

UC Berkeley

UC Berkeley Electronic Theses and Dissertations

Title

Theoretical Investigation of Binary Eutectic Alloy Nanoscale Phase Diagrams

Permalink

<https://escholarship.org/uc/item/05x231mf>

Author

Boswell-Koller, Cosima Nausikaa

Publication Date

2012

Peer reviewed|Thesis/dissertation

**Theoretical Investigation of Binary Eutectic Alloy Nanoscale Phase
Diagrams**

by

Cosima Nausikaa Boswell-Koller

A dissertation submitted in partial satisfaction
of the requirements for the degree of

Doctor of Philosophy

in

Engineering - Materials Science and Engineering

in the

GRADUATE DIVISION

of the

UNIVERSITY OF CALIFORNIA, BERKELEY

Committee in charge:

Professor Daryl C. Chrzan, Chair

Professor Eugene E. Haller

Professor Ali Javey

Spring 2012

Theoretical Investigation of Binary Eutectic Alloy Nanoscale Phase Diagrams

Copyright © 2012

by

Cosima Nausikaa Boswell-Koller

Abstract

Theoretical Investigation of Binary Eutectic Alloy Nanoscale Phase Diagrams

by

Cosima Nausikaa Boswell-Koller

Doctor of Philosophy in Engineering - Materials Science and Engineering

University of California, Berkeley

Professor Daryl C. Chrzan, Chair

Recently, embedded binary eutectic alloy nanostructures (BEANs) have drawn some attention. A previously calculated equilibrium structure map predicts four possible nanocrystal alloy morphologies: phase-separated, bi-lobe, core-shell and inverse core-shell governed by two dimensionless interface energy parameters. The shape of the bilobe nanoparticles is obtained by finding the surface area of all interfaces that minimizes the overall energy, while also maintaining mechanical equilibrium at the triple point.

Two representative alloy systems displaying eutectic phase diagrams and negligible solid solubility were chosen: SnGe and AuGe. SnGe samples were prepared by sequential implantation of Ge and Sn into SiO₂. AuGe samples were prepared by implanting Ge within Au-doped silica films. Transmission electron microscopy images revealed bi-lobe nanocrystals in both samples. Therefore, the interface energies in both systems must be such that the dimensionless parameters lie in the region of bi-lobe stability.

Careful analysis of the bi-lobe structure leads to the determination of two dimensionless length scales, which describe the bi-lobe independent of the size of the nanoparticle. These two parameters, η_1 and η_2 can be used to calculate contours of equal η_1 and η_2 over the entire range of bi-lobe stability. Experimental measurement and comparison to predicted structures leads to determination of acting dimensionless interface energies. Experimentally available wetting data is then used to calculate the remaining interface energies in the system. $\gamma_{Ge(s)/SiO_2}$ was found to be between $0.82-0.99 \frac{J}{m^2}$. $\gamma_{Ge_{0.22}Sn_{0.78}(l)/SiO_2}$ and $\gamma_{Au_{0.53}Ge_{0.47}(l)/SiO_2}$ are determined to be 1.20 and $0.94 \frac{J}{m^2}$, respectively.

To investigate the possibility of size effects at the nanoscale, size dependent phase diagrams for the AuGe and SnGe system are determined. This is done by the theoretical approach first outlined by Weissmueller *et al.*, which takes into account the energy contribution of the various morphologies listed above. Results from this calculation are compared to those using the tangent line construction approach. The composi-

tion dependent surface energies of binary alloy liquids required in this calculation are determined using Butler's equation.

I dedicate this dissertation to my terrific family. First and foremost, I must thank my husband, Jürgen, for his never-ending moral support, always standing by me through thick and thin, and for always having kind and encouraging words for me. Also, my parents, Astrid and Frank, for their support throughout my academic and personal endeavors.

Contents

Contents	ii
List of Figures	iv
List of Tables	x
Acknowledgements	xi
1 Introduction	1
2 Analysis of the Bilobe Nanostructure	4
3 Application of Bilobe Analysis to Two Experimental Systems	15
3.1 SnGe	15
3.2 AuGe	21
4 Application of Butler's Equation to SnGe and AuGe Systems	28
5 Nanoscale Phase Diagrams	39
5.1 Free energy curve of a Solid-Solid particle	49
5.2 Free energy curve of a Liquid particle	54
5.3 Free energy curve of a Particle consisting of Ge-solid and AuGe-Liquid	54
5.4 Free energy curve of a Particle consisting of Au-solid and AuGe-Liquid	61
5.5 Nanoscale Phase Diagram of Free-standing AuGe particles	65
5.6 Nanoscale Phase Diagram of Free-standing SnGe particles	71
5.7 Nanoscale Phase Diagram of AuGe particle embedded in SiO ₂	72
5.8 Discussion	78

6 Conclusions	82
Bibliography	84

List of Figures

1.1	Schematic of the most important features of an equilibrium bulk phase diagram. The system consists of two elements A and B	2
2.1	Equilibrium structure map for a binary alloy nanoparticle consisting of volume fraction of β -phase equal to 0.70. The regions of stability consist of phase-separated, two distinct core-shell structures, and the bilobe nanoparticle region.	5
2.2	A bilobe nanocrystal showing the triple point and relevant parameters used to describe the conditions of mechanical equilibrium.	6
2.3	3-dimensional rendering of a bilobe nanocrystal of parameters $\{f_\beta, \gamma_1, \gamma_2\} = \{0.5, 1.5, 2.0\}$	7
2.4	Cross-sectional view of the bi-lobe nanocrystal presented in Figure 2.3 with parameters $\{f_\beta, \gamma_1, \gamma_2\} = \{0.5, 1.5, 2.0\}$ is shown. Here, the important geometrical features, d_{MIN} , d_{MAJ} and d_{INT} are depicted. . .	9
2.5	Considering a binary alloy particle of equal volume fractions of α and β -phases, a contour plot of $\eta_1 = d_{MIN}/d_{MAJ}$ is calculated and graphically presented. As the $\{\gamma_1, \gamma_2\}$ doublet increases, the particles become increasingly spherical. As expected for $f_\beta = 0.5$, the contours are symmetric about the line $\gamma_1 = \gamma_2$	10
2.6	The contour plot of $\eta_2 = d_{INT}/d_{MAJ}$ is shown for a binary alloy particle of equal volume fractions of α and β -phases. η_2 is a measure of the internalization of the β -phase. Again, the contours are symmetric about the line $\gamma_1 = \gamma_2$	11
2.7	Overlaid contour plots of η_1 (shaded contours) and η_2 (dashed lines) are shown. The red star represents the example discussed in the text.	13
3.1	Representative TEM image of SnGe bilobe nanocrystals used in determination of interface energy from the characterized bilobe geometry.	16

3.2	A bilobe nanocrystal is shown with one lobe (radius R) centered at $\{x, y, z\} = \{0, 0, 0\}$ and a second lobe centered at $\{x, y, z\} = \{x_c, 0, 0\}$. To investigate the range of possible η_1 -values, a rotation about the y -axis is considered. As the bilobe undergoes rotation by θ -degrees, the projection of the center of the second bilobe onto the x -axis becomes $x_c \cdot \cos(\theta)$	17
3.3	η_1 can take on a spread of possible values depending on the degree of rotation, θ . However, the maximum value must be equal to 1, while the minimum value represents an advantageously oriented bilobe.	18
3.4	Contour plot corresponding to a volume fraction of $f_\beta = 0.28$. The contours $\eta_1^{SnGe} = 0.88$ and $\eta_2^{SnGe} = 0.67$ are highlighted. The intersection of the two contours lies at $\gamma_1 = 2.31$ and $\gamma_2 = 2.43$	19
3.5	The equilibrium bulk phase diagram of the SnGe system is presented. Contours represent the volume fraction of the liquid phase in the system.	20
3.6	γ_{Ge^{sol}/SiO_2} and $\gamma_{Sn_xGe_{1-x}^{liq}/SiO_2}$ calculated as a function of temperature. γ_{Ge^{sol}/SiO_2} is represented by the black line, while $\gamma_{Sn_xGe_{1-x}^{liq}/SiO_2}$ is shown in blue.	22
3.7	A representative TEM image of AuGe nanoparticles is shown. Clearly, the bilobe structure has formed.	23
3.8	Contour plot corresponding to a volume fraction of $f_\beta = 0.28$. The contours $\eta_1^{SnGe} = 0.94$ and $\eta_2^{SnGe} = 0.71$ are highlighted. The intersection of the two contours indicates acting values of $\gamma_1 = 2.31$ and $\gamma_2 = 2.43$	23
3.9	γ_{Ge^{sol}/SiO_2} plotted as a function of temperature. The black line represents the results calculated from the SnGe system, while the gray line is calculated from the AuGe system.	24
3.10	Contour plot for the SnGe system at $T = 600$ °C for which f_β is predicted to be equal to 0.31.	26
3.11	Contour plot for the AuGe system at $T = 600$ °C for which f_β is predicted to be equal to 0.33.	27
4.1	The excess free energy of mixing of a AuGe (blue) and SnGe (red) alloy at $T = 1500K$ is shown. The solid lines are calculated according to the Redlich-Kister expansion using published interaction parameters for each system. The dashed lines (the blue line is not visible under the red dashed line) assume no excess energy of mixing, i.e. the interaction parameters in the Redlich-Kister expansion are identically set equal to 0.	32

4.2	The partial molar Gibbs free energies of components A and B in the bulk are plotted as a function of x_{Ge}^B . Blue represents the AuGe-system, while red represents the SnGe-system. $\overline{G}_A^{Ex,b}(T, x_B^b)$ is plotted as a thick, solid line and $\overline{G}_B^{Ex,b}(T, x_B^b)$ is plotted as a dashed line.	33
4.3	The concentration of Ge in the surface of a liquid alloy is calculated as a function of Ge concentration in the bulk liquid. As before, blue represents the AuGe system and red represents the SnGe system.	35
4.4	The composition dependent surface tensions of the $Au_{1-x}Ge_x$ and $Sn_{1-x}Ge_x$ liquids are plotted in blue and red, respectively. The black dotted line represents the concentration weight average of the liquid elements at $T = 1500$. In both systems, a deviation from the concentration weighted average is predicted.	36
4.5	The composition dependent surface tensions of $Sn_{1-x}Ge_x$ liquids are calculated at various temperatures: $T = 573, 773, 973, 1173, 1373,$ and $1573K$	37
4.6	The composition dependent surface tensions of the $Au_{1-x}Ge_x$ liquids are plotted at $T = 973, 1173, 1373, 1573, 1773,$ and $1973K$	38
5.1	Schematic representation of the temperature dependent total Gibbs' free energy of a solid and a liquid system, shown in blue and red, respectively. The temperature at which the energy of the phases is equal represents the bulk melting point of the system.	40
5.2	The temperature dependent total free energy per volume of particle of a representative solid and a liquid particle is shown in blue and red, respectively. The addition of the surface term shifts the free energy upward for both the liquid and the solid phase. Generally, however, the shift of the solid phase is more pronounced, thus decreasing the melting temperature.	42
5.3	The free energy of a particle as it undergoes melting. As the volume fraction of the liquid within the particle is increased, the energy of the particle undergoes a maximum value, that can be seen as a kinetic barrier for melting. This leads to the possibility of superheating and supercooling in nanoparticles due to the addition of the surface/interface energy terms.	43

5.4	Gibbs' free energy of two solid phases, A (blue) and B (red), and a homogeneous liquid phase (purple) at three temperatures are considered. In macroscopic alloys, the tangent rule construction (black, dashed line) is used to determine the compositions that lead to the solidus and liquidus lines of phase diagrams. In the left most panel, an alloy composed of two solid phases, A and B , minimizes the overall energy of the system. Above the eutectic temperature, a solid A -liquid AB structure minimizes the energy. Above the liquidus temperature for the composition under consideration, the homogeneous liquid phase is stable.	45
5.5	A nanoscale system composed of the same phases as in Figure 5.4 is depicted. Unlike before, surface effects must be considered. This leads to a shift in the overall free energies of all phases (recall surface energies are positive). Additionally, the tangent rule construction may no longer be applied and the free energy curve must be calculated exactly. This leads to a positive deviation from the tangent rule construction. . . .	47
5.6	Volume fraction of Ge-solid in a solid-solid particle is calculated as a function of Ge content. AuGe (blue) shows a positive deviation from linearity due to the larger molar volume of Ge-solid over Au-solid. The opposite is true for the SnGe-system shown in red.	51
5.7	The four possible binary alloy nanoparticle morphologies are calculated as a function of Ge-concentration (which in turn can be used to calculate the volume fraction Ge-solid). At a temperature of $300K$ the surface and interface energies of Au- and Ge-solid phases predict $\{\gamma_1, \gamma_2\} = \{0.699231, 0.320272\}$. This indicates that the bilobe geometry is stable, which is verified as the magenta line representing the energy of the bilobe structure minimizes the surface contribution to the free energy for all compositions. The blue line representing the phase separated morphology is very close to the bilobe prediction and thus not visible.	52
5.8	The surface contribution to the free energy of the bilobe structure as seen in Figure5.7 is plotted separately. The expected positive curvature is seen. Therefore, the tangent rule construction is not applicable in this type of nanoscale system.	53
5.9	The free energy curve of a AuGe-liquid alloy is calculated as a function of composition. The black dotted line represents the volumetric contribution. The thick, blue line represents the total energy of the liquid alloy after the surface contribution has been taken into account. This leads to an increase in the overall free energy when normalized by the total surface area.	55

5.10	Volume fraction of Ge-solid in a particle consisting of Ge-solid and a AuGe-liquid of composition $x_L = 40$ at. % Ge as a function of alloy composition, x_{Ge}	56
5.11	The four possible binary alloy nanoparticle morphologies are calculated as a function of Ge-concentration at a temperature of $1300K$ and $x_L = 0.40$. The contribution of the surfaces/interfaces to the total energy is minimized by the bilobe geometry.	58
5.12	$G^{Au(sol)Ge(sol)}(x_{Ge})$ (blue), $G^L(T, x_{Ge})$ (red) and $G^{Ge(sol)L}(T, x_{Ge}, x_L)$ (purple) are calculated for a particle of size $r = 25 \times 10^{-9}m$. Liquids of composition $x_L = 0.01, 0.05, 0.10, 0.15, 0.20, 0.25, 0.30, 0.35, 0.40, 0.45, 0.51, 0.55, 0.60, 0.65, 0.70, 0.75, 0.80, 0.85, 0.90, 0.95, 0.99$ are considered for $G^{Ge(sol)L}(T, x_{Ge}, x_L)$	59
5.13	$G^{Au(sol)Ge(sol)}(x_{Ge})$ (blue), $G^L(T, x_{Ge})$ (red) and $G^{Ge(sol)L}(T, x_{Ge}, x_L)$ (purple) are calculated for a particle of size $r = 5 \times 10^{-9}m$. Liquids of composition $x_L = 0.01, 0.05, 0.10, 0.15, 0.20, 0.25, 0.30, 0.35, 0.40, 0.45, 0.51, 0.55, 0.60, 0.65, 0.70, 0.75, 0.80, 0.85, 0.90, 0.95, 0.99$ are considered for $G^{Ge(sol)L}(T, x_{Ge}, x_L)$	60
5.14	Magnified view of Figure 5.13. Clearly, the solid-liquid phase minimizes the overall energy at compositions above ≈ 0.35 , while at larger particle size the solid-solid phase is stable.	62
5.15	Volume fraction of $Au_{0.6}Ge_{0.4}$ -liquid in a particle consisting of Au-solid and a AuGe-liquid of composition $x_L = 0.4$ at. % Ge as a function of alloy composition, x_{Ge}	63
5.16	The four possible binary alloy nanoparticle morphologies are calculated as a function of Ge-concentration at a temperature of $1300K$ and $x_L = 0.40$. The Au(sol)-core/AuGe(liq)-shell structure minimizes the contribution of the surfaces/interfaces to the total energy. At these temperatures and compositions, the bilobe structure cannot be realized.	64
5.17	$G^{Au(sol)Ge(sol)}(x_{Ge})$ (blue), $G^L(T, x_{Ge})$ (red), $G^{Ge(sol)L}(T, x_{Ge}, x_L)$ and $G^{Au(sol)L}(T, x_{Ge}, x_L)$ (both shown in purple) are calculated for a particle of size $r = 5 \times 10^{-9}m$ as a function of alloy composition, x_{Ge}	66
5.18	$G^{Au(sol)Ge(sol)}(x_{Ge})$ (blue), $G^L(T, x_{Ge})$ (red), $G^{Ge(sol)L}(T, x_{Ge}, x_L)$ and $G^{Au(sol)L}(T, x_{Ge}, x_L)$ (both shown in purple) are calculated for a particle of size $r = 5 \times 10^{-9}m$ as a function of alloy composition, x_{Ge} . $\sigma^{Au(sol)L} = \sigma^{Ge(sol)L} + 2$	67
5.19	Theoretical phase diagrams of particles of sizes $r = 25 \times 10^{-9}, 10 \times 10^{-9}$ and 5×10^{-9} m are shown in the top, center and bottom plots, respectively. These phase diagrams are calculated using the theoretical approach outlined by Weissmueller <i>et al.</i> (68; 8; 69)	68

5.20	The size dependent phase diagrams of the AuGe system are calculated. Three particle sizes are considered: $r = 25 \times 10^{-9}$, 10×10^{-9} and 5×10^{-9} m, which are shown in the top, center and bottom panels, respectively. The left column considers assumed values of $\sigma^{Au(sol)L} = \sigma^{Ge(sol)L} + 0.054$, while the right column considers $\sigma^{Au(sol)L} = \sigma^{Ge(sol)L} + 2$. The black, dotted and black, solid lines represent the “bulk” and “standard nanoscale” phase diagrams, respectively. Phases under consideration are: Au-solid/Ge-solid (dark blue), homogenous liquid (red), Au-solid/liquid (light blue) and Ge-solid/liquid (yellow).	69
5.21	Three SnGe particle sizes are considered, $r = 25 \times 10^{-9}$, 10×10^{-9} and 5×10^{-9} m, and the size dependent phase diagrams are calculated. Resulting phase diagrams are shown in the top, center and bottom panels, respectively. The black, dotted lines represent the “bulk” phase diagram, while the black, solid lines represent the size dependent “standard nanoscale” phase diagrams. The dark blue, red and yellow regions represent the Sn-solid/Ge-solid phase, homogenous liquid, and Ge-solid/liquid phases, respectively.	73
5.22	The composition dependent interface energies of $Au_{1-x}Ge_x$ -liquids are calculated as a function of Ge concentration for various temperatures using Butler’s equation.	75
5.23	A AuGe particle of size $r = 5 \times 10^{-9}$ m is considered to be embedded in a SiO_2 matrix and the size dependent phase diagram is considered. The blue region represents the solid-solid phase, while red represents the homogeneous liquid phase. Light blue and yellow represent the Au-solid/liquid and Ge-solid/liquid phases, respectively. The dotted line represents the “bulk” phase diagram as a point of comparison. . .	76
5.24	γ_{Ge^{sol}/SiO_2} is plotted as a function of temperature after taking into account the possibility of size effects in the AuGe system. The black line represents the results calculated from the SnGe system, while the gray line is calculated from the AuGe system at $r = 5 \times 10^{-9}$ m. . . .	77
5.25	In the two-phase regions of the phase diagram, the composition of the respective liquid phases is plotted. The legend shows that liquids composed of 0 at. % Ge is represented by blue, while a liquid of 100 at. % Ge is represented by red.	79
5.26	The Ge(sol)/AuGe(liq) region of the phase diagram is considered. Here, we determine which morphology is the structure that minimizes the total free energy of the particle. Blue and yellow represent the AuGe(liq)-core/Ge(sol)-shell and Ge(sol)-core/AuGe(liq)-shell structures, respectively. Red represents the bilobe structure. There is no region which is stabilized by the phase separated morphology.	80

List of Tables

2.1	Excerpt of a Data Set: $\{\eta_1, \eta_2\}$ -Values for $f_\beta = 0.5$	14
4.1	σ , Surface Tension (J/m^2) of Elemental Liquid	30
4.2	Molar Volume (m^3/mol) of Elemental Liquid	31
4.3	$\{L_1, L_2, L_3, L_4\}$, Interaction Parameters	31
5.1	$\Delta G(\text{solid} \rightarrow \text{liquid})$ (J/m^3)	81

Acknowledgements

The graduate school experience and writing of this dissertation represent the biggest challenges I have yet had to overcome. While my name appears as author, this dissertation truly represents a group of people, who have supported, encouraged and guided me through this experience. The list is long, but I am truly grateful to each and every one of you.

Professor Daryl C. Chrzan who graciously offered me a position in his research group. I thank you for your support, understanding and kind words of encouragement on my academic path and for providing me with an excellent atmosphere for doing research. Not everyone finds an advisor so committed to his students that he would spend personal fishing time with them.

I would like to thank all those who attended the Wednesday morning “Nanomeeting”. Thank you for the stimulating discussions and priceless input in my work. Professor Eugene Haller and Dr. Joel Ager, III deserve a special thanks for providing us with invaluable experience and expertise and always challenging us to think outside the box and push our research to the next level. Also, I could not have completed this research without my experimental counterparts, former students, Dr. Julian Guzman and Dr. Swanee Shin, who tirelessly prepared samples and spent countless hours with me at the microscope. Dr. Chun-Wei Yuan, my predecessor, must be thanked for laying the foundation for this research. My lab mate and friend Matt Sherburne, who was there to calm me down when my level of frustration was high. Karen Bustillo, James Mastandrea, and Carolyn Sawyer for the many insightful discussions and interesting ideas. Finally, a thank you to my lab mates for their input during research presentations. It was truly a pleasure to have worked with all of you.

I would have never reached Berkeley had it not been for my time at the University of Florida. The Materials Science and Engineering department and its’ faculty and staff will always hold a special place in my heart. Thank you to Dr. Susan Sinnott, who provided me with my first research experience. It was she, and the members of her group, especially Dr. Jennifer Wohlwend, who guided me to the world of computation and theory. Also, Dr. Gerald Bourne for writing countless recommendations, and encouraging my academic endeavors.

Special thanks also to Dr. Aurelia Herrmann who became my mentor through the “Deutscher Akademischer Austausch Dienst Research Internships for Scientists and Engineers”. My time spent at the Max-Planck Institut was inspiring and truly fueled my desire to attend graduate school.

While the writing of this dissertation represents the culmination of my graduate research, it also marks the end to a significant chapter in my life. I was truly fortunate to have had such a wonderful set of classmates, who all made this experience unforgettable. When I felt overwhelmed and close to the end, their encouraging words and fun events kept me going. Especially Alyssa Maich, whom I am lucky to call a friend, was there for me always and cheered me up when I was feeling down.

My entire extended family, especially my grandparents, my friends from all walks of life, my South African host family, and my in-laws must be thanked for having such confidence in me. You have always pushed me to do my very best and without this motivation I could accomplish nothing.

I would like to offer my sincerest and heartfelt thanks to my parents, Frank and Astrid Boswell, and brother, Saska. You have been there for me always, supporting my crazy ideas and goals. Without you this would not have been possible.

Finally, to my husband, Dr. Jürgen Koller. Words cannot express my appreciation to you. You are my rock and without you, I would not be here today. Thank you for your never-ending love, support, encouragement, and patience. Ich liebe Dich!

Curriculum Vitæ

Cosima Nausikaa Boswell-Koller

Education

2005	Santa Fe Community College A.A., Pre-Engineering
2008	University of Florida B.S., Materials Science and Engineering
2011	University of California, Berkeley M.S., Materials Science and Engineering
2012	University of California, Berkeley Ph.D., Materials Science and Engineering

Personal

Born	November 10, 1983, Ozark, AL
------	------------------------------

Chapter 1

Introduction

In Materials Science and Engineering and many other related sciences, phase diagrams have been used for decades as a convenient tool to determine the temperature dependent equilibrium compositions of metal alloys.⁽²²⁾ Besides extracting simple information such as melting temperatures or eutectic points (see Figure 1.1), the fractional amount of any given phase within a sample can be easily predicted using the well-known Lever Rule, and the predictions can be used to analyze experimental data and aid in the design of material processing routes.⁽⁵⁾ Many of these diagrams have been established using calculations in conjunction with measurements involving bulk materials.

While the information obtainable from these diagrams is certainly valid at the macro-scale, the advent of nano-technology is increasingly challenging the usability of these data for modern science. It is commonly accepted that as the size of a system decreases, the surface properties of the system become increasingly important. This importance is especially evident in the size-dependent melting of nanocrystals, a concept theoretically investigated by Pawlow as early as 1909.⁽⁴⁹⁾ More recently Buffat and Borel investigated the melting of Au nanocrystals.⁽⁷⁾ Results from their investigations show that as the size of the Au nanocrystals is decreased the melting temperature significantly decreases as well. Astonishingly, Au nanocrystals with a radius of 12 Å exhibited a melting point of 27 °C, while the bulk melting point of Au is 1063 °C. These data indicate that the equilibrium phase of some Au nanocrystals is liquid at room temperature, a concept that is hard to grasp when considering the physical properties of most bulk metals. Similarly, Sn particles of approximately 50 Å radius exhibit a melting point of 153 °C (bulk melting point of 227 °C), with other common metals such as Bi, Ag and Pb and semiconductors (CdS) following similar trends.^(46; 30; 10; 51; 23) In general, the melting point suppression in nanocrystals is inversely proportional to the radius.

These findings may be explained by studying the surface energies of the involved

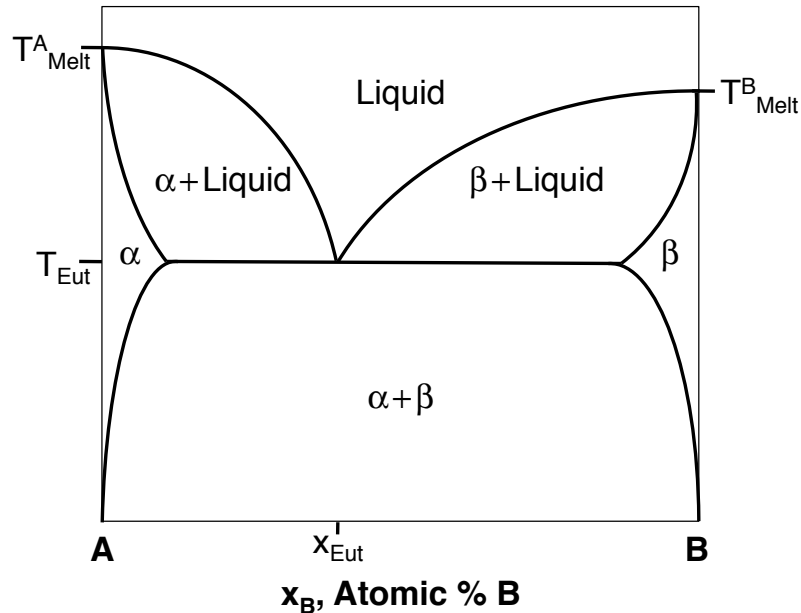


Figure 1.1. Schematic of the most important features of an equilibrium bulk phase diagram. The system consists of two elements A and B

materials and their influences on the minimization of free energy. While such surface effects are negligible at the macro-scale, they become increasingly important on the nanoscale where a substantial surface energy contribution (due to the high surface/volume ratio) represents a significant portion of the total energy. Following similar arguments, nanocrystals of metals embedded in a matrix material (such as SiO_2) behave differently compared to their free-standing counterparts. For example, embedded Ge nanocrystals (2.5 nm radius) behave differently from their free-standing analogues.⁽⁷⁰⁾ Both superheating and supercooling of such particles can be observed with the hysteresis loop centered approximately at the bulk melting point of 938 °C (hysteresis loop of 470 °C). Melting of the Ge nanocrystals starts at 1077 °C and ends at 1177 °C, indicative of superheating of more than 220 °C. The corresponding re-solidification of the nanocrystals initiates at 707 °C, is terminated at 607 °C, and thus exhibits supercooling of up to 330 °C.

Considering the substantial effects of particle size on the physical properties of a pure material, it is not terribly surprising that binary systems exhibit similar distortions from bulk-phase behavior that may even be more complicated compared to those of pure metals. Although nano-sized materials introduce complications that can be quite challenging to model, they also promote unrivaled opportunities for scientists to stabilize materials of previously unknown compositions and geometries. Possible geometries of binary nanocrystals have been calculated by Yuan et al. leading to an equilibrium structure map as a function of dimensionless interface energy ratios.⁽⁷²⁾ Recent studies have shown that systems involving SnGe and AuGe embedded in SiO_2

display a bilobe geometry.(60; 24) These findings indicate that the relevant interface energies acting in these systems are located in the bilobe stability region of the equilibrium structure map. However, the question arises if additional information can be determined from the equilibrium geometry. If the bilobe stability region is examined closely, it becomes evident that the equilibrium morphology changes with changing dimensionless interface energies.

In Chapter 2, two dimensionless aspect ratios will be established using the bilobe geometry. These aspect ratios can be experimentally measured using transmission electron microscopy (TEM) images of binary systems displaying a bilobe geometry. Once the aspect ratios are measured they can be compared to theoretically determined aspect ratios and the dimensionless interface energies can be established. In Chapter 3, recent studies involving SnGe and AuGe systems will be used to further elaborate on the previously introduced concepts, and will simultaneously provide the basis for theoretical approaches to explain physical phenomena. The stable geometries of Germanium-Tin (SnGe) and Gold-Germanium (AuGe) are predicted as a function of temperature (T) and composition. Butler's equation is discussed and used to calculate the surface and interface energies of the AuGe and SnGe systems in Chapter 4. Finally, in Chapter 5 the nanoscale phase diagrams of the SnGe and AuGe systems are calculated.

Chapter 2

Analysis of the Bilobe

Nanostructure

Generally, an embedded binary alloy nanocrystal system is characterized by three distinct phases, α , β and *matrix*, where the *matrix* phase can either be a solid matrix such as SiO_2 or the vapor phase. The α and β phases can be elemental solids/liquids, liquid/solid alloys or phases differing in crystal structure. The systems investigated herein always contain three acting surface/interface energies: $\gamma_{\alpha/M}$, $\gamma_{\beta/M}$ and $\gamma_{\alpha/\beta}$. As demonstrated previously by Yuan et al. who defined two dimensionless interface energies $\gamma_1 = \gamma_{\alpha/M}/\gamma_{\alpha/\beta}$ and $\gamma_2 = \gamma_{\beta/M}/\gamma_{\alpha/\beta}$.(72) From these values, γ_1 and γ_2 may be used to calculate the optimum structure, thus effectively minimizing the overall energy of the system. Possible geometries include two distinct core-shell structures, phase-separated and the lobe-lobe (bilobe) morphology, which may be used to calculate an equilibrium structure map.

An example of such an equilibrium structure map is shown in Figure 2.1 for a binary alloy consisting of 30 volume % of the α -phase and 70 volume % of the β -phase. This map is calculated using the procedure described by Yuan et al.(72) Systems with interface energies that lead to doublets, $\{\gamma_1, \gamma_2\}$, in the region defined by

$$\gamma_2 \geq -\gamma_1 + 1 \quad (2.1)$$

$$\gamma_2 \leq \gamma_1 + 1 \quad (2.2)$$

$$\gamma_2 \geq \gamma_1 - 1 \quad (2.3)$$

are predicted to result in bi-lobe structures. While these calculations may predict the overall stable structure of a given binary system, the exact equilibrium shapes of the bilobes also depend on one other parameter: the volume fraction of the β -phase.(72) The region of bilobe stability will be the focus of the following paragraphs.

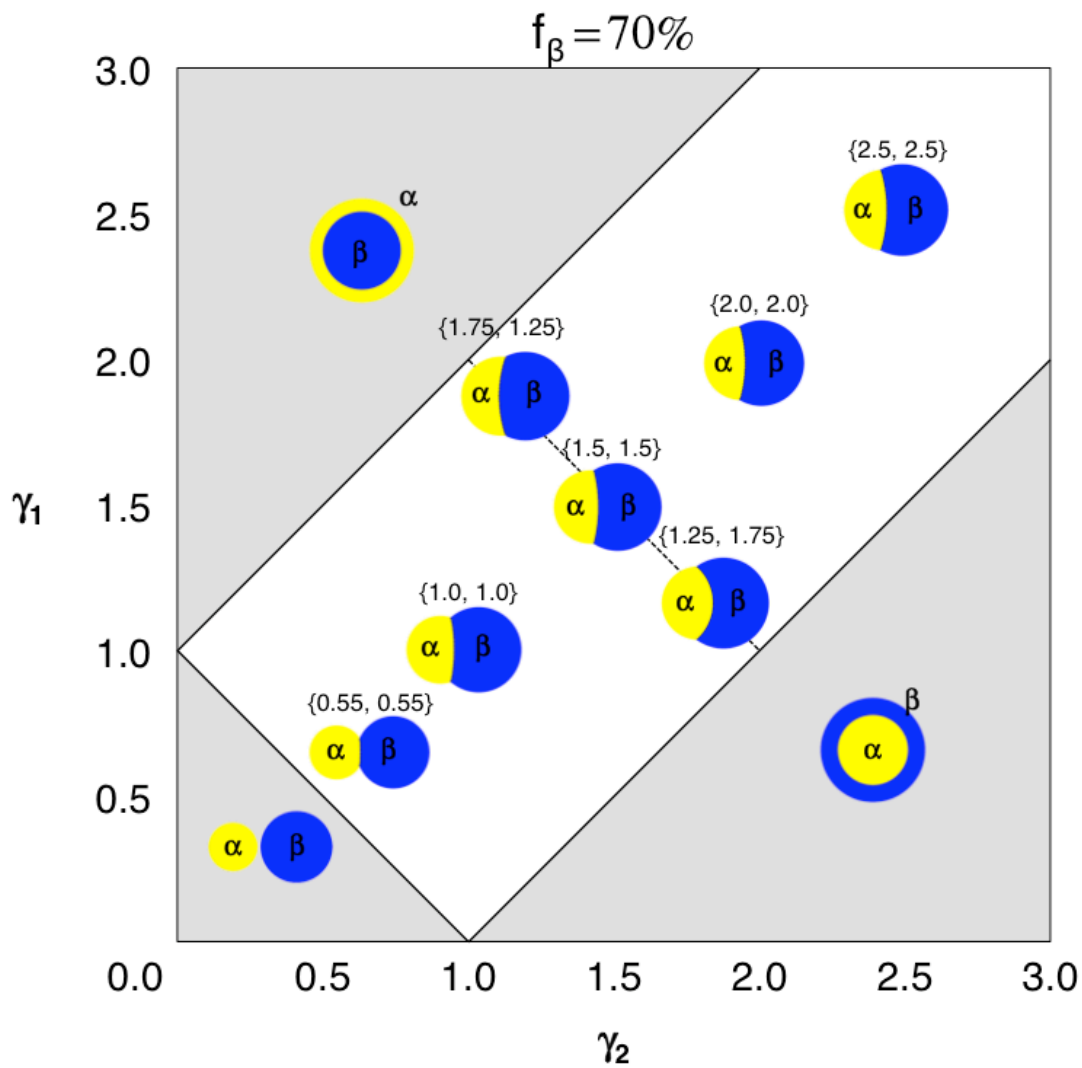


Figure 2.1. Equilibrium structure map for a binary alloy nanoparticle consisting of volume fraction of β -phase equal to 0.70. The regions of stability consist of phase-separated, two distinct core-shell structures, and the bilobe nanoparticle region.

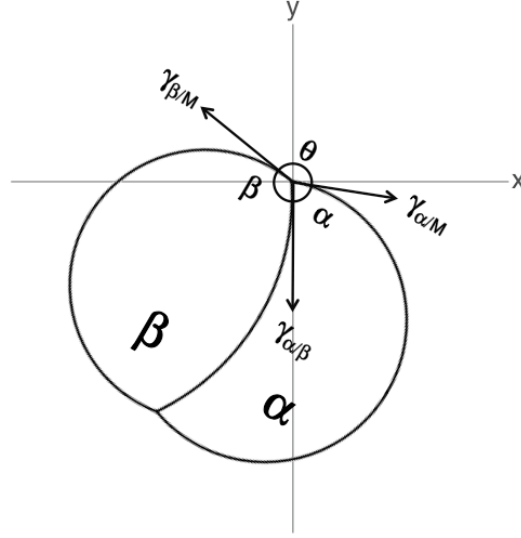


Figure 2.2. A bilobe nanocrystal showing the triple point and relevant parameters used to describe the conditions of mechanical equilibrium.

To calculate the equilibrium bilobe structure, one must first satisfy the conditions of mechanical equilibrium. A schematic of a bilobe nanocrystal is shown in Figure 2.2. The arrows represent the acting interface energies between the individual phases: $\gamma_{\alpha/M}$, $\gamma_{\beta/M}$ and $\gamma_{\alpha/\beta}$. Also shown are the three angles between the phases: α , β and θ . The equations of mechanical equilibrium then become:

$$\gamma_{\beta/M} \cdot \sin(\beta - \pi/2) = \gamma_{\alpha/M} \cdot \sin(\pi/2 - \alpha) + \gamma_{\alpha/\beta} \quad (2.4)$$

$$\gamma_{\beta/M} \cdot \cos(\beta - \pi/2) = \gamma_{\alpha/M} \cdot \cos(\pi/2 - \alpha) \quad (2.5)$$

$$\alpha + \beta + \theta = 2\pi \quad (2.6)$$

A dimensionless analysis can be obtained by dividing the equations through by $\gamma_{\alpha/\beta}$:

$$\gamma_2 \cdot \sin(\beta - \pi/2) = \gamma_1 \cdot \sin(\pi/2 - \alpha) + 1 \quad (2.7)$$

$$\gamma_2 \cdot \cos(\beta - \pi/2) = \gamma_1 \cdot \cos(\pi/2 - \alpha) \quad (2.8)$$

Equations 2.7 and 2.8 can be solved for the two unknown values, α and β , for any set of $\{\gamma_1, \gamma_2\}$. Then, θ will also be known. From this, the three spherical caps, of which the bilobes are composed, can be constructed. Within the bilobe region, the bilobe structure is the morphology, which minimizes the overall surface energy of the nanoparticles.

Initially, the case of equal volume fraction of α and β phase will be examined. Forthwith, the volume fraction of β -phase will be denoted f_β . In Figure 2.3, a 3-dimensional rendering of the exterior of the equilibrium bilobe structure of a nanocrystal with parameters $\{f_\beta, \gamma_1, \gamma_2\} = \{0.5, 1.5, 2.0\}$ is shown. Here, the α and β -phases

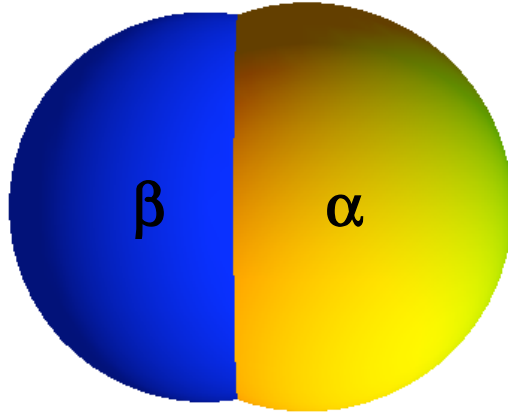


Figure 2.3. 3-dimensional rendering of a bilobe nanocrystal of parameters $\{f_\beta, \gamma_1, \gamma_2\} = \{0.5, 1.5, 2.0\}$.

are represented in yellow and blue, respectively. It should be noted that the bilobe depicted in this figure is composed of equal volume fractions of α and β -phase. However, if this was not known *a priori*, one may assume that the internal interface is flat and that there is a larger volume fraction of α -phase within the particle.

While a flat internal interface is possible, it is not necessarily the shape which minimizes the overall energy of the system. As shown in Figures 2.1 and 2.2, the internal interface often displays a curvature. Figure 2.4 shows the cross-sectional view of the nanocrystal represented in Figure 2.3. It becomes evident through this graphical approach that the internal interface, which is generally not visible through standard microscopy experiments, is curved. Unfortunately, the direction and magnitude of this curvature is difficult to determine experimentally. Using only the above described procedure, no further information can be obtained from an experimentally observed bilobe structure, only that the interface energies must be such that the equilibrium structure is a bilobe nanoparticle.

Experiments do, however, offer the possibility of measuring various length scales, that characterize bilobes of differing dimensionless interface energies. In Figure 2.4, three lengths are defined: d_{MAJ} , d_{MIN} and d_{INT} . d_{MAJ} , or the major axis, is the distance from the edge of the α -phase to the edge of the β -phase. To define the minor axis, d_{MIN} , one chooses the larger lobe and measures the size as shown in Figure 2.4 (in this figure, the larger lobe is the α lobe; however, this is not always the case). Finally, the distance from the β -edge to the intersection of the α and β lobes will define d_{INT} . While Figure 2.4 shows a perfectly oriented bilobe structure, these three lengths can be determined for rotated bilobes as well. The effect of bilobe orientation will be discussed in detail in the following chapter. Thus, these three lengths can be measured from microscopy images (see below).

Using these lengths, two aspect ratios, $\eta_1 = d_{MIN}/d_{MAJ}$ and $\eta_2 = d_{INT}/d_{MAJ}$, can be defined. η_1 can be described as a measure of the sphericity of the nanocrystals.

As η_1 approaches 1, the nanocrystal becomes increasingly spherical. This is the case in both the α -core/ β -shell and β -core/ α -shell structures. In the region of phase separated particles, η_1 can be calculated using the procedure outlined in the following paragraph.

In the phase separated region, the volume fraction f_β is calculated as follows:

$$f_\beta = \frac{\frac{4}{3}\pi r_\beta^3}{\frac{4}{3}\pi r_\alpha^3 + \frac{4}{3}\pi r_\beta^3} = \frac{r_\beta^3}{r_\alpha^3 + r_\beta^3}, \quad (2.9)$$

where r_α and r_β are the radii of the α and β particles, respectively. Rearranging, r_α is calculated with

$$r_\alpha = r_\beta \left(\frac{1 - f_\beta}{f_\beta} \right)^{1/3} \quad (2.10)$$

and η_1 becomes

$$\eta_1 = \frac{2 \cdot \text{Max}[r_\alpha, r_\beta]}{2 \cdot r_\alpha + 2 \cdot r_\beta} = \frac{\text{Max}[r_\alpha, r_\beta]}{r_\alpha + r_\beta}, \quad (2.11)$$

where Max represents the maximum absolute value. This can be simplified to

$$\eta_1 = \frac{r_\beta \left(\frac{1-f_\beta}{f_\beta} \right)^{1/3}}{r_\beta \left(\frac{1-f_\beta}{f_\beta} \right)^{1/3} + r_\beta} = \frac{\left(\frac{1-f_\beta}{f_\beta} \right)^{1/3}}{\left(\frac{1-f_\beta}{f_\beta} \right)^{1/3} + 1} \quad (2.12)$$

$$\eta_1 = \frac{r_\beta}{r_\beta \left(\frac{1-f_\beta}{f_\beta} \right)^{1/3} + r_\beta} = \frac{1}{\left(\frac{1-f_\beta}{f_\beta} \right)^{1/3} + 1}, \quad (2.13)$$

where the first equation represent η_1 for a bilobe with a larger α -lobe and the second one represents a bilobe with larger β -lobe. The value of η_1 in the phase-separated region also represents the minimum value that η_1 can take on, as in the bilobe region d_{MAJ} must decrease and therefore increase η_1 . For the case of $f_\beta = 0.5$, the minimum value of η_1 is determined to be 0.5.

In contrast, η_2 is a measure of the internalization of the β -phase by the α -phase. As η_2 approaches 1, the β -phase is barely visible and the bilobe nanocrystal approaches an β -core/ α -shell structure. Consequently, as η_2 approaches 0, the α -phase becomes decreasingly visible with the bilobe nanocrystal approaching an α -core/ β -shell structure. In the phase-separated region, η_2 becomes:

$$\eta_2 = \frac{2 \cdot r_\beta}{2 \cdot r_\alpha + 2 \cdot r_\beta} = \frac{r_\beta}{r_\alpha + r_\beta}. \quad (2.14)$$

Again simplifying, Eq. 2.14 becomes

$$\eta_2 = \frac{r_\beta}{r_\beta \left(\frac{1-f_\beta}{f_\beta} \right)^{1/3} + r_\beta} = \frac{1}{\left(\frac{1-f_\beta}{f_\beta} \right)^{1/3} + 1}. \quad (2.15)$$

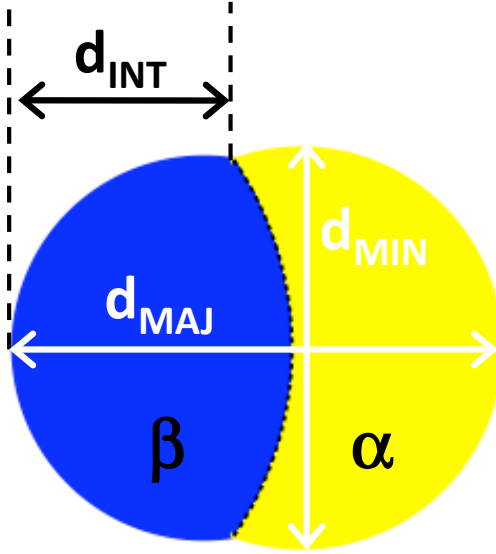


Figure 2.4. Cross-sectional view of the bi-lobe nanocrystal presented in Figure 2.3 with parameters $\{f_\beta, \gamma_1, \gamma_2\} = \{0.5, 1.5, 2.0\}$ is shown. Here, the important geometrical features, d_{MIN} , d_{MAJ} and d_{INT} are depicted.

Thus, in the phase-separated and core-shell regions, η_1 and η_2 remain fixed and are independent of the actual γ_1 and γ_2 -values. The minimum value of η_2 is again found in the phase-separated region and takes on a value of 0.5. In the region of bilobe stability, η_1 and η_2 depend on γ_1 and γ_2 .

Therefore, employing the above described strategy, one may calculate both η_1 and η_2 for each γ_1 and γ_2 doublet given the volume fraction of β . We calculate η_1 and η_2 for the equilibrium structures in the case of $f_\beta = 0.5$. An actual calculation is performed by varying γ_1 and γ_2 at an increment of 0.1 and an initial value of 0.1, producing a very large data set and will not be shown fully. However, an excerpt of this data is shown in Table 2.1. The first and second value in each set of brackets represent η_1 and η_2 , respectively.

First, η_1 will be examined more closely. A table similar to the one shown in Table 2.1 consisting of η_1 -values is calculated. Using this data, contours of equal η_1 -value can then be calculated and used to construct a contour plot of η_1 -values in the bilobe region. Results of this calculation are shown in Figure 2.5. As expected, for the case of equal volume fraction of α and β -phases, the contours are symmetric about the $\gamma_1 = \gamma_2$ line. Furthermore, it should be noted that as the values of γ_1 and γ_2 increase, the degree of sphericity increases, as expected. The limiting value for η_1 occurs when two completely phase separated spheres (region $\gamma_2 \leq -\gamma_1 + 1$) touch at one point. As mentioned above, for $f_\beta = 0.5$, the minimum value of η_1 is 0.5.

Next, the same analysis is applied to calculated η_2 -values. Results of the calculation are shown graphically in Figure 2.6. Again, the symmetry about the $\gamma_1 = \gamma_2$

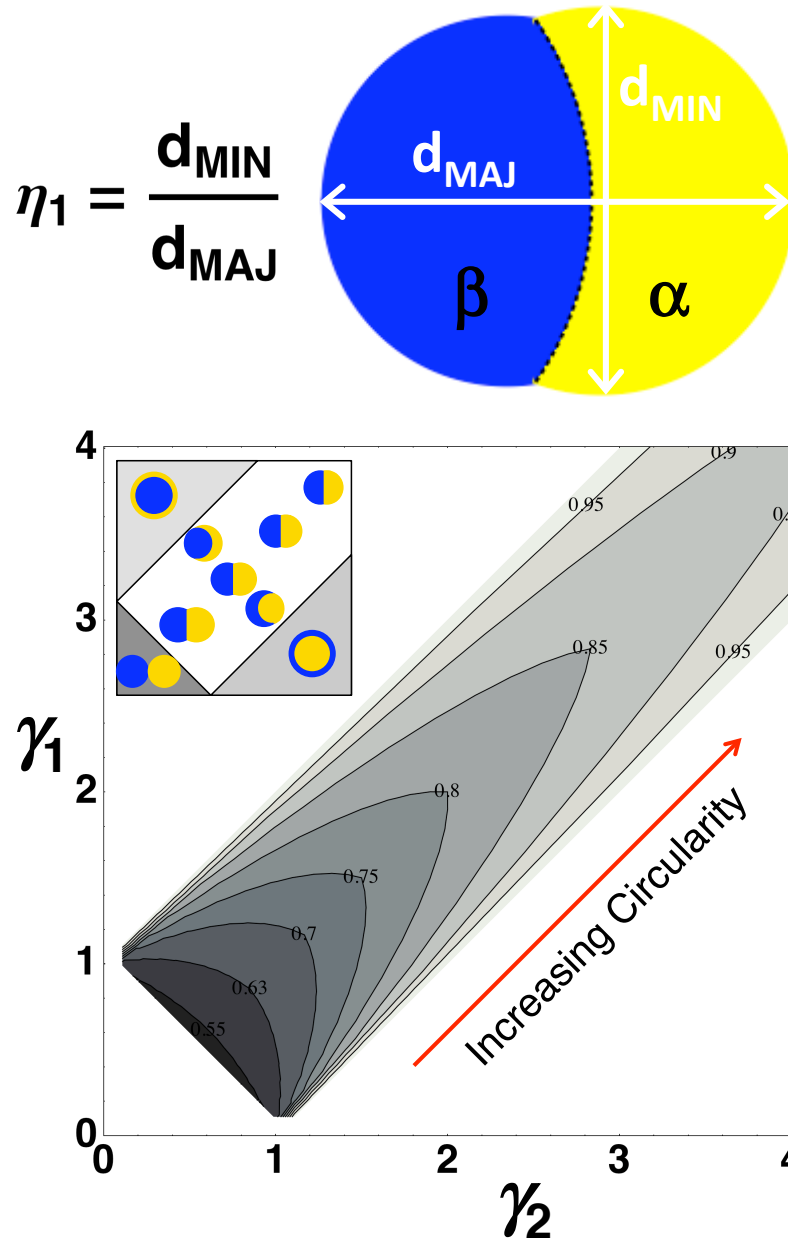


Figure 2.5. Considering a binary alloy particle of equal volume fractions of α and β -phases, a contour plot of $\eta_1 = d_{\text{MIN}}/d_{\text{MAJ}}$ is calculated and graphically presented. As the $\{\gamma_1, \gamma_2\}$ doublet increases, the particles become increasingly spherical. As expected for $f_\beta = 0.5$, the contours are symmetric about the line $\gamma_1 = \gamma_2$.

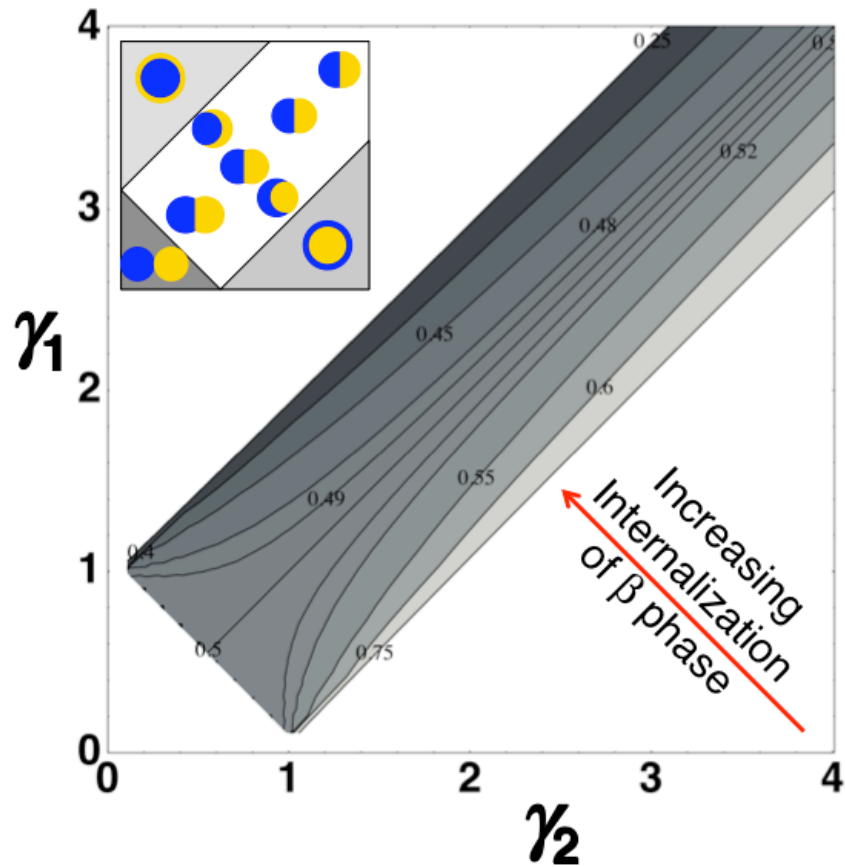
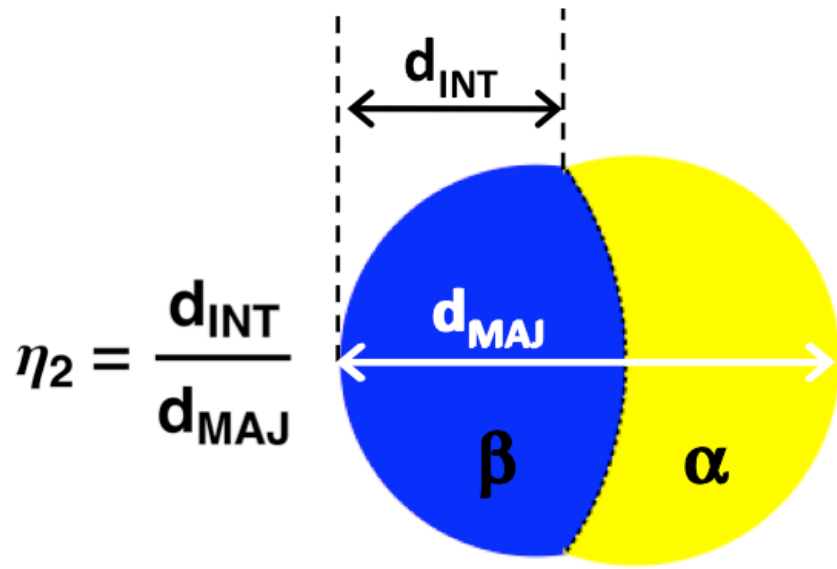


Figure 2.6. The contour plot of $\eta_2 = d_{INT}/d_{MAJ}$ is shown for a binary alloy particle of equal volume fractions of α and β -phases. η_2 is a measure of the internalization of the β -phase. Again, the contours are symmetric about the line $\gamma_1 = \gamma_2$.

line should be noted. Now, the contours range from 0 to 1 across the bilobe region and between the two, possible core-shell structures. In addition, the value of η_2 is 0.5 in the phase-separated region.

Now, as an example, assume a binary alloy system exists with the following parameters: $f_\beta = 0.5$, $\eta_1 = 0.80$ and $\eta_2 = 0.48$. Once both contour plots of η_1 and η_2 are constructed, one can superimpose the two plots over one another as demonstrated in Figure 2.7 for the case of $f_\beta = 0.5$. Next, the contours corresponding to $\eta_1 = 0.80$ and $\eta_2 = 0.48$ are highlighted. Notice, that the two contours intersect at one point, marked by the red star in Figure 2.7. This point corresponds to a unique set of $\{\gamma_1, \gamma_2\}$, determined in this example to be $\{1.95, 1.70\}$, indicating that $\gamma_{\alpha/M} = 1.95 \times \gamma_{\alpha/\beta}$ and $\gamma_{\beta/M} = 1.70 \times \gamma_{\alpha/\beta}$.

According to the theory elaborated above, one can measure and calculate the η_1 and η_2 values assuming that electron microscopy images of bilobe nanoparticles are available and the volume fraction of β -phase is known. Then, the γ_1 and γ_2 values can be determined. Even if none of the acting interface/surface energies are known, this analysis provides insight into which interface energies are largest in a given system. One should, however, note that in some regions of the structure map, it seems there is the possibility of one or more solutions (see regions close to doublets $\{\gamma_1, \gamma_2\} = \{1, 0\}$ and $\{\gamma_1, \gamma_2\} = \{0, 1\}$). If the measured values predict η -values leading to a solution in these regions, a more careful analysis is required to pinpoint the exact values of γ_1 and γ_2 . This can be achieved by more precise measurements and an increase in numerical accuracy of the solutions. However, limitations in both may lead to a region of possible solutions.

However, most systems will likely fall into the region where there is only one obvious solution. Then, if one of the interface/surface energies is known, the above-mentioned analysis may be used to determine the remaining two interface/surface energies. In the following chapters, two binary alloy systems displaying the above described bilobe structure are investigated and the preceding analysis is performed.

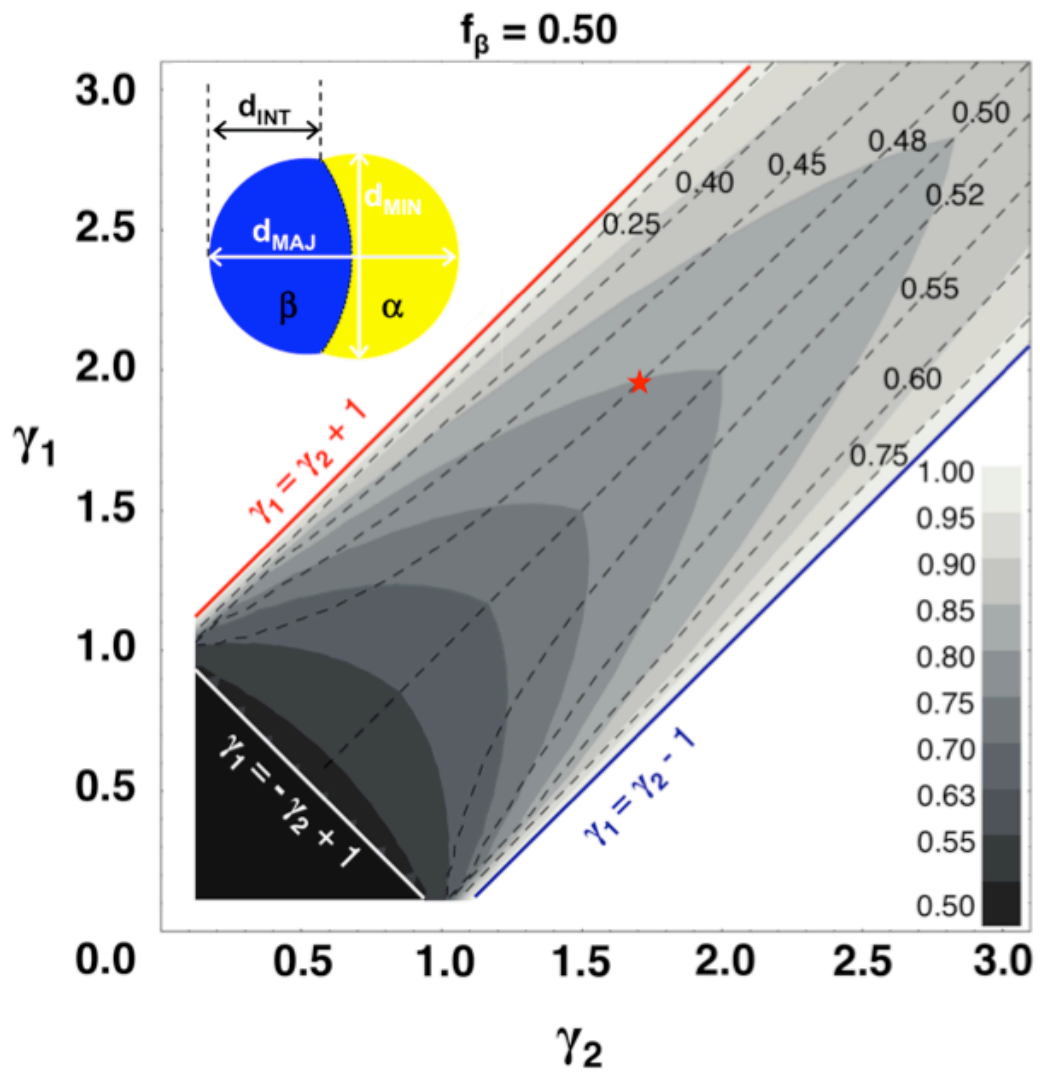


Figure 2.7. Overlaid contour plots of η_1 (shaded contours) and η_2 (dashed lines) are shown. The red star represents the example discussed in the text.

Table 2.1. Excerpt of a Data Set: $\{\eta_1, \eta_2\}$ -Values for $f_\beta = 0.5$

		γ_1							
		0.5	1.0	1.5	2.0	2.5	3.0	3.5	4.0
γ_2	0.5	{0.67,0.67}	{0.63,0.510341}	{1,1}	{1,1}	{1,1}	{1,1}	{1,1}	{1,1}
	1.0	{0.63,0.49}	{0.67,0.5}	{0.76,0.53}	{1,1}	{1,1}	{1,1}	{1,1}	{1,1}
	1.5	{1,0}	{0.76,0.47}	{0.75,0.5}	{0.82,0.55}	{1,1}	{1,1}	{1,1}	{1,1}
	2.0	{1,0}	{1,0}	{0.82,0.45}	{0.8,0.5}	{0.85,0.55}	{1,1}	{1,1}	{1,1}
	2.5	{1,0}	{1,0}	{1,0}	{0.85,0.45}	{0.83,0.5}	{0.88,0.56}	{1,1}	{1,1}
	3.0	{1,0}	{1,0}	{1,0}	{1,0}	{0.88,0.44}	{0.86,0.5}	{0.90,0.56}	{1,1}
	3.5	{1,0}	{1,0}	{1,0}	{1,0}	{1,0}	{0.90,0.44}	{0.88,0.5}	{0.91,0.57}
	4.0	{1,0}	{1,0}	{1,0}	{1,0}	{1,0}	{1,0}	{0.91,0.43}	{0.89,0.5}

Chapter 3

Application of Bilobe Analysis to Two Experimental Systems

Previously, a geometry based approach to determine the dimensionless interface energies of bilobe nanostructures was introduced. In the following paragraphs, two cases of experimentally available embedded binary eutectic alloy nanostructures (BEANs) will be investigated using the described theory. Both SnGe and AuGe BEANs are fabricated using ion implantation/co-sputtering within a SiO₂ matrix and post-fabrication thermal annealing.(60; 24) Ion beam synthesis (IBS), a convenient method for the production of embedded nanoclusters, is typically employed when control over quantity, purity, and desired isotopes of the embedded species is of special importance.(40; 70; 44; 57) Both bright field (BF) and high angle annular dark field (HAADF) imaging are used to characterize the resulting nanostructures. Representative TEM images of SnGe and AuGe BEANs are shown in Figures 3.1 and 3.7. The annealing step clearly results in the formation of bilobe nanostructures (for both systems), providing adequate experimental parameters that warrant the use of the geometry based analysis.

3.1 SnGe

Based on the implantation, the Ge:Sn ratio is estimated to be 3:1 (25 at. % Sn).(60) Additionally, the average radius of the resulting SnGe BEANs was measured to be 25 nm. A representative TEM image of the resulting BEANs is shown in Figure 3.1. Clearly, some of the nanocrystals are composed of two distinct lobes as evidenced by the contrast difference in the high-angle annular dark-field (HAADF) image. The

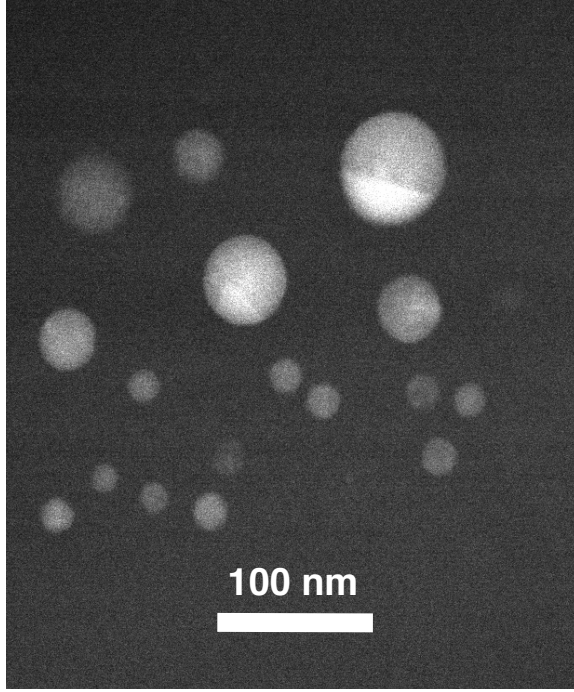


Figure 3.1. Representative TEM image of SnGe bilobe nanocrystals used in determination of interface energy from the characterized bilobe geometry.

rest of the nanoparticles are assumed to be composed of pure Ge due to the non-uniform implantation conditions. In this technique, higher atomic number elements appear brighter than low atomic number elements. Consequently, the bright region is assumed to be composed of Sn, while the lower contrast (with respect to the SiO_2 matrix) lobe is composed of Ge. It should be noted that the brighter lobe is also the smaller lobe of the bilobe nanocrystals, which is consistent with the estimated alloy composition.

To perform the analysis, the α -phase will denote the Ge rich phase, while the secondary phase (in this case the Sn rich phase) will be the β -phase. Accordingly, the SiO_2 represents the matrix, M -phase. As described in the preceding chapter, η_1 and η_2 are measured and calculated for each nanocrystal from the TEM images. As a consequence of the implantation conditions, a random orientation of nanocrystals throughout the sample, which is evidenced by a range of measured η_1 and η_2 values, is expected.

To properly identify the true aspect ratios, we must take a closer look at the bilobe nanocrystals. Consider a bilobe with one lobe of radius R centered at $\{x, y, z\} = \{0, 0, 0\}$ and a second lobe of radius r centered at $\{x, y, z\} = \{x_c, 0, 0\}$, as shown in Figure 3.2. In this case, R is greater than r . Subsequently, η_1 , as defined earlier, is calculated to be $\eta_1 = \frac{2R}{R+x_c+r}$. Now imagine the bilobe structure is rotated by some angle θ about the y -axis. The projection of the center of the smaller bilobe then becomes $x_c \cdot \cos(\theta)$, and thus, $\eta_1 = \frac{2R}{R+x_c \cdot \cos(\theta)+r}$. Accordingly, if $x_c \cdot \cos(\theta) + r \leq R$,

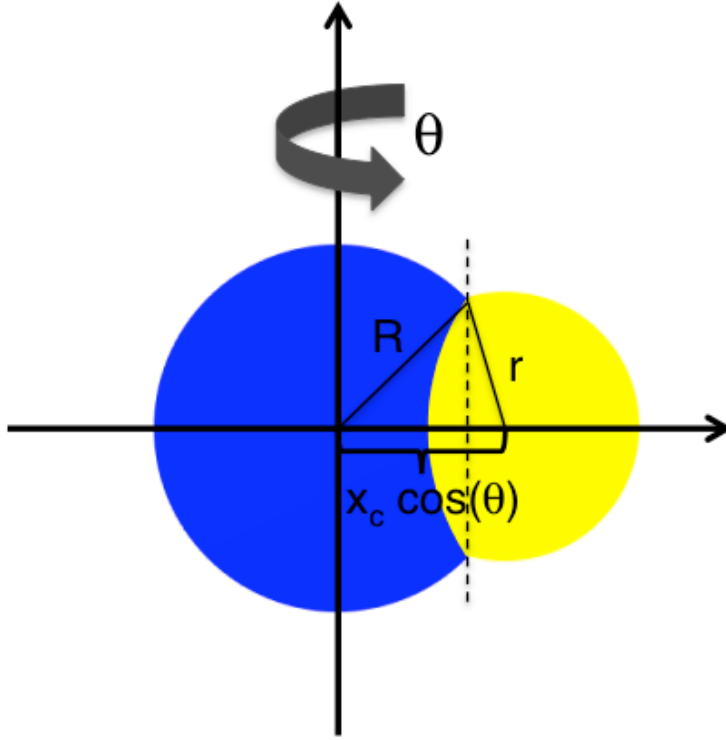


Figure 3.2. A bilobe nanocrystal is shown with one lobe (radius R) centered at $\{x, y, z\} = \{0, 0, 0\}$ and a second lobe centered at $\{x, y, z\} = \{x_c, 0, 0\}$. To investigate the range of possible η_1 -values, a rotation about the y -axis is considered. As the bilobe undergoes rotation by θ -degrees, the projection of the center of the second bilobe onto the x -axis becomes $x_c \cdot \cos(\theta)$.

the secondary bilobe has rotated out of view, and η_1 becomes 1 until the lobe has rotated sufficiently to be seen on the left-hand side of the primary lobe.

As an example, we let $R = 1$, $r = 0.725$ and $x_c = 0.92$. η_1 is plotted graphically in Figure 3.3 as a function of rotational angle, θ , about the y -axis. The minimum η_1 -value is calculated to be 0.756144, which is also evidenced by the local minimum at $\theta = 0$. As expected, this minimum is also found at $\theta = \pi$. Also, as described above, there are two regions of θ -values for which η_1 must equal 1. In the first region, the smaller lobe is hidden behind the larger lobe, and thus both the minor and the major axis are equal to $2R$. In the second region, the secondary lobe is visible; however, the minor and major axis, as defined previously, must still both equal $2R$.

Consequently, when examining a collection of randomly oriented bilobe structures, the structure with the minimum value of η_1 represents the nanocrystal, that is most closely oriented to the perfect side-on view of the bilobe. Analysis of possible η_2 -values leads to a similar result. Therefore, under the assumption of uniform composition (this assumption will be addressed by the use of error bars, see below), the bilobe

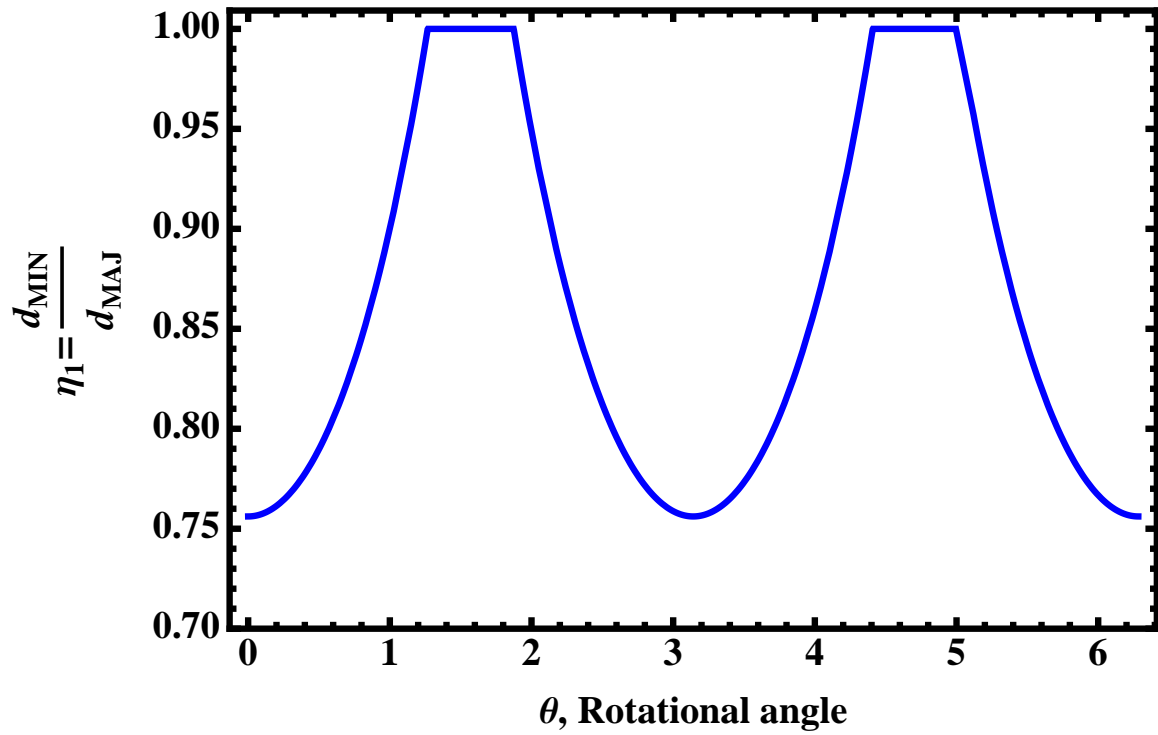


Figure 3.3. η_1 can take on a spread of possible values depending on the degree of rotation, θ . However, the maximum value must be equal to 1, while the minimum value represents an advantageously oriented bilobe.

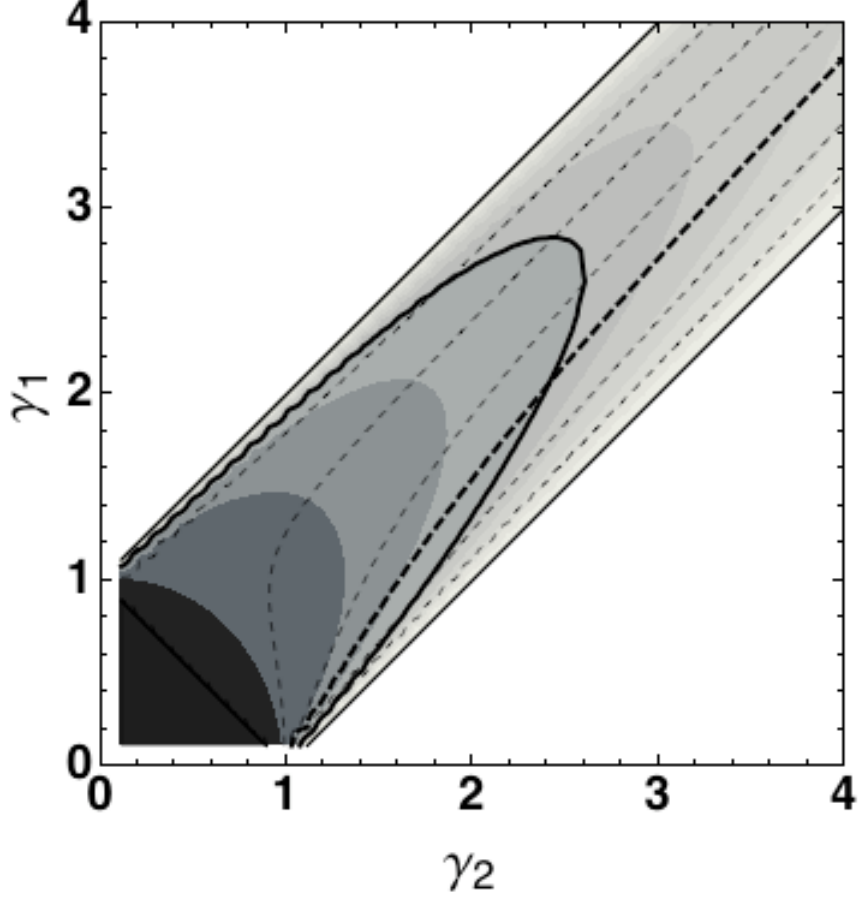


Figure 3.4. Contour plot corresponding to a volume fraction of $f_\beta = 0.28$. The contours $\eta_1^{SnGe} = 0.88$ and $\eta_2^{SnGe} = 0.67$ are highlighted. The intersection of the two contours lies at $\gamma_1 = 2.31$ and $\gamma_2 = 2.43$.

displaying the smallest values of η_1 and η_2 are chosen to represent the actual values of η_1 and η_2 in a given sample.

In the SnGe-samples, the aspect ratios are determined to be $\eta_1^{SnGe} = 0.88$, $\eta_2^{SnGe} = 0.67$. The bilobe composition was estimated to be 25 at. % Sn, which corresponds to a volume fraction of $f_\beta = 0.28$ Sn. Figure 3.4 shows the corresponding contour plot at $f_\beta = 0.28$ with the contours $\eta_1^{SnGe} = 0.88$ and $\eta_2^{SnGe} = 0.67$ highlighted. It is clear from the calculation that the contours corresponding to the measured aspect ratios cross at one point: $\gamma_1 = 2.31$ and $\gamma_2 = 2.43$.

Although the microscopy experiments are performed at room temperature, samples undergo thermal treatment to stabilize the bilobe structure. Therefore, it is possible that the observed structures are formed at an elevated temperature and set by the freezing of the matrix during subsequent quenching, which would indicate that the experimentally observed bilobe structures are not the equilibrium structure at room temperature. It is possible that the equilibrium morphology at room temperature is still a bilobe structure, but with possibly different aspect ratios.

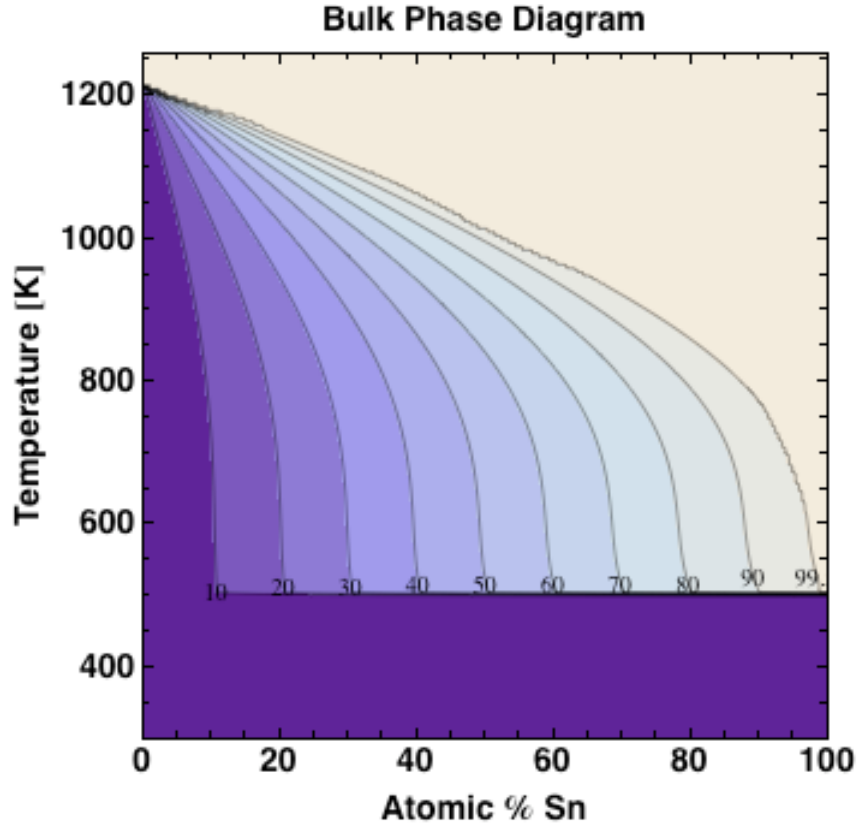


Figure 3.5. The equilibrium bulk phase diagram of the SnGe system is presented. Contours represent the volume fraction of the liquid phase in the system.

To further investigate this setting theory, the equilibrium bulk SnGe phase diagram is employed. As described above, samples with 25 at. % Sn are heated to 900 °C for 1 hr. At this temperature, the bulk phase diagram (see Figure 3.5) predicts the liquid phase for the composition under investigation. As the temperature is decreased to $T = 1130$ K, the liquidus line is reached, thus indicating the onset of solidification and a small volume solid nucleates from the binary alloy liquid. As the temperature decreases below the liquidus temperature, the fractional amount of solid in the system increases according to the lever rule.

In the case of the SnGe system, a very Ge-rich phase is solidified leaving a liquid phase of increasing Sn concentration. In Figure 3.5, contours represent the fractional amount of liquid expected in the system. The solid, vertical line represents the investigated composition. As the temperature decreases, the intersection between the vertical line and the contour represents the fraction of liquid present. The fraction of solid is then defined as $1 - f_{liquid}$. As discussed above, the η_1 and η_2 contour plots change for differing volume fractions of the β -phase. Thus, as the temperature is decreased, the volume fraction of the liquid phase changes (the liquid phase will represent the β -phase), and as such contour plots differ as a function of temperature. Therefore, the intersection of the two contours changes and the determined γ_1 and γ_2 values are temperature dependent. Consequently, a contour plot according to the

volume fraction of β -phase must be constructed and analyzed for every temperature. The result is a table consisting of temperature, γ_1 and γ_2 . Reconsider the definitions of γ_1 and γ_2 ,

$$\gamma_1 = \gamma_{\alpha/M} / \gamma_{\alpha/\beta} \quad (3.1)$$

$$\gamma_2 = \gamma_{\beta/M} / \gamma_{\alpha/\beta}. \quad (3.2)$$

There are three interface energies involved in the system at each temperature and according to our previous definition, $\gamma_{\alpha/M}$ is $\gamma_{Sn_xGe_{1-x}^{liq}/SiO_2}$, $\gamma_{\beta/M}$ is γ_{Ge^{sol}/SiO_2} and $\gamma_{\alpha/\beta}$ is $\gamma_{Sn_xGe_{1-x}^{liq}/Ge^{sol}}$. Thus, if one of the interface energies is known, the other two interface energies can be calculated as a function of temperature.

Fortunately, Naidich and Perevertailo determined the composition dependent wetting properties of SnGe-liquids on Ge-solid.(42) These analyses provide us with one of the relevant interface energies within the system and allows us to use the analysis described in Chapter 2 to determine the remaining interface energies. The employed equations are as follows:

$$\gamma_{Ge^{sol}/SiO_2} = \gamma_1(T) \times \gamma_{Sn_xGe_{1-x}^{liq}/Ge^{sol}} \quad (3.3)$$

$$\gamma_{Sn_xGe_{1-x}^{liq}/SiO_2} = \gamma_2(T) \times \gamma_{Sn_xGe_{1-x}^{liq}/Ge^{sol}}, \quad (3.4)$$

with $\gamma_{Sn_xGe_{1-x}^{liq}/Ge^{sol}}$ determined experimentally.(42) γ_{Ge^{sol}/SiO_2} and $\gamma_{Sn_xGe_{1-x}^{liq}/SiO_2}$ can now be calculated as a function of temperature. Results of this calculation are shown in Figure 3.6, where γ_{Ge^{sol}/SiO_2} and $\gamma_{Sn_xGe_{1-x}^{liq}/SiO_2}$ are represented in black and blue, respectively. It is clear from this figure that all temperatures investigated, result in reasonable values for the interface energies.

As mentioned before, the calculations performed thus far have been under the assumption of uniform and known composition. To adjust for the possibility that the composition of the individual bilobes is not equal to the overall implantation composition, error bars will be calculated. This is achieved by measuring and calculating the visible portion of the two caps in the TEM images and calculating the volume fraction of Sn, which can subsequently be converted to atomic fraction of Sn in the particle. In the case of SnGe particles, the atomic fraction of Sn is calculated to be 0.22, while the implantation conditions predict 0.25. Thus, an error bar of 3 at. % Sn is applied to the calculation. It should be noted that the values of γ_{Ge^{sol}/SiO_2} and $\gamma_{Sn_xGe_{1-x}^{liq}/SiO_2}$ change as a function of temperature over a substantial range (0.3-1.8 $\frac{J}{m^2}$), and therefore no definite prediction can yet be made.

3.2 AuGe

A second system was also investigated using a similar methodology: the AuGe-system. Samples are prepared via cosputtering method of SiO₂ and Au and subsequent ion implantation of Ge as described by Shin et al.(60) A Au to Ge ratio of 3:17

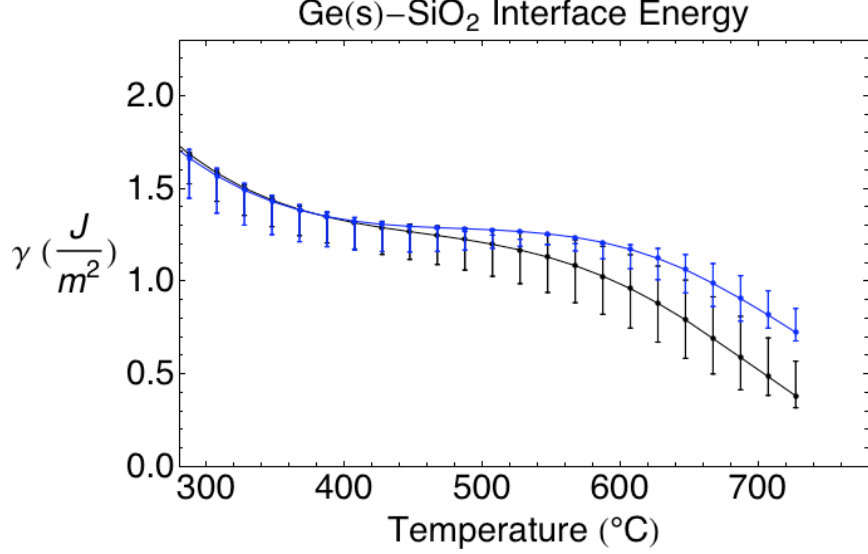


Figure 3.6. γ_{Ge^{sol}/SiO_2} and $\gamma_{Sn_xGe_{1-x}^{liq}/SiO_2}$ calculated as a function of temperature. γ_{Ge^{sol}/SiO_2} is represented by the black line, while $\gamma_{Sn_xGe_{1-x}^{liq}/SiO_2}$ is shown in blue.

or 15 at.% Au is achieved, which corresponds to a volume fraction of Au of $f_\beta = 0.12$. Similar to the SnGe-system, AuGe bilobe structures are found upon thermal annealing of samples at 900 °C for 1 hr (see Figure 3.7). Again, the bilobes consist of a Ge-rich larger lobe, and a Au-rich smaller lobe. Careful measurement of the AuGe bilobes determines $\eta_1^{GeAu} = 0.94$ and $\eta_2^{GeAu} = 0.71$. These values clearly differ from those measured in the SnGe-system indicating that the interface energies and volume fraction of β -phase must be different. Again, the two contour plots for $f_\beta = 0.12$ are constructed and the intersection of contours $\eta_1 = 0.94$ and $\eta_2 = 0.71$ is found. The resulting contour plot is shown in Figure 3.8. The intersection is found at $\gamma_1 = 2.95$ and $\gamma_2 = 2.11$.

However, as previously discussed, the bilobe structure may have been formed at an elevated temperature during the solidification process. Consequently, as described before, the temperature dependent γ_1 and γ_2 values are determined through the use of the AuGe bulk phase diagram. Here, the acting equations are:

$$\gamma_{Ge^{sol}/SiO_2} = \gamma_1(T) \times \gamma_{Au_xGe_{1-x}^{liq}/Ge^{sol}} \quad (3.5)$$

$$\gamma_{Au_xGe_{1-x}^{liq}/SiO_2} = \gamma_2(T) \times \gamma_{Au_xGe_{1-x}^{liq}/Ge^{sol}}. \quad (3.6)$$

Again, Naidich and Perevertailo studied the wetting properties of AuGe-liquids on Ge-solid: $\gamma_{Au_xGe_{1-x}^{liq}/Ge^{sol}}$.⁽⁴³⁾ This allows us to calculate both γ_{Ge^{sol}/SiO_2} and $\gamma_{Au_xGe_{1-x}^{liq}/SiO_2}$ as a function of temperature. It should be noted that the two systems studied share a common interfacial energy: $\gamma_{Ge(s)/SiO_2}$. Assuming that the set temperature is the same for both systems, comparison of this common interface energy as a function of temperature should enable identification of the set temperature. The temperature for which the two systems yield identical $\gamma_{Ge(s)/SiO_2}$ is the setting temperature.

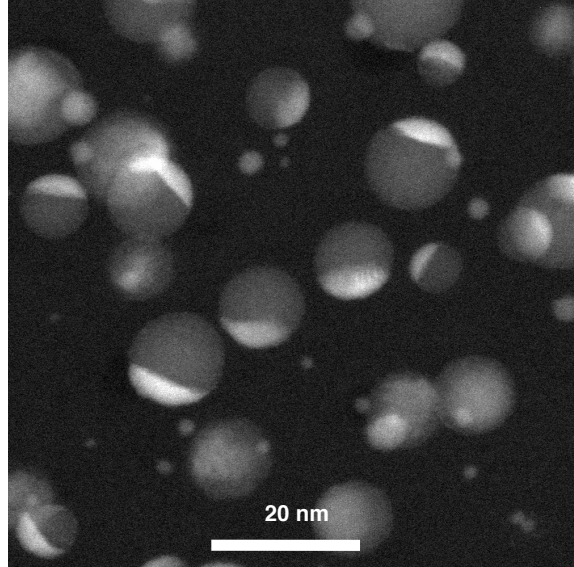


Figure 3.7. A representative TEM image of AuGe nanoparticles is shown. Clearly, the bilobe structure has formed.

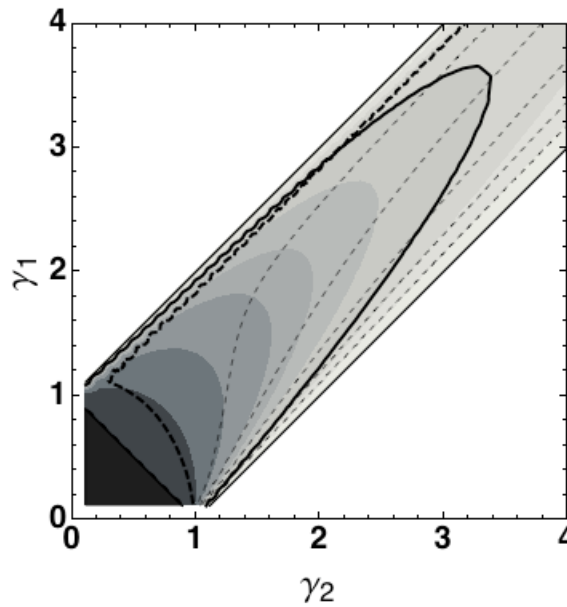


Figure 3.8. Contour plot corresponding to a volume fraction of $f_\beta = 0.28$. The contours $\eta_1^{SnGe} = 0.94$ and $\eta_2^{SnGe} = 0.71$ are highlighted. The intersection of the two contours indicates acting values of $\gamma_1 = 2.31$ and $\gamma_2 = 2.43$.

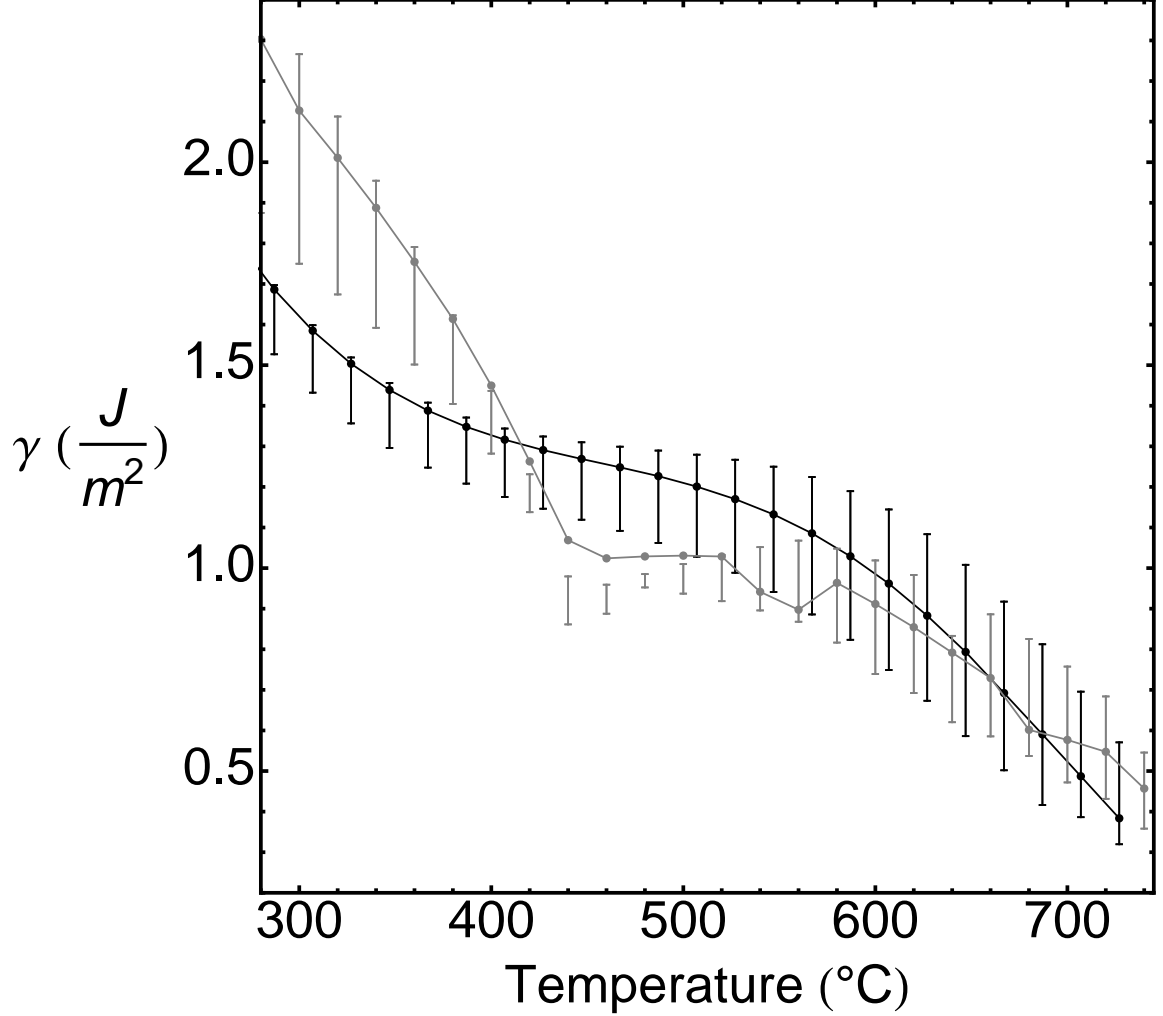


Figure 3.9. γ_{Ge^{sol}/SiO_2} plotted as a function of temperature. The black line represents the results calculated from the SnGe system, while the gray line is calculated from the AuGe system.

In Figure 3.9, the interface energy γ_{Ge^{sol}/SiO_2} is plotted as a function of temperature calculated using both the SnGe (black line) and AuGe (gray line) systems. Again, the error bars are calculated using the method described above.

It is clearly evident that both systems predict a Ge^{sol}/SiO_2 interface energy over a similar range. The two predictions cross at two temperatures, 415 and 660 °C and thus the corresponding predicted interface energies are 1.30 and $0.73 \frac{J}{m^2}$. At all temperatures above 415 °C, the error bars for both systems overlap substantially. A question arises: is there a mechanism acting at temperatures above 415 °C that would cause the theorized setting and further pinpoint the exact setting temperature.

A previous study on Ge nanocrystals embedded in silica by IBS (using the same method as in the current experiment) showed that stress relaxation of the embedded clusters did not significantly occur at a temperature of 600 °C even after long (greater

than 24 hrs) annealing times.(58) At further elevated temperatures, stress relaxation was in fact observed, which would indicate that the silica matrix no longer allows for a change in shape of the nanocrystals at temperatures below ~ 600 °C. Additionally, McGraw(39) and Belousov *et al.*(6) observed a marked increase in the elastic modulus of industrial glasses at temperatures below ~ 580 °C. While in the current experiment, the matrix material is SiO_2 , it is not unthinkable that the implantation or cosputtering of Sn/Au/Ge into the matrix causes a similar elastic behavior as that observed in the impure industrial glasses. Considering these experiments, it seems reasonable to assume that the bilobe structure is set at ~ 600 °C.

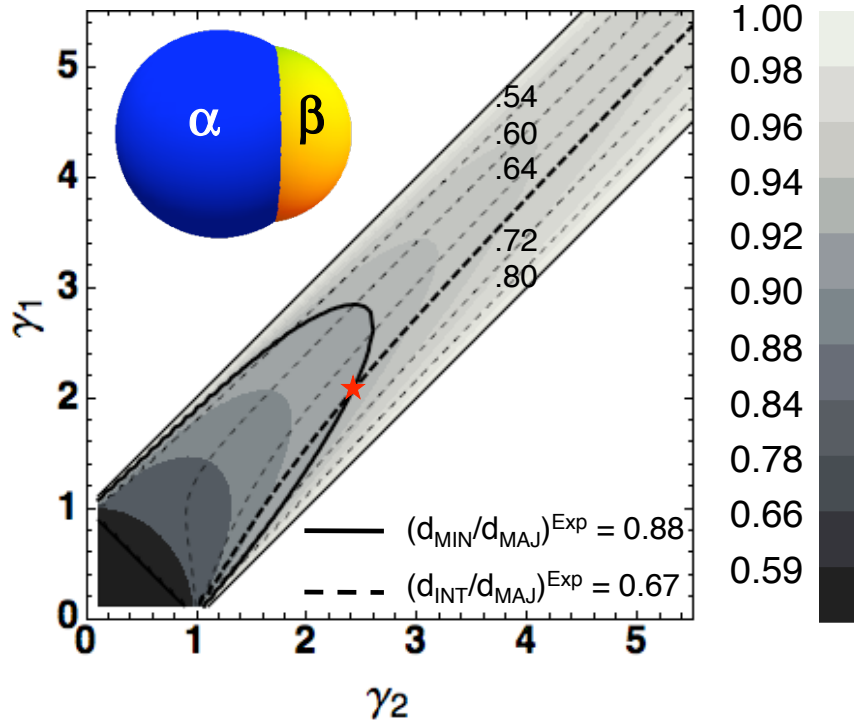
Next, the systems are evaluated at $T = 600$ °C. At this temperature, the bulk SnGe phase diagram predicts a system containing Ge^{sol} and a $\text{Ge}_{0.22}\text{Sn}_{0.78}^{liq}$. Also, the volume fraction of liquid present is determined to be $f_\beta = 0.31$. Figure 3.10 shows the resulting contour plot at this volume fraction. The intersection of the contours is emphasized by the star and is found at $\gamma_1 = 2.05$ and $\gamma_2 = 2.41$. At this composition/temperature, Naidich and Perevertailo determined $\gamma_{\text{Sn}_{0.78}\text{Ge}_{0.22}^{liq}/\text{Ge}^{sol}}$ to be equal to $\sim 0.5 \frac{J}{m^2}$ leading to $\gamma_{\text{Ge}^{sol}/\text{SiO}_2} = 0.99 \frac{J}{m^2}$ and $\gamma_{\text{Sn}_{0.78}\text{Ge}_{0.22}^{liq}/\text{SiO}_2} = 1.20 \frac{J}{m^2}$.

The AuGe system predicts Ge^{sol} and a $\text{Au}_{0.53}\text{Ge}_{0.47}^{liq}$ with a volume fraction of liquid equal to $f_\beta = 0.33$. The resulting contour plot is shown in Figure 3.11 and the contour intersection may be found at $\gamma_1 = 3.71$ and $\gamma_2 = 4.26$. Combined with the value of $\gamma_{\text{Au}_{0.53}\text{Ge}_{0.47}^{liq}/\text{Ge}^{sol}}$ ($\sim 0.22 \frac{J}{m^2}$)(43), $\gamma_{\text{Ge}^{sol}/\text{SiO}_2}$ and $\gamma_{\text{Au}_{0.53}\text{Ge}_{0.47}^{liq}/\text{SiO}_2}$ are calculated to be equal to 0.82 and $0.94 \frac{J}{m^2}$, respectively.

Both Figures 3.10 and 3.11 are shown with inserts of simulated BEANs using the parameters determined at $T = 600$ °C. It should be noted that these bilobes show a striking similarity to the experimentally observed structures, indicating that the determined parameters are reasonable. Furthermore, the value of $\gamma_{\text{Ge}^{sol}/\text{SiO}_2}$ is determined to be $\sim 0.82 - 0.99 \frac{J}{m^2}$, which is in good agreement with prior estimates for the Ge^{sol} - SiO_2 interface energy of 0.7-0.9 $\frac{J}{m^2}$.(70; 31)

One final observation should be considered: size effect. As noted previously, the average radius of the SnGe bi-lobe nanocrystals is 25 nm. Comparison of the two sets of TEM images clearly shows that the resulting AuGe bilobes are considerably smaller: 5 nm average radius. It is therefore possible that a size has been reached, especially in the case of the AuGe nanocrystals, at which the bulk phase diagram is no longer applicable. If size effects are relevant, the size dependent phase diagrams must be calculated. Consequently, if the liquidus and solidus lines or the eutectic point shift due to the small size of the binary alloy system, the temperature dependent volume fractions of β -phase will change. This may result in a change of calculated $\gamma_{\text{Ge}^{sol}/\text{SiO}_2}$ values. In the following chapters, a procedure to calculate the size dependent phase diagrams will be described.

GeSn system



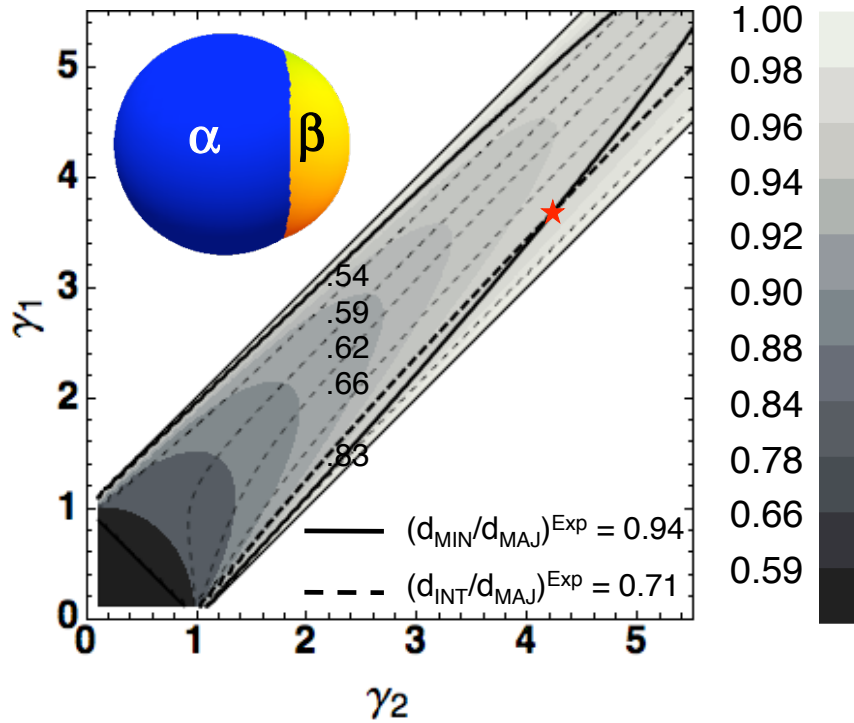
$f_{\beta} = 31\%:$
 α – phase : Ge (\perp)
 β – phase: $Ge_{0.22}Sn_{0.78}$ (ℓ)

$\gamma_1 = 2.05$
 $\gamma_2 = 2.41$

$\gamma_{\alpha/\beta} = 0.50 \text{ J/m}^2$
 $\gamma_{\alpha/M} = 0.99 \text{ J/m}^2$
 $\gamma_{\beta/M} = 1.20 \text{ J/m}^2$

Figure 3.10. Contour plot for the SnGe system at $T = 600 \text{ }^{\circ}\text{C}$ for which f_{β} is predicted to be equal to 0.31.

AuGe system



$f_{\beta} = 33\%:$
 α – phase: Ge (ℓ)
 β – phase: Au_{0.53}Ge_{0.47} (ℓ)

$\gamma_1 = 3.71$
 $\gamma_2 = 4.26$

$\gamma_{\alpha/\beta} = 0.22 \text{ J/m}^2$
 $\gamma_{\alpha/M} = 0.82 \text{ J/m}^2$
 $\gamma_{\beta/M} = 0.94 \text{ J/m}^2$

Figure 3.11. Contour plot for the AuGe system at $T = 600 \text{ }^{\circ}\text{C}$ for which f_{β} is predicted to be equal to 0.33.

Chapter 4

Application of Butler's Equation to SnGe and AuGe Systems

As mentioned previously, the properties of the surfaces and interfaces of a system become increasingly important as a result of a decreasing system size. Crystal sizes on the order of nanometers (10^{-9} m) and below show significant size dependent properties.(13; 2; 1; 54; 70; 30) Therefore, it becomes important to predict the phase diagrams of nanoscale binary alloy systems, as a deviation from bulk behavior is possible, if not expected.(11; 64; 69; 68; 8; 63; 36; 15; 16; 48; 67) Thus, we must first turn our attention to the determination and evaluation of the surface/interface energies acting in our model systems, SnGe and AuGe. To evaluate the phase diagrams, a *priori* knowledge of $\gamma_{A_xB_{1-x}}$, the surface/interface energy of a binary alloy liquid of composition A_xB_{1-x} (A and B represent the two component elements), is required. Often, a concentration weighted average of the surface/interface energies of the individual elements is used.(63) Subsequently, the surface tension is calculated as follows:

$$\gamma_{A_xB_{1-x}} = x \cdot \gamma_A + (1 - x) \cdot \gamma_B \quad (4.1)$$

This method assumes that the composition of the surface is identical to that of the bulk and that the two atom types contribute to the surface tension similarly, whether or not they are surrounded by atoms of the same or different type. In elemental liquids, the surface composition is necessarily equal to the bulk composition of the liquid; however, in alloys this is not necessarily true. Due to element specific surface activities, the composition of the surface may vary significantly from that of the bulk. Thus, the contribution to the surface tension of the two elements may deviate from the linear approximation made by assuming a concentration weighted average.

To address this, Butler's equation is often employed.(9; 4) This technique seeks

to express the surface tension in terms of equilibrium between the chemical potential of the bulk material (with bulk composition) and that of its' surface layer (possible different composition).(38; 64; 65; 15; 16; 36; 18; 71) Considering a binary alloy composed of components A and B , Butler's equation is expressed as follows:

$$\sigma^L = \sigma_A^L + \frac{RT}{A_A} \ln\left(\frac{x_A^s}{x_A^b}\right) + \frac{1}{A_A} \overline{G_A^{Ex,s}} - \frac{1}{A_A} \overline{G_A^{Ex,b}} \quad (4.2)$$

$$\sigma^L = \sigma_B^L + \frac{RT}{A_B} \ln\left(\frac{x_B^s}{x_B^b}\right) + \frac{1}{A_B} \overline{G_B^{Ex,s}} - \frac{1}{A_B} \overline{G_B^{Ex,b}}, \quad (4.3)$$

where σ^L is the surface tension of the alloy, $\sigma_{A,B}^L$ is the surface tension of the pure liquid components A or B, $x_{A,B}^{s,b}$ is the mole fraction of component A or B in the surface or bulk and $A_{A,B}$ is the relative surface areas of components A or B. $\overline{G_A^{Ex,b}}$ and $\overline{G_A^{Ex,s}}$ are the partial molar excess Gibbs' free energies of element A in the bulk and surface, respectively. A B in the subscript denotes element B , whereas a b in the superscript refers to the bulk of the system.

To clarify, the above form of Butler's equation (Equations 4.2 and 4.3) can be rewritten as:

$$RT \ln(x_A^s) + \overline{G_A^{Ex,s}} + A_A(\sigma_A^L - \sigma^L) = RT \ln(x_A^b) + \overline{G_A^{Ex,b}} \quad (4.4)$$

$$RT \ln(x_B^s) + \overline{G_B^{Ex,s}} + A_B(\sigma_B^L - \sigma^L) = RT \ln(x_B^b) + \overline{G_B^{Ex,b}}, \quad (4.5)$$

where R is the universal gas constant equal to $8.3144621 \frac{J}{mol \cdot K}$ and T represents the temperature in *Kelvin*. In the above equations, the left-hand side represents the chemical potential of the surface, while the right-hand side represents the chemical potential of the bulk. Therefore, Butler's equations assumes equilibrium between the bulk of some composition and the surface with a differing composition. Furthermore, the relative surface areas of the components A and B are calculated using the their molar liquid volumes, $V_{A,B}^L$, as follows:

$$A_{A,B}^L = l \cdot N_0^{1/3} (V_{A,B}^L)^{2/3}. \quad (4.6)$$

In this equation, l is a fitting parameter that recalculates the area of the liquid surface layer assuming a close-packed structure and equal to 1.091(4; 19; 20; 59) and N_0 represents Avogadro's number equal to 6.0233×10^{23} . The excess partial molar Gibbs free energies of components A or B in the bulk, $\overline{G_A^{Ex,b}}(T, x_B^b)$ or $\overline{G_B^{Ex,b}}(T, x_B^b)$, can be calculated using:

$$\overline{G_A^{Ex,b}}(T, x_B^b) = G^{Ex,L} - x_B^b \frac{\partial G^{Ex,L}}{\partial x_B^b} \quad (4.7)$$

$$\overline{G_B^{Ex,b}}(T, x_B^b) = G^{Ex,L} + (1 - x_B^b) \frac{\partial G^{Ex,L}}{\partial x_B^b}. \quad (4.8)$$

x_B^b represents the molar fraction of component B in the bulk of the liquid. The partial molar excess Gibbs free energy of components A and B in the surface is estimated using:

$$\overline{G_{A,B}^{Ex,s}}(T, x_B^s) = \beta \cdot \overline{G_{A,B}^{Ex,b}}(T, x_B^s). \quad (4.9)$$

This form assumes that the partial molar Gibbs free energy of a component at the surface is a fractional portion of the partial molar Gibbs free energy of the same component in the bulk. β represents the ratio of coordination number in surface to bulk. In general for liquid alloys, β is set equal to 0.75 or 0.83, which assumes the coordination number in the bulk is 12 and at the surface either 9 or 10.

The excess Gibbs energy of mixing of an alloy can be modeled using Redlich-Kister expansions:(53)

$$G^{Ex,L} = x_A^b \cdot x_B^b \{L_0 + L_1(x_A^b - x_B^b) + L_2(x_A^b - x_B^b)^2 + L_3(x_A^b - x_B^b)^3 + \dots + L_i(x_A^b - x_B^b)^i\}. \quad (4.10)$$

The interaction parameters, L_i , must be found in the appropriate thermodynamic databases for each system under investigation.

All relevant data for the calculation of surface tensions of AuGe and SnGe liquid alloys is summarized in Tables 4.1-4.3. Table 4.1 lists values for the surface tension of Au, Ge and Sn liquids available in the literature. When available, temperature dependent properties are tabulated. In the case of Sn, measurements of the surface tension at various temperatures are used to construct a linear best fit equation. This equation is also tabulated. If multiple measurements are available in the literature (as in the case of Au and Sn), subsequent calculations will be carried out multiple times. Table 4.2 lists available data for the molar volumes of the elemental liquids. If temperature dependent data is not available, the available data will be used and assumed not to depend on temperature. Finally, Table 4.3 lists the interaction parameters for both the AuGe and SnGe systems. In both cases, the interaction parameters are listed as function of Ge concentration.

Table 4.1. σ , Surface Tension (J/m^2) of Elemental Liquid

		Ref.
Au	$1.169 - 0.25 \times 10^{-3}(T - 1336.15)$	(27)
	$1.138 - 1.9 \times 10^{-3}(T - 1337)$	(26)
	$1.33 - 1.4 \times 10^{-4}T$	(48)
Sn	$(0.531 - 0.151 \times 10^{-3}(T - 505))$	(37)
	$(0.5828 - 0.0834 \times 10^{-3}T)$	(21; 50; 35)
Ge	$0.587 - 0.105 \times 10^{-3}(T - 1211.5)$	(26)

Table 4.2. Molar Volume (m^3/mol) of Elemental Liquid

		Ref.
Au	$11.3 \times 10^{-6}(1.0 + 0.000069 \times (T - 1336.15))$	(27)
	$1.1345 \times 10^{-5} \exp [8.0 \times 10^{-5}(T - 1337)]$	(26)
	$1.02582 \times 10^{-5} + 7.797 \times 10^{-10}T$	(48)
Sn	$0.118710/7300$	(38)
Ge	1.2966×10^{-5}	(26)

Table 4.3. $\{L_1, L_2, L_3, L_4\}$, Interaction Parameters

System		Ref.
[Au,Ge]	$\{-20050 - 8.365 \times T, -12950 - 2.015 \times T, -13.52 \times T, 0\}$	(26)
[Sn,Ge]	$\{2738.48 - 8.365 \times T, -472.41, 0, 0\}$	(17)

In the following paragraphs, the calculation of the surface tension of the binary liquids will be discussed step-by-step. Initially, we plot the excess free energies of both the AuGe and SnGe systems as a function of Ge content using the interaction parameters tabulated in 4.3 using Eq. 4.10. The following data is used for means of an example:

$$\sigma^{Sn} = (0.5828 - 0.0834 \times 10^{-3}T) \quad (4.11)$$

$$\sigma^{Au} = 1.169 - 0.25 \times 10^{-3}(T - 1336.15) \quad (4.12)$$

$$\sigma^{Ge} = 0.587 - 1.05 \times 10^{-4}(T - 1211.5) \quad (4.13)$$

$$Vol^{Sn} = 0.118710/7300 + 0T \quad (4.14)$$

$$Vol^{Au} = 11.3 \times 10^{-6}(1.0 + 0.69 \times 10^{-4}(T - 1336.15)) \quad (4.15)$$

$$Vol^{Ge} = 1.2966 \times 10^{-5} \quad (4.16)$$

Figure 4.1 plots $G^{Ex,L}$ for AuGe and SnGe at $T = 1500K$ in blue and red, respectively. The dotted line represents the simplest solution model, in that all interaction parameters are identically set equal to 0, assuming zero energy of mixing. The partial molar Gibbs' free energies (Equations 4.7 and 4.8) are plotted in Figure 4.2. Again, blue represents the AuGe system, while red represents the SnGe system.

The partial molar Gibbs free energies of components A and B in the bulk are given by Eqs. 4.7 and 4.8 and are plotted in Figure 4.2. The blue line represents the AuGe-system, while red represents the SnGe-system. In each system, $\overline{G}_A^{Ex,b}(T, x_B^b)$ is plotted with a solid line and $\overline{G}_B^{Ex,b}(T, x_B^b)$ is represented by the dashed line. For clarity, the ideal solution is not shown, but uniformly equal to 0.

AuGe–system and SnGe–system

T = 1500 K

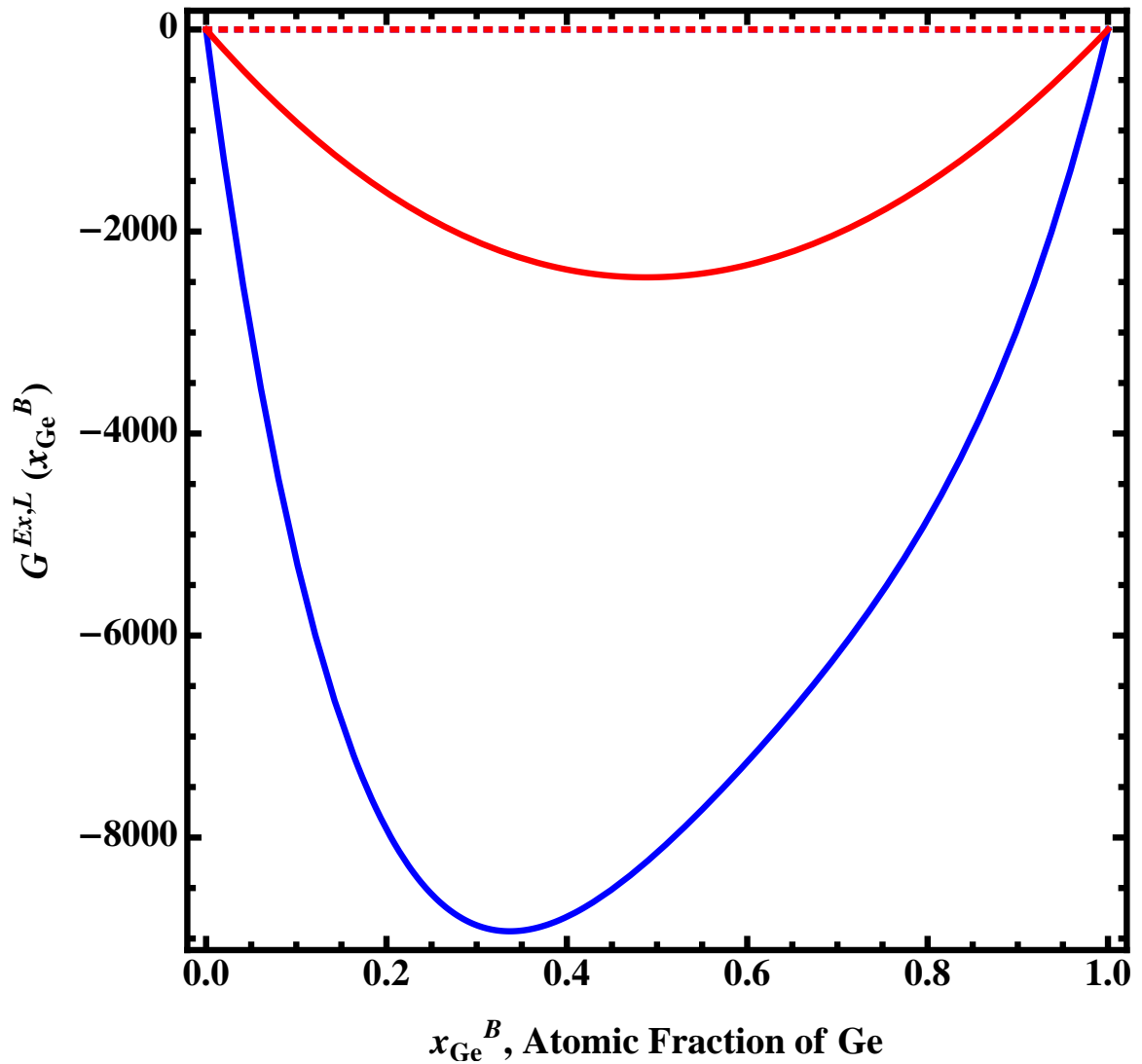


Figure 4.1. The excess free energy of mixing of a AuGe (blue) and SnGe (red) alloy at $T = 1500K$ is shown. The solid lines are calculated according to the Redlich-Kister expansion using published interaction parameters for each system. The dashed lines (the blue line is not visible under the red dashed line) assume no excess energy of mixing, i.e. the interaction parameters in the Redlich-Kister expansion are identically set equal to 0.

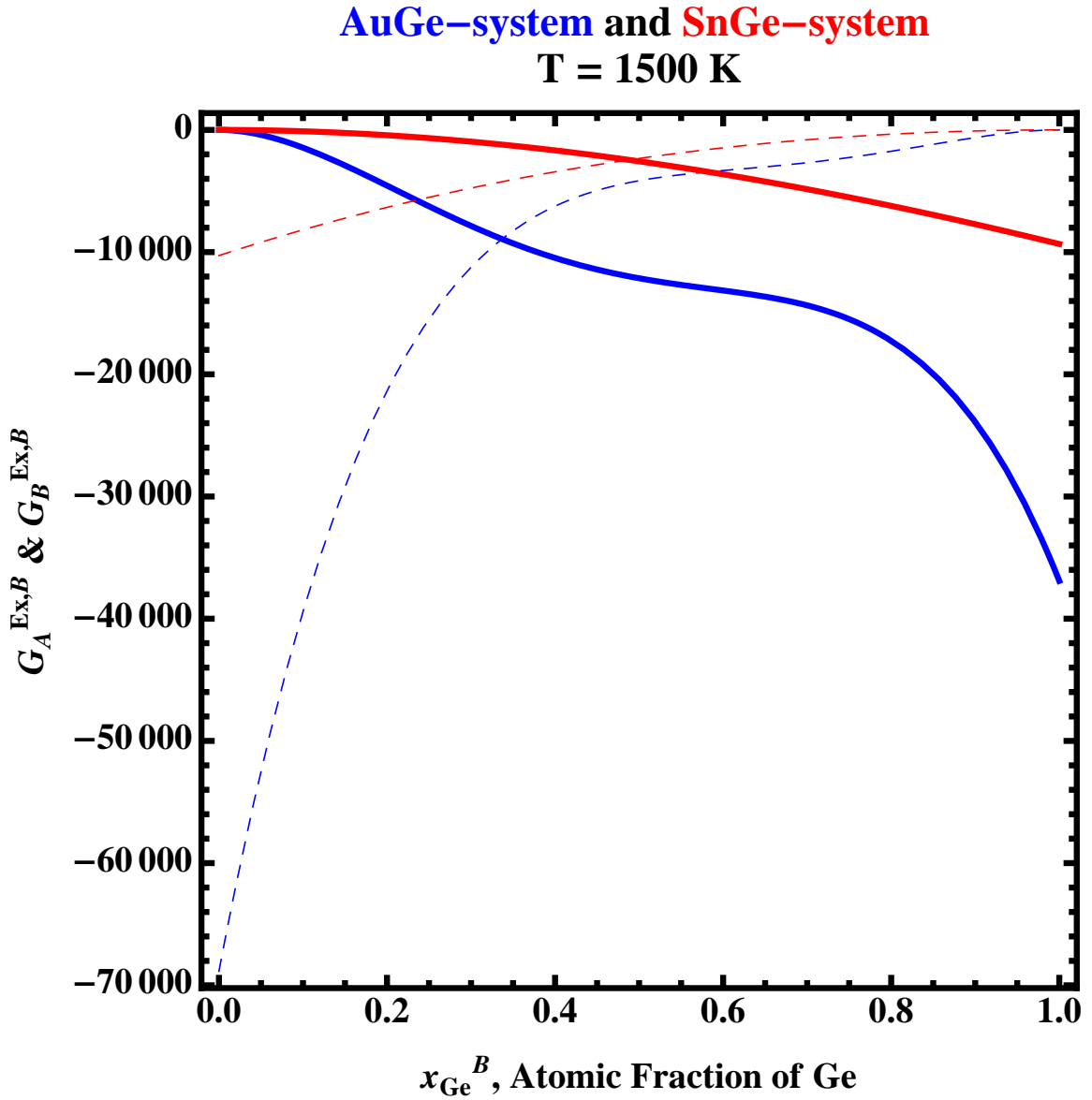


Figure 4.2. The partial molar Gibbs free energies of components A and B in the bulk are plotted as a function of x_{Ge}^B . Blue represents the AuGe-system, while red represents the SnGe-system. $\overline{G}_A^{Ex,b}(T, x_B^b)$ is plotted as a thick, solid line and $\overline{G}_B^{Ex,b}(T, x_B^b)$ is plotted as a dashed line.

Subsequently, we solve for the surface composition of the binary alloy liquid as a function of the overall composition of the binary alloy. This is done by setting Eq. 4.2 equal to Eq. 4.3 and solving for x_B^s with $x_A^s = 1 - x_B^s$. Figure 4.3 shows the expected composition of the surface layer, x_B^s , as a function of the composition of the bulk liquid, x_B^b , shown for both the AuGe (blue) and SnGe (red)-systems calculated at $T = 1500K$. The black dotted line is added to guide the eye and represents a surface layer of composition equal to that of the bulk. Clearly, both systems are predicted to consist of surface layers deviating in composition from the bulk. However, the two systems also display a marked difference in behavior. While the surface of the SnGe-systems is predicted to be slightly deficient in Ge, a significant increase in Ge-content relative to the AuGe-bulk system is predicted. This indicates that Sn is slightly more surface active than Ge, but that Ge is far more surface active than Au at this temperature. Once the surface composition is predicted, σ_L can be calculated using either Eq. 4.2 or 4.3. This calculation is carried out at $T = 1500K$ and plotted in Figure 4.4. The SnGe system (red line in Figure 4.4) shows a positive deviation from the concentration weighted average (black, dashed line) of the liquid surface tensions of the two elements. In contrast, the AuGe system (blue line) deviates negatively and far more pronounced from the surface tensions predicted by the concentration weighted average.

Using the above described analysis, the temperature and composition dependent surface tensions of both the AuGe and SnGe-systems can be calculated. Figure 4.5 shows the calculated surface tensions of $\text{Sn}_{1-x}\text{Ge}_x$ liquids at $T = 573, 773, 973, 1173, 1373,$ and $1573K$. At low temperatures, the surface tension of the pure *Sn*-liquid takes on a higher value than that of the pure *Ge*-liquid. The surface tension of the SnGe-alloys then show a negative deviation from the concentration weighted average. In contrast, at higher temperatures, the surface tension of pure *Sn*-liquid is lower than that of the pure *Ge*-liquid, indicating that *Sn*-liquids display a stronger temperature dependence. Also, at lower temperatures, the alloys liquids deviate positively from the values predicted by the concentration weighted average. This indicates that Ge has a lower surface activity at higher temperatures than at lower temperatures.

Similarly, the composition dependent surface tensions of the $\text{Au}_{1-x}\text{Ge}_x$ -liquids is calculated for temperatures ranging between 973 and 1973K. Unlike in the SnGe system, the surface tensions of the alloys deviate negatively from the values predicted by the concentration weighted average at all temperatures under investigation. However, overall, the expected temperature trend is observed: as the temperature is increased, the surface tensions decrease.⁽⁴⁷⁾ This trends arises from the fact that the surface tension in its' simplest form is proportional to N and $\Delta\epsilon$, where N is the number of atoms per unit area and $\Delta\epsilon$ is the energy required to overcome a nearest neighbor interaction/bond strength. In general, as the temperature increases the density decreases, i.e. N decreases. Also, considering a simple Lennard-Jones potential, we know that as the temperature increases, the energy to overcome a nearest neighbor bond decreases. Therefore, it follows that as the temperature increases, the surface tension must decrease. Now that the surface tensions have been calculated, we focus our attention of the calculation of the size dependent phase diagrams.

AuGe–system and SnGe–system
T = 1500 K

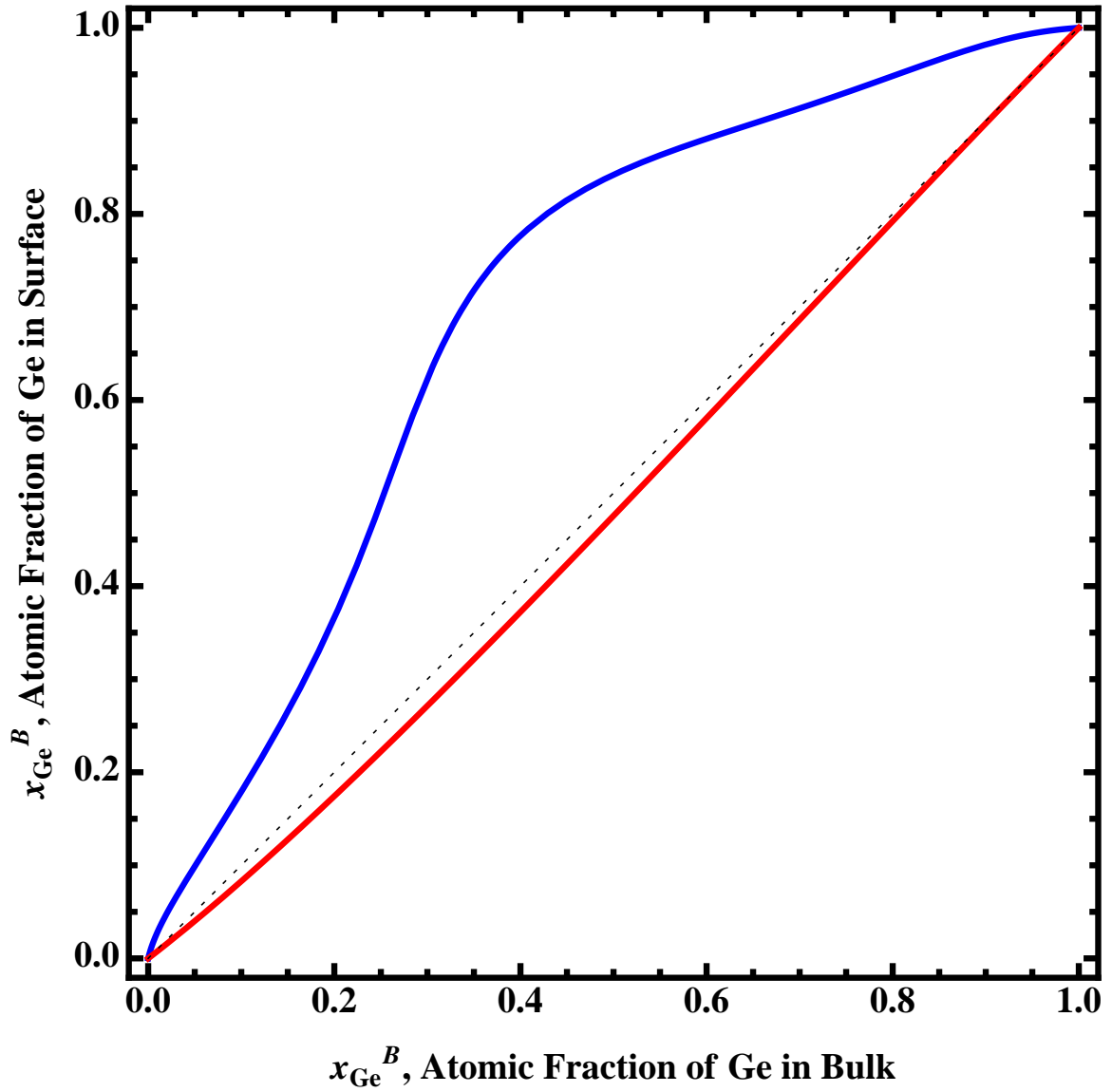


Figure 4.3. The concentration of Ge in the surface of a liquid alloy is calculated as a function of Ge concentration in the bulk liquid. As before, blue represents the AuGe system and red represents the SnGe system.

AuGe–system and SnGe–system

T = 1500 K

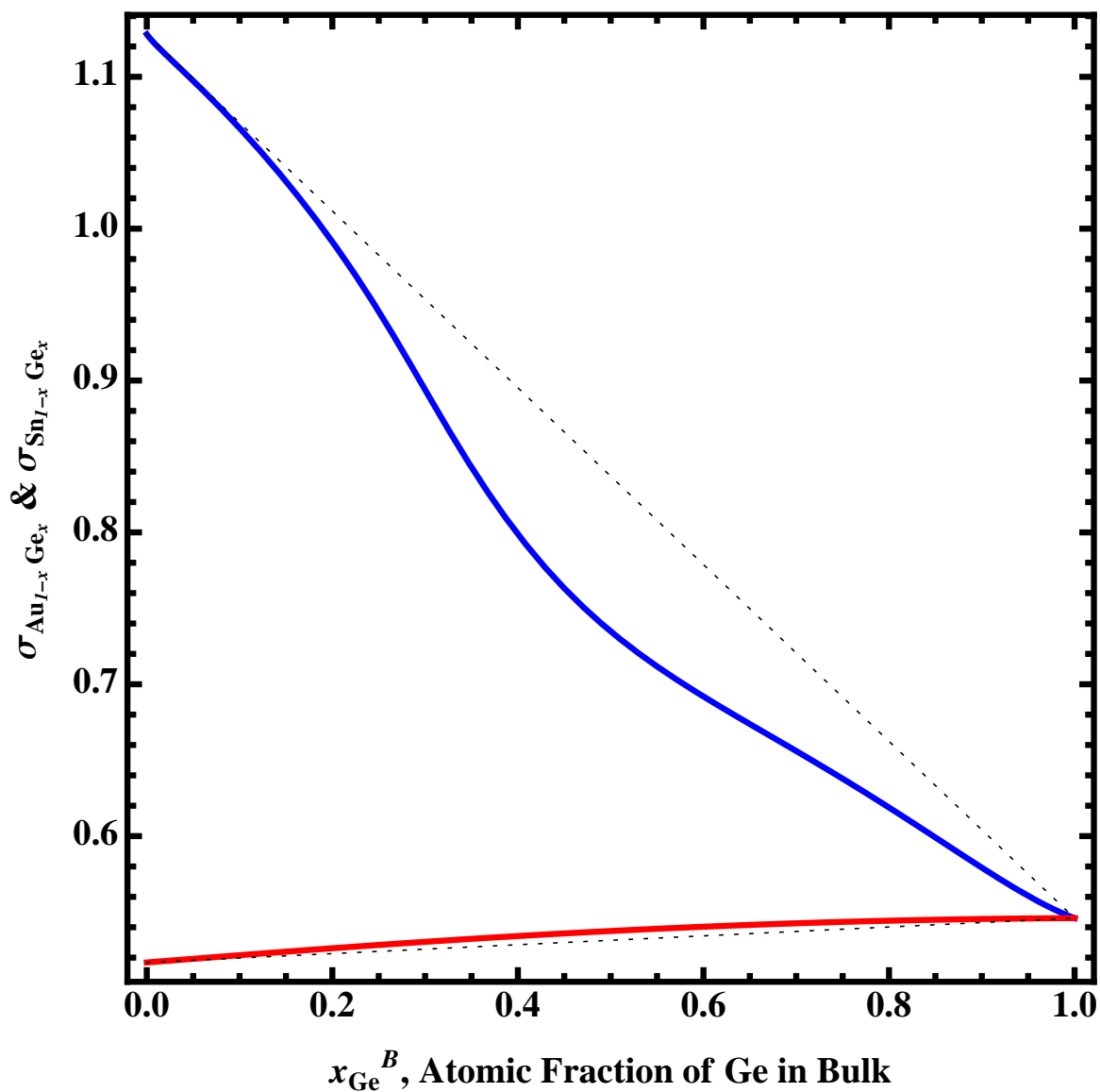


Figure 4.4. The composition dependent surface tensions of the $\text{Au}_{1-x}\text{Ge}_x$ and $\text{Sn}_{1-x}\text{Ge}_x$ liquids are plotted in blue and red, respectively. The black dotted line represents the concentration weight average of the liquid elements at $T = 1500$. In both systems, a deviation from the concentration weighted average is predicted.

Sn_{1-x}Ge_x system
T = 573, 773, 973,
1173, 1373, 1573

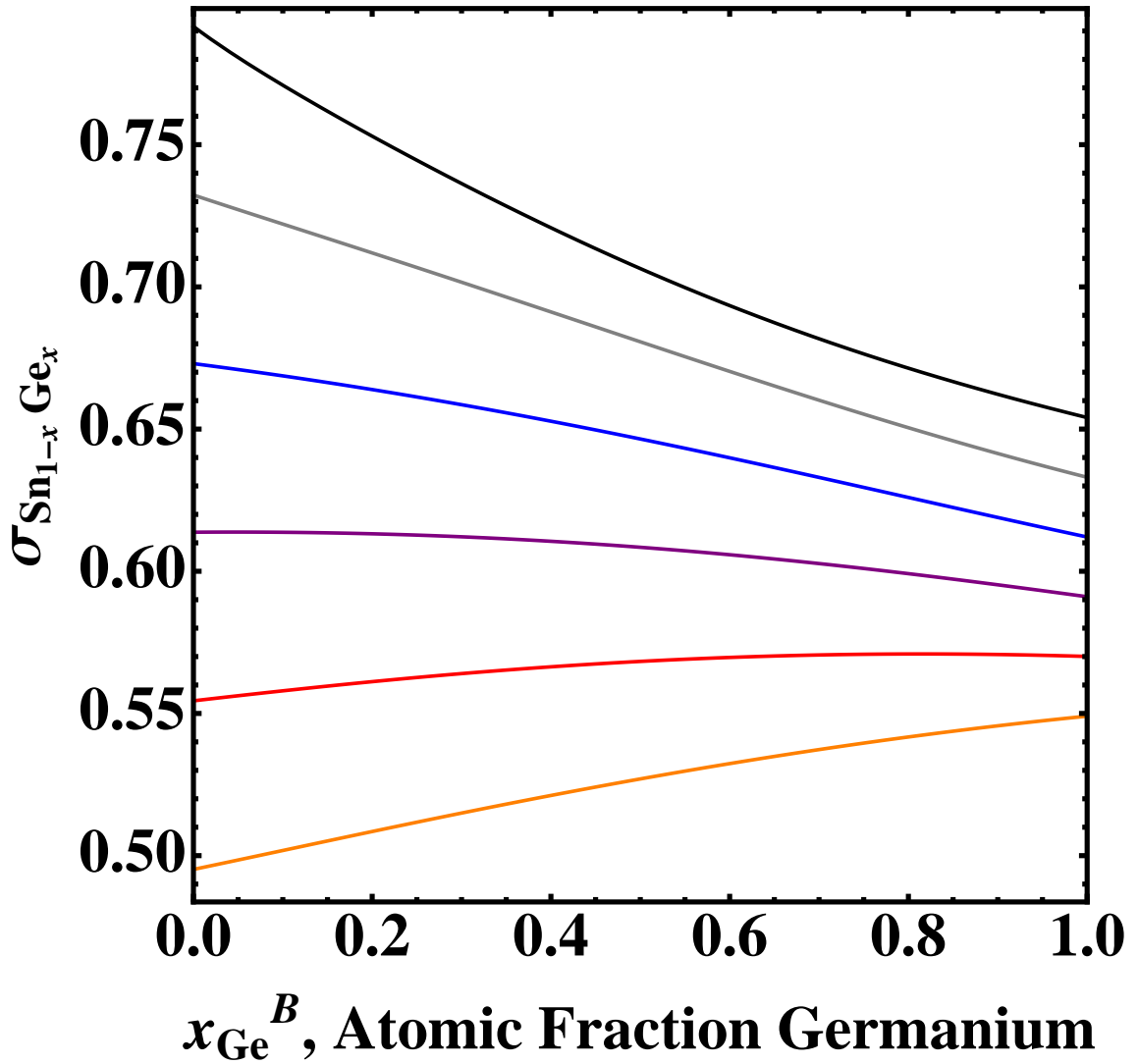


Figure 4.5. The composition dependent surface tensions of Sn_{1-x}Ge_x liquids are calculated at various temperatures: $T = 573, 773, 973, 1173, 1373,$ and 1573K .

Au_{1-x}Ge_x system
T = 973, 1173, 1373,
1573, 1773, 1973

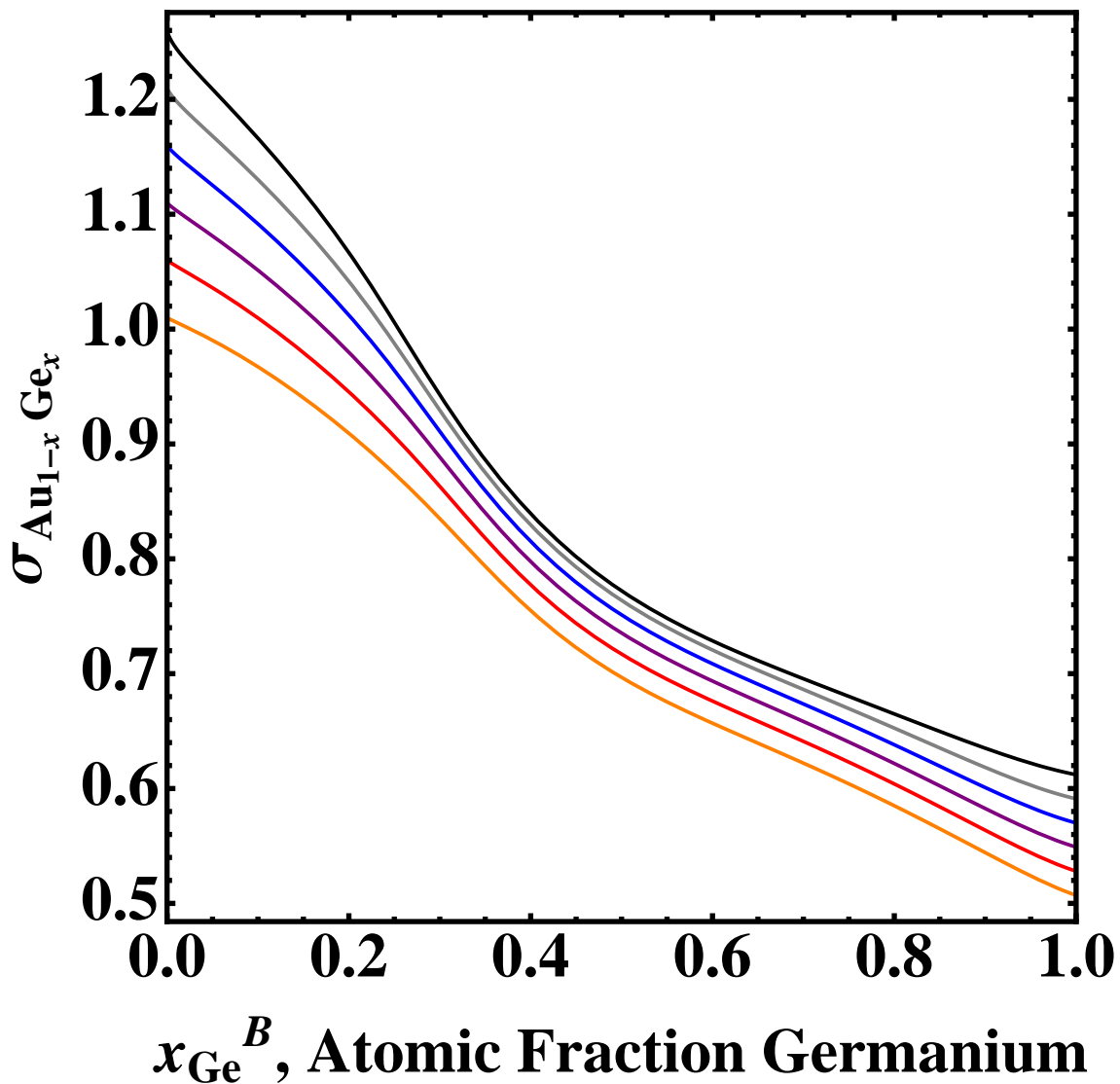


Figure 4.6. The composition dependent surface tensions of the Au_{1-x}Ge_x liquids are plotted at $T = 973, 1173, 1373, 1573, 1773, \text{ and } 1973\text{K}$.

Chapter 5

Nanoscale Phase Diagrams

The melting point of an elemental substance, such as a metal or semiconductor material, can be described as the temperature at which the substance undergoes a change of state from solid to liquid. Similarly, the opposing change of state from liquid to solid is described as freezing or solidification and, in general, melting and solidification occur at the same temperature. More specifically, the melting point of a substance occurs when the liquid and solid phase exist in equilibrium, indicating that the total free energy of the liquid phase is equal to the total free energy of the solid phase at the equilibrium melting temperature.

The total free energy of a system can be calculated by considering two separate contributions: the first from the volumes of the various phases and the second from the surfaces and interfaces existing in the system. The volumetric contribution is determined using the volumetric Gibbs' free energy, G^{phase} (J/m^3), and the contribution of the surface to the overall free energy is determined by the surface energy. These parameters can be summarized in the following equation:

$$G^{Tot,phase} = V^{phase} \cdot G^{phase} + A^{phase} \cdot \sigma^{phase}, \quad (5.1)$$

where V (m^3) and A (m^2) represent the volume and surface area of the phase, respectively, and σ (J/m^2) is the surface energy of the phase.

In a macroscopic system, the volumetric contribution far exceeds the contribution of the surface to the total energy. This is easily evident when considering a spherical system, as the volume is proportional to r^3 , while the surface is proportional to only r^2 . Therefore, the contribution of the surface can and is often neglected. The total free energy is then estimated by:

$$G^{Tot,phase} \approx V^{phase} \cdot G^{phase}. \quad (5.2)$$

An example of the temperature dependence of the Gibbs' free energy of an elemental solid and liquid is shown schematically in Figure 5.1. Here, blue and red represent

Macroscopic Unary System

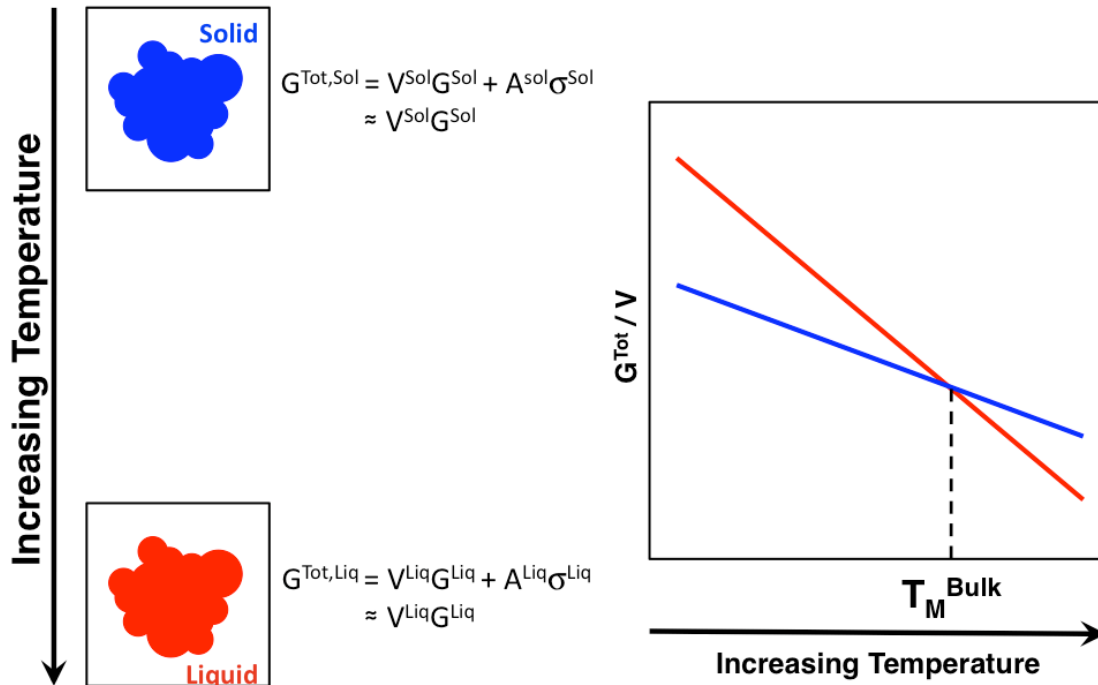


Figure 5.1. Schematic representation of the temperature dependent total Gibbs' free energy of a solid and a liquid system, shown in blue and red, respectively. The temperature at which the energy of the phases is equal represents the bulk melting point of the system.

the solid and liquid phases, respectively. Generally, both the free energy of the solid and corresponding liquid show a negative temperature dependence with the liquid phase displaying a stronger temperature dependence. Clearly, the Gibbs free energies cross at T_M^{Bulk} , which represents the bulk melting temperature. At temperatures below T_M^{Bulk} , the free energy of the solid phase minimizes the total free energy of the system, and thus the solid phase is expected. At T_M^{Bulk} , the two phases may coexist in equilibrium. Then, as the temperature is increased further, the free energy of the liquid phase becomes lower than that of the solid phase and melting is expected to occur. Naturally, at some further elevated temperature, the vapor phase would become the most favorable temperature, which accordingly is known as the boiling point. However, in the case of metals and semiconductors, this temperature is usually very high and will not be considered.

Next, consider a system similar to that described above, but much smaller in size. As has been discussed in the preceding chapters, as the system size decreases, the contributions of the surfaces become increasingly important. Eventually, the surface

contribution may no longer be neglected and the total free energy of the system under investigation must be written as shown in Equation 5.1. It should further be noted that the surface energy, σ , can only assume positive values. Therefore, this contribution will always work to increase the overall energy of the system. Accordingly, one must also consider what system geometry would minimize the total surface contribution to the free energy. This shape is known to be a sphere, which has the smallest surface to volume ratio and by neglecting any surface energy anisotropy, this will be the shape under consideration in the following.

The total free energy can then be calculated per unit volume. Considering a spherical particle, Equation 5.1 becomes:

$$\begin{aligned}
 G^{Tot,phase}/V^{phase} &= G^{phase} + A^{phase}/V^{phase} \cdot \sigma^{phase} \\
 &= G^{phase} + (4\pi r^2)/(4/3\pi r^3) \cdot \sigma^{phase} \\
 &= G^{phase} + 3/r \cdot \sigma^{phase}.
 \end{aligned}
 \tag{5.3}$$

where r is the radius of the spherical particle. Clearly, at large values of r , the surface contribution becomes negligible. However, as r decreases sufficiently, this contribution may no longer be neglected. With further decreasing radius, the surface contribution increases accordingly, which is shown schematically in Figure 5.2. Clearly, the addition of the surface area term leads to an upward shift of the free energy. It is also generally true that the surface energy of the solid phase is larger than that of the liquid phase.(47; 61; 73; 3; 41; 33; 32) Therefore, when considering a particle of radius r , the shift of the free energy in the solid phase will be larger in magnitude than that in the liquid phase. This leads to a decrease in the melting point, T_M^{Nano} , proportional to the inverse of particle size, as evidenced experimentally by many researchers.(7; 13; 12; 30; 10; 46; 51; 52)

However, when studying melting/solidification, one must also investigate the transition between the two phases. Consider, for example, a solid particle of radius r at the onset of melting. This leads to a particle with a majority solid-phase and a small fraction liquid-phase. As has been discussed in the preceding chapters, possible morphologies that must be considered are: solid-core/liquid-shell, liquid-core/solid-shell, phase separated, and the bilobe structure. This leads to a possible change in the total free energy of the particle as the fraction of liquid increases, which is shown schematically in Figure 5.3. Regardless of the morphology, phase transitions can lead to a kinetic barrier of melting/solidification, a behavior that was demonstrated and explained by (70) in the case of Germanium embedded in silica. Ge nanoparticles displayed both superheating and supercooling centered approximately about the bulk melting temperature. This phenomenon was attributed to the kinetic barrier associated with the melting/solidification transition. Thus, it is important to consider not only the total free energy of the solid and liquid phases, but also the transition between the two phases.

The melting of elemental solids has been extensively studied, but as was shown in the previous chapters, binary alloys show interesting structures when reduced in size to the nanoscale. Recently, the effect of size on the phase diagrams of binary

Nanoscale Unary System

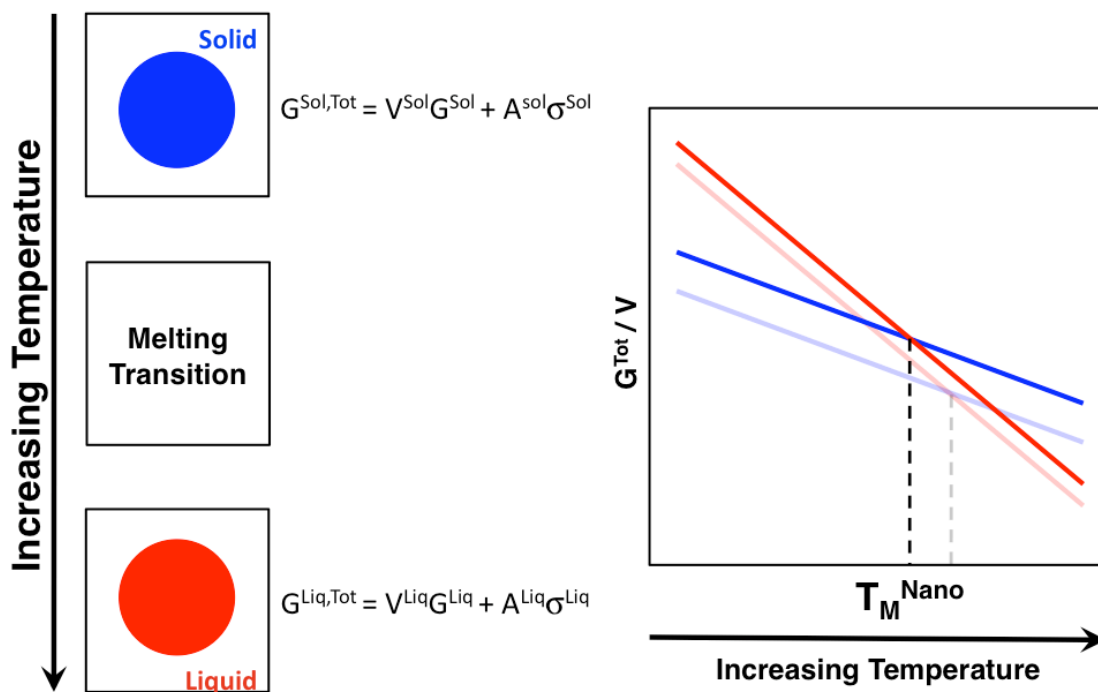


Figure 5.2. The temperature dependent total free energy per volume of particle of a representative solid and a liquid particle is shown in blue and red, respectively. The addition of the surface term shifts the free energy upward for both the liquid and the solid phase. Generally, however, the shift of the solid phase is more pronounced, thus decreasing the melting temperature.

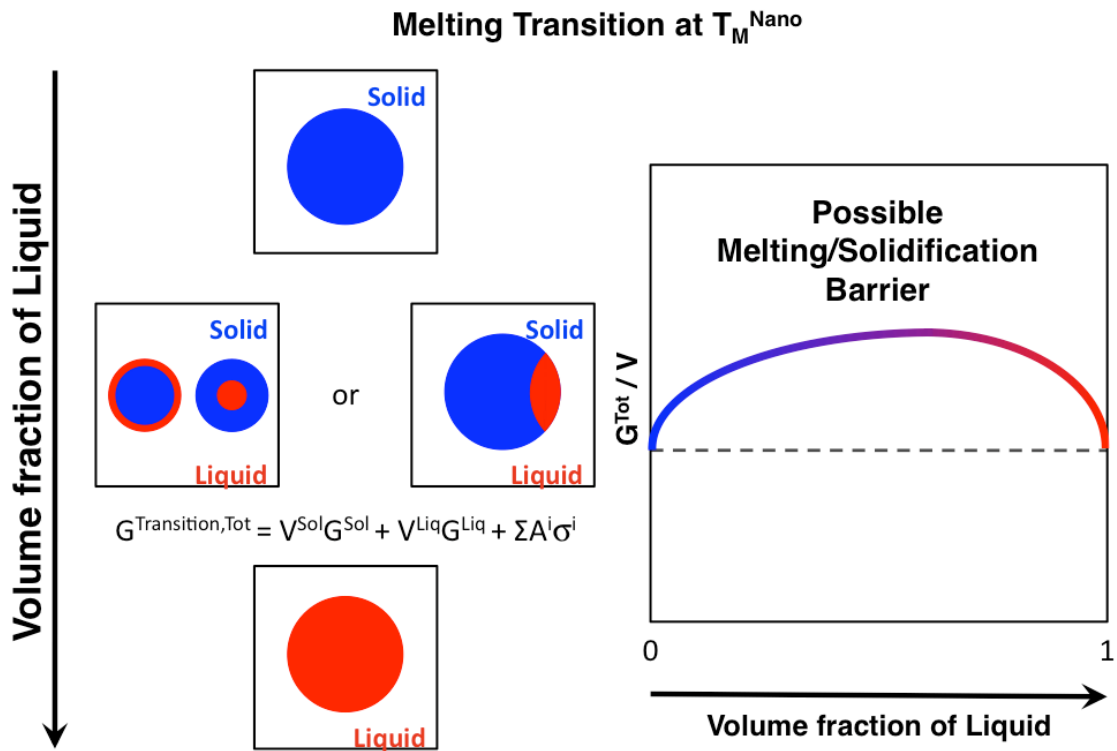


Figure 5.3. The free energy of a particle as it undergoes melting. As the volume fraction of the liquid within the particle is increased, the energy of the particle undergoes a maximum value, that can be seen as a kinetic barrier for melting. This leads to the possibility of superheating and supercooling in nanoparticles due to the addition of the surface/interface energy terms.

alloys has been studied quite frequently.(26; 48; 15; 16; 36; 63; 28; 45; 25; 56) While these studies take into account the addition of the surface term to the liquid and solid phases, the tangent rule construction, generally applied to bulk phases, is employed to determine the phase boundaries. The use and applicability of the tangent rule construction will be more closely examined in the following paragraphs.

Initially, we will consider a macroscopic system consisting of elements A and B . An arbitrary binary alloy may then be described by its overall composition, $A_{1-x}B_x$ (this is shown in Figure 5.4 as composition x_c). Subsequently, at each temperature, the Gibbs' free energy of all phases must be calculated as a function of composition, x_c . This is shown graphically in Figure 5.4, where 3 distinct phases are under consideration. The phases considered are solid-phases A (blue) and B (red), and the liquid phase L (purple). In general, the total energy of the alloy must be minimized to reach equilibrium, which can be achieved by use of the tangent rule construction, while ensuring conservation of mass. Consider an alloy of composition x_c at some low temperature as shown in the left graphic of Figure 5.4. The tangent to both phases A and B is shown as a black dashed line. Clearly, the alloy can minimize its energy by splitting into some solid-phase A and solid-phase B rather than existing in the liquid phase with composition x_c . Furthermore, the diagram indicates that the two solid phases are not composed of pure elements, but rather each display some low solubility of the second element.

As the temperature increases to some intermediate temperature, as shown in the center panel, the free energy of all phases decrease. However, the free energy of the liquid phase decreases more rapidly than that of the solid phase. Once again, the tangent minimizing the free energy is shown as a black, dashed line. Unlike at the lower temperature, it is now energetically favorable for the alloy to be composed of some solid-phase A and a liquid phase AB . In both cases, the Lever rule can be used to determine the fractional amount of each phase in the system.(5) Finally, as the temperature increases, the free energy of the liquid phase decreases sufficiently to make it the most energetically favorable phase and the system melts completely (right panel) to form a liquid of composition, x_c . This procedure leads to a bulk equilibrium phase diagram such as the one shown in Figure 1.1.

Now, consider a system containing a binary alloy nanoparticle. When studying the melting behavior of these alloys, we must first consider each phase separately. As in the case of the unary nanoscale system, surface contributions now may not be neglected, leading to an overall increase in the free energies of the individual phases (recall, surface energies are positive and thus lead to an increase in energy). The amount of increase then is dependent on the phase under consideration and will not be equal in all phases. Thus, if the previously described tangent rule construction is used, a shift in transition temperatures and solubility limits is expected. Similar procedures are employed by (64; 26) and other researchers. Their findings show the expected melting point depressions of the elemental solids, a decrease in eutectic temperature, a shift in eutectic composition, as well as changes in the solubility limits.

However, these works use the tangent rule construction, neglecting the contribu-

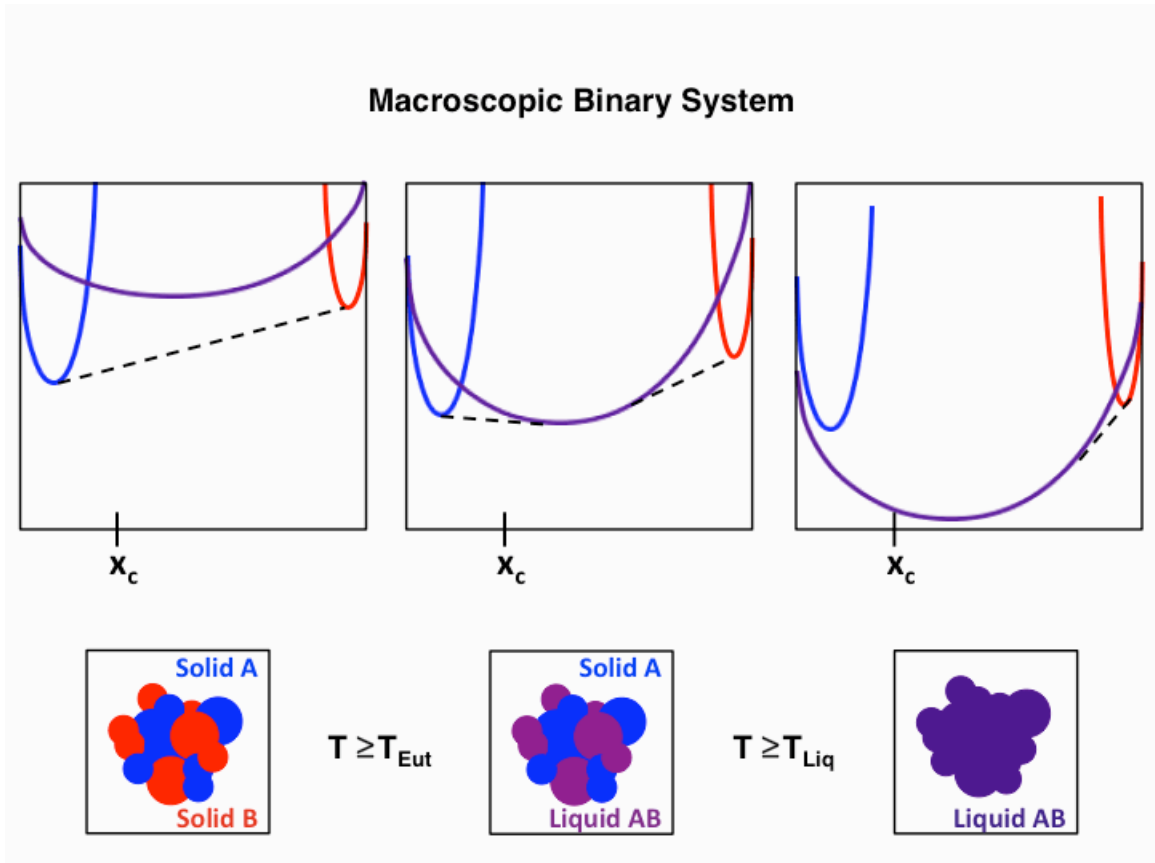


Figure 5.4. Gibbs' free energy of two solid phases, A (blue) and B (red), and a homogeneous liquid phase (purple) at three temperatures are considered. In macroscopic alloys, the tangent rule construction (black, dashed line) is used to determine the compositions that lead to the solidus and liquidus lines of phase diagrams. In the left most panel, an alloy composed of two solid phases, A and B , minimizes the overall energy of the system. Above the eutectic temperature, a solid A -liquid AB structure minimizes the energy. Above the liquidus temperature for the composition under consideration, the homogeneous liquid phase is stable.

tion of the interface energy between the two coexisting phases. Consider, for example, the binary alloy in the left most panel of Figure 5.5. The light grey, dashed line represents the tangent to the two solid phases. Clearly, this indicates that the alloy must split into a particle containing solid A and solid B , with the fractional amounts of each phase depending on the Lever rule. As the composition x_c changes, the free energy of the alloy particle is predicted to increase along the tangent line, while the volume fraction of the two phases changes. However, as was demonstrated before in the unary system, a nanoparticle consisting of solid and liquid phases does not follow a linear relationship in fractional amount of the secondary phase, leading to a kinetic barrier of melting in elemental systems. In a binary alloy system, various phases may also coexist and the interface energy between them may no longer be neglected. The total free energy of a particle of volume V consisting of two phases can then be calculated by:

$$\begin{aligned} G^{Tot} &= f_\alpha \cdot V \cdot G^\alpha + f_\beta \cdot V \cdot G^\beta + A^\alpha \cdot \sigma^A + A^\beta \cdot \sigma^B + A^{\alpha/\beta} \cdot \sigma^{\alpha/\beta} \\ &= (1 - f_\beta) \cdot V \cdot G^\alpha + f_\beta \cdot V \cdot G^\beta + A^\alpha \cdot \sigma^A + A^\beta \cdot \sigma^B + A^{\alpha/\beta} \cdot \sigma^{\alpha/\beta}, \end{aligned} \quad (5.4)$$

where f_α and f_β represent the volume fractions of phase α and β , respectively and $f_\alpha + f_\beta = 1$. A^α , A^β and $A^{\alpha/\beta}$ represent the surface and interface areas of the various phases, while σ^α , σ^β and $\sigma^{\alpha/\beta}$ represent the corresponding surface and interface energies. If it is assumed that the particle is confined to a spherical geometry, $A^\alpha + A^\beta$ must equal $4\pi r^2$. However, if the previously described bilobe geometry is assumed, the total volume of the particle will be held constant: $V^\alpha + V^\beta = 4/3\pi r^3$. Now, the addition of surface area terms in Equation 5.4 leads to a positive deviation (black dashed line) of free energy from that of the tangent line (grey, dashed line) shown in Figure 5.5. Depending on the degree of positive deviation, the addition of this energy term can cause the free energy to shift above the free energies of other phases, such as the liquid phase in the center panel of Figure 5.5. This would indicate that the system can decrease its free energy by existing in a purely liquid state, rather than a bilobe of some solid and some liquid. These findings clearly reinforce the need to investigate the nanoscale phase diagram more closely and to take into account the contribution of the interface energy to the total free energy.

The theoretical approach is based on a procedure outlined by Weissmueller (68; 69; 8) *et al.*, whose work focuses on idealized binary systems. The systems they consider consist of components A and B (with equal melting temperatures) with a eutectic composition lying at 50 at. % B. Additionally, the investigated system is assumed to have no solid solubility and an ideal solution as the melt, thus leading to a bulk phase diagram that is symmetric about the 50/50 at. % composition. Furthermore, the alloy nanoparticle is assumed to be confined to a spherical cavity of radius r with all interface energies set equal to one another. As a result, all internal dihedral angles are equal to 90° for all volume fractions of β -phase. Moreover, the molar volumes of all phases are assumed equal to one another. The free energy is then calculated as follows:

$$G_{tot} = \frac{4}{3}\pi r^3 \cdot G_{vol} + \sum_{i=1} \gamma^i \cdot A^i. \quad (5.5)$$

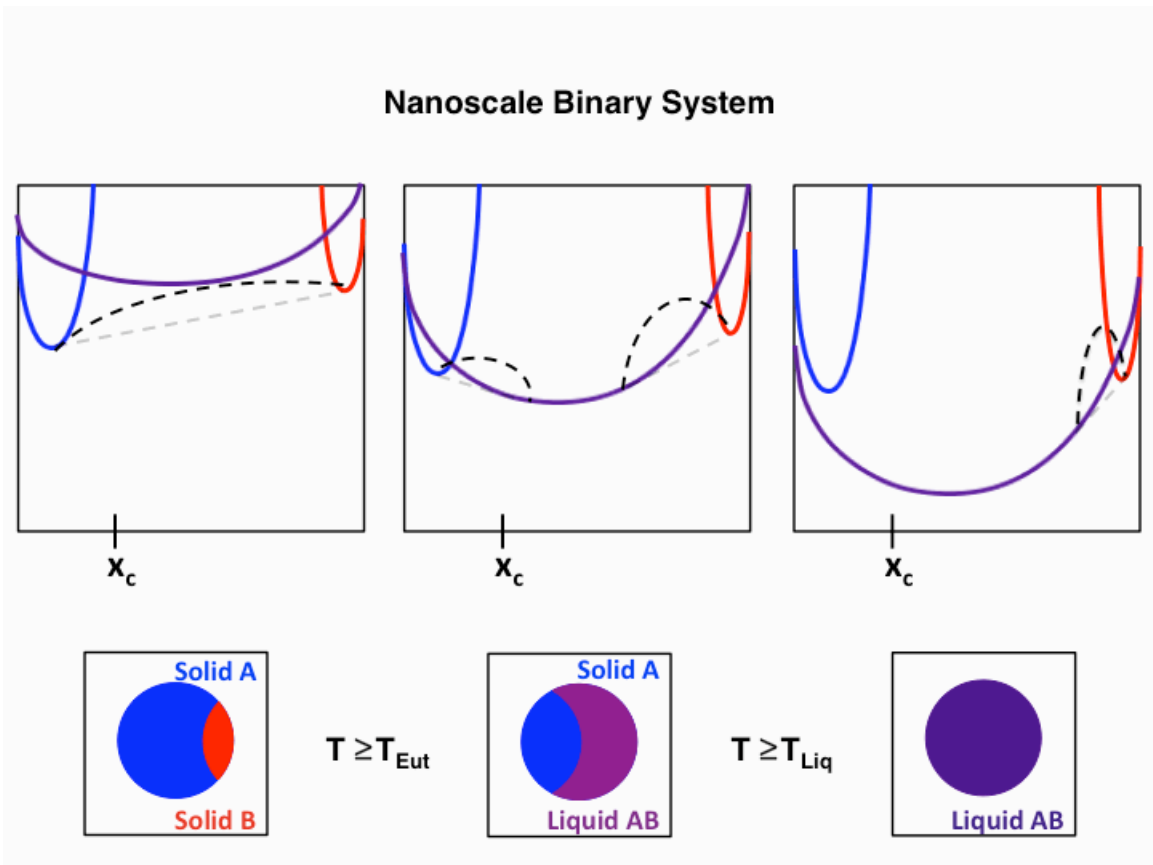


Figure 5.5. A nanoscale system composed of the same phases as in Figure 5.4 is depicted. Unlike before, surface effects must be considered. This leads to a shift in the overall free energies of all phases (recall surface energies are positive). Additionally, the tangent rule construction may no longer be applied and the free energy curve must be calculated exactly. This leads to a positive deviation from the tangent rule construction.

The summation in the second term can be reduced to a single additive term due to the assumption that all interface energies are equal (the surface contribution of the sphere is therefore equal for all compositions and phases). Thus,

$$G_{tot} = \frac{4}{3}\pi r^3 \cdot G_{vol} + \gamma^{int} \cdot A^{int}. \quad (5.6)$$

A_{int} was then approximated using an analytic function. The free energy of the system can subsequently be calculated as a function of size. At each temperature, four free energies are calculated as a function of volume fraction of the secondary-phase: $G^{S_1S_2}$, G^L , G^{S_1L} and G^{S_2L} , where S and L represent the solid and liquid phases, respectively. The molar free energies are calculated as follows in units of the enthalpy of fusion, which is assumed equal in all phases.

$$g^L = 1 + \frac{T}{T_f} \left(-1 + \frac{R}{\Delta s_f} [x \cdot \ln(x) + (1-x) \cdot \ln(1-x)] \right)$$

$$G^L(x, \tau) = N \cdot g^L \quad (5.7)$$

$$G^{S_1S_2} = (1 - f_2) \cdot G^{S_1} + f_2 \cdot G^{S_2} + \gamma \cdot A(f_2, N) \quad (5.8)$$

$$G^{S_1L}(x, \tau) = (1 - f_L) \cdot G_1^S + f_L \cdot G^L + \gamma \cdot A(f_L) \quad (5.9)$$

Here, x is the composition in at. % B. f_2 and f_L represent the volume fraction of solid 2 and the liquid phase, respectively. $\frac{\Delta s_f}{R}$ is set equal to 1.2, typical for metals. Δs_f and Δh_f are the entropy and enthalpy of fusion, respectively. T_f is the melting temperature. Then, for every value of $\tau = \frac{T}{T_f}$, the free energies are calculated as a function of composition and phase fraction. The free energies are then compared for each composition and the structure that minimizes the free energy is determined. These energies are then compared and the size dependent phase diagram may be constructed.

However, the above described simplifying assumptions are not applicable in real systems such as SnGe and AuGe. For one, the melting temperatures of the elemental solids are not equal and the eutectic compositions are generally not centered at 50 at. % B. Besides some solid solubility contribution typically observed at temperatures above absolute zero, the volumes of elemental solids change upon melting, thus the assumption of equal molar volumes in all phases fails. Au and Sn experience a volume expansion upon melting, whereas Ge contracts, leading to a difference in particle size upon melting when the chemical content of the particles remains fixed. Additionally, if the molar volumes of two pure components are different (whether in the solid or the liquid phase), it is fairly obvious that the molar volumes of phases consisting of mixed components must also vary. Furthermore, it is shown above that the equilibrium structure of a binary alloy depends only on γ_1 and γ_2 . Weissmueller *et al.* do not account for the possibility of energy minimization by formation of a core-shell

or phase-separated structure; however, this oversight is not detrimental to the conclusions, because of the assumptions made by the authors. One of the simplifying assumptions made was the equality of all interface energies which necessarily leads to $\{\gamma_1, \gamma_2\} = \{1, 1\}$, (located in the region of bi-lobe phase stability in Figure 2.1). However, the interface/surface energies may not be assumed equal to one another. As discussed previously, composition and temperature ranges may exist in which the core-shell or phase separated structure is the stable structure. Also, predictions and experimental observations indicate that the equilibrium structures of both AuGe and SnGe BEANs are not confined to a spherical external surface, but rather form cusped bi-lobes.

In the following paragraphs, the size dependent nanoscale phase diagrams for the AuGe and SnGe systems will be calculated using the above described theoretical approach. Herein, available experimental and theoretical data for surface and interface energies, and free energies will be used to first calculate the phase diagram of free-standing particles. Finally, an attempt will be made to extend the theory to available data for embedded nanoparticles. By necessity, some simplifying assumptions will be made. First, we will assume negligible solid solubility, which is in large part due to the fact that surface and interface energies are available only for the pure solid phase. Also, in the systems under investigation, AuGe and SnGe, the macroscopic solid solubility is relatively low. Furthermore, we choose to investigate only the solid phases found in the bulk phase diagram. Namely, Ge in the diamond-phase, Au in the face-centered cubic (FCC)-phase, and Sn in the body-centered tetragonal (BCT)-phase, minimizing the number of phases under investigation.

5.1 Free energy curve of a Solid-Solid particle

In subsequent sections, a nanosized system of radius r will be considered such that the volume of all possible morphologies and phases will be equal to $4/3\pi r^3$. Calculations demonstrating the theory will be performed at $r = 25 \times 10^{-9}$ m. In the following, we will consider the AuGe system, where x_{Ge} will represent the atomic fraction of Ge found in the system. The same analysis can be applied by substituting the values of Sn for the Au values.

Consider a particle that is composed of, for example, $x_{Ge} = 0.4$. How much of the volume of the particle will be consumed by the *Ge*-solid? Due to the differences in molar volume of the two elements, the particle will not be 40 volume % *Ge*-phase. A concentration weighted average of the two molar volumes will be used.(62) If the two elements are Au and Ge, the volume fraction of *Ge*-solid in the particle will be closer to 47% (at a representative temperature of 900 K), which can be calculated by:

$$f_{Ge(sol)}(T, x_{Ge}) = \frac{x_{Ge} \cdot v_{Sol}^{Ge}(T)}{x_{Ge} \cdot v_{Sol}^{Ge}(T) + (1 - x_{Ge}) \cdot v_{Sol}^{Au}(T)}, \quad (5.10)$$

where $f_{Ge(sol)}(T, x_{Ge})$ is the volume fraction of the *Ge*-solid. v represents the molar

volume and is dependent on temperature. Figure 5.6 shows the volume fraction of Ge-solid in a AuGe and a SnGe solid-solid particle at $T = 300 \text{ K}$ as a function of composition, x_{Ge} (blue line). The dashed, black line is added to guide the eye. The AuGe system displays a positive deviation from linearity due to the larger molar volume of Ge. In contrast, SnGe deviates negatively.

Next, we consider the free energy of a solid-solid particle, $G^{Au(sol)Ge(sol)}$. As discussed before, we must consider a volumetric and surface contribution (assuming isotropic interface energies):

$$\begin{aligned}
G^{Au(sol)Ge(sol)} &= V^{Au(sol)} \cdot G^{Au(sol)} + V^{Ge(sol)} \cdot G^{Ge(sol)} \\
&\quad + A^{Au(sol)} \cdot \sigma^{Au(sol)} + A^{Ge(sol)} \cdot \sigma^{Ge(sol)} + A^{Au(sol)Ge(sol)} \cdot \sigma^{Au(sol)Ge(sol)} \\
&= (1 - f_{Ge(sol)}(T, x_{Ge}))V \cdot G^{Au(sol)} + f_{Ge(sol)}(T, x_{Ge})V \cdot G^{Ge(sol)} \\
&\quad + A^{Au(sol)} \cdot \sigma^{Au(sol)} + A^{Ge(sol)} \cdot \sigma^{Ge(sol)} \\
&\quad + A^{Au(sol)Ge(sol)} \cdot \sigma^{Au(sol)Ge(sol)}.
\end{aligned} \tag{5.11}$$

As is seen in Table 5.1, the Gibbs' free energies are given in reference to the solid phase. Thus, the volumetric contribution of the solid phase is equal to 0. The surface contribution, however, must be calculated.

$$\begin{aligned}
G^{Au(sol)Ge(sol)}(x_{Ge}) &= A^{Au(sol)} \cdot \sigma^{Au(sol)} + A^{Ge(sol)} \cdot \sigma^{Ge(sol)} \\
&\quad + A^{Au(sol)Ge(sol)} \cdot \sigma^{Au(sol)Ge(sol)}.
\end{aligned} \tag{5.12}$$

As was discussed in preceding chapters, we must take into account all possible morphologies. The equilibrium morphology depends on the surface and interface energies. The surface energies are known as a function of temperature; however the interface energies between Ge-solid to Au-solid and Ge-solid to Sn-solid are unknown. Ge and Au and Ge and Sn are highly mismatched due to the large differences in lattice parameter. Consequently, it stands to reason that this interface energy is fairly high. For example, the interface energy of solid Au on solid sapphire is $2.18 \pm 0.06 \text{ J/m}^2$.(55) Therefore, we choose a value for the interface energy, which ensures the bilobe geometry as the energy minimization for all temperatures under investigation, with a chosen value of 2.6 J/m^2 .

At every temperature, the three applicable interface energies are used to determine γ_1 and γ_2 . These values can be used to calculate the energy contribution of the surfaces as a function of volume fraction. For the AuGe system at $T = 300 \text{ K}$, $\{\gamma_1, \gamma_2\} = \{0.699231, 0.320272\}$. Figure 5.7 shows results of the surface contribution of the possible morphologies. While the curves for the phase separated structure and the bilobe structure are very close, the bilobe structure minimizes the overall energy of the surfaces. A closer examination of the energy of solid-solid bilobe structure is depicted in Figure 5.8. This plot is calculated as a function of the molar concentration of Ge in the particle using Equation 5.10. Clearly, unlike the prediction from the tangent rule, the actual energy of a solid-solid particle can deviate from linearity. The energy deviates positively from the tangent rule model and assumes a concave down shape during the transition from one solid to the other (similar to the kinetic barrier of melting described above).

AuGe-system and SnGe-system

T = 300 K

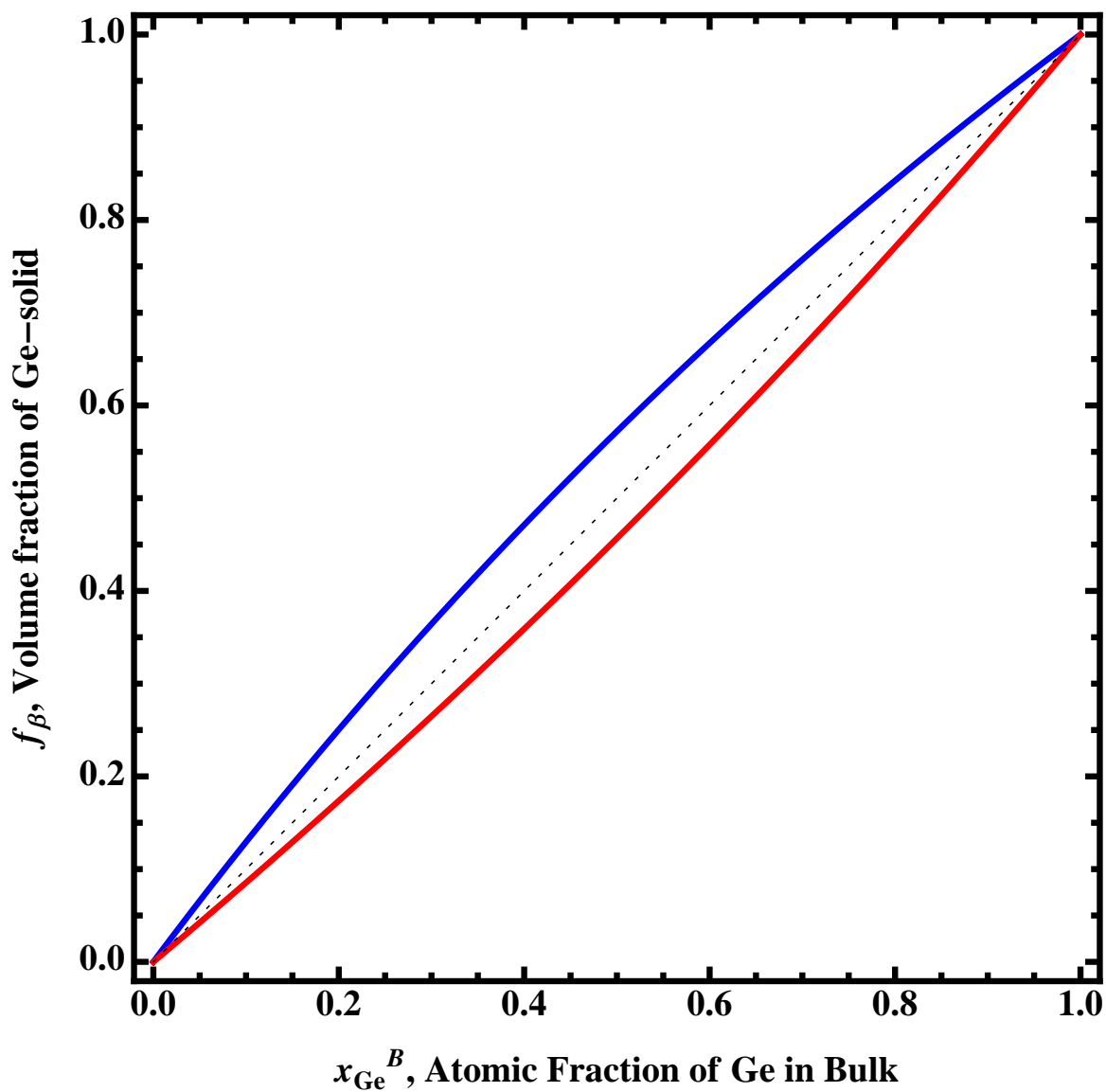


Figure 5.6. Volume fraction of Ge-solid in a solid-solid particle is calculated as a function of Ge content. AuGe (blue) shows a positive deviation from linearity due to the larger molar volume of Ge-solid over Au-solid. The opposite is true for the SnGe-system shown in red.

AuGe solid–solid particle T = 300K

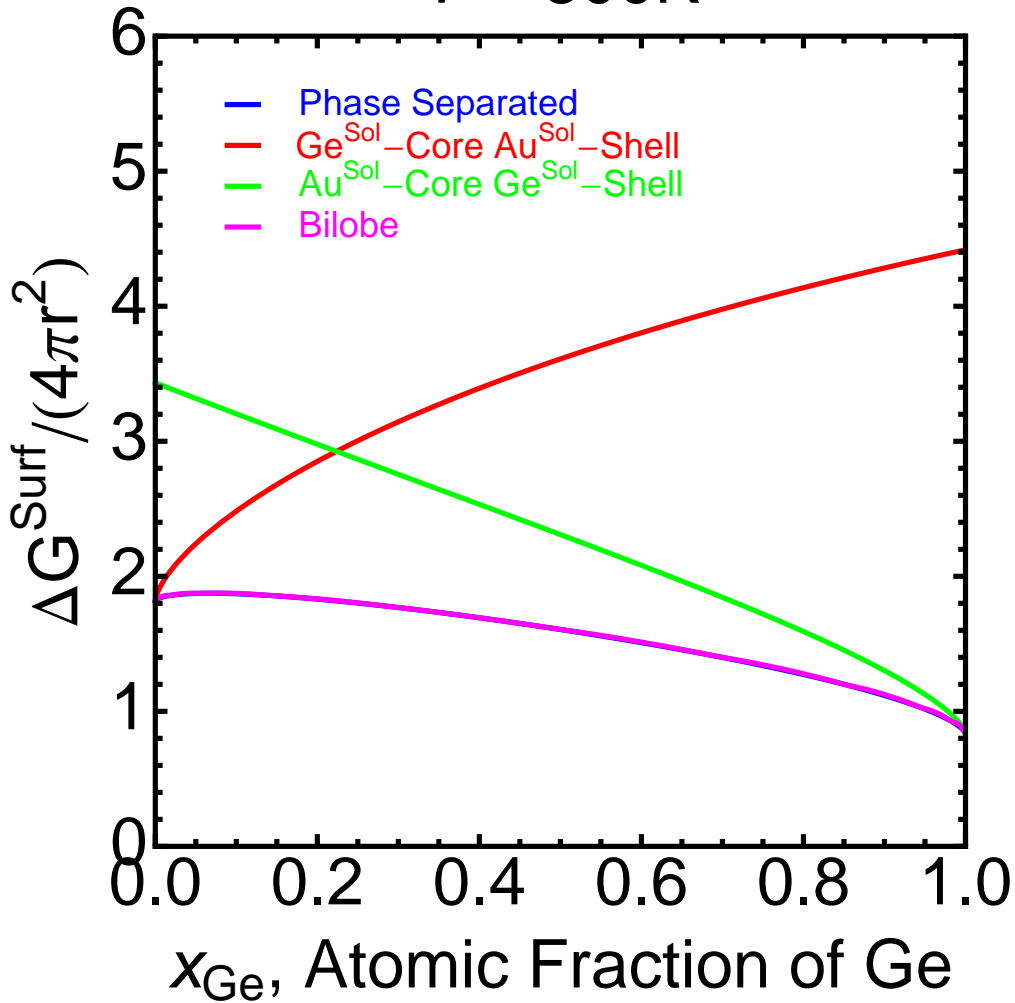


Figure 5.7. The four possible binary alloy nanoparticle morphologies are calculated as a function of Ge-concentration (which in turn can be used to calculate the volume fraction Ge-solid). At a temperature of 300K the surface and interface energies of Au- and Ge-solid phases predict $\{\gamma_1, \gamma_2\} = \{0.699231, 0.320272\}$. This indicates that the bilobe geometry is stable, which is verified as the magenta line representing the energy of the bilobe structure minimizes the surface contribution to the free energy for all compositions. The blue line representing the phase separated morphology is very close to the bilobe prediction and thus not visible.

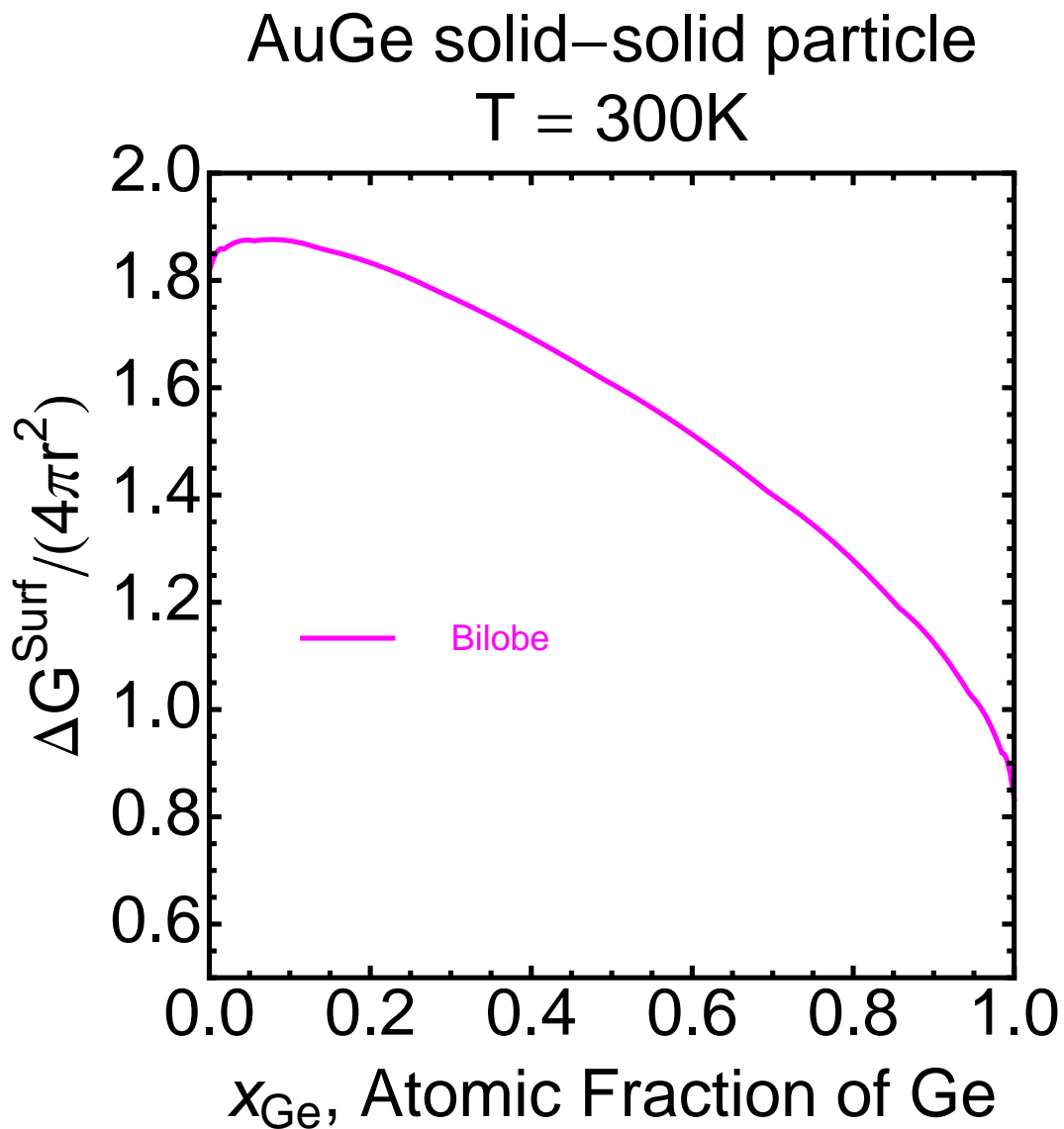


Figure 5.8. The surface contribution to the free energy of the bilobe structure as seen in Figure 5.7 is plotted separately. The expected positive curvature is seen. Therefore, the tangent rule construction is not applicable in this type of nanoscale system.

5.2 Free energy curve of a Liquid particle

The volumetric contribution to the free energy of a liquid particle can be calculated from:

$$\Delta G_{Vol}^L = [(1 - x_{Ge})\Delta G_{S \rightarrow L}^{Au} + x_{Ge}\Delta G_{S \rightarrow L}^{Ge} + RT((1 - x_{Ge}) \log(1 - x_{Ge}) + x_{Ge} \log(x_{Ge})) + G^{Ex,L}] \cdot (x_{Ge}v_{Liq}^{Ge}(T) + (1 - x_{Ge})v_{Liq}^{Au}(T))^{-1}. \quad (5.13)$$

$\Delta G_{S \rightarrow L} = G_L - G_S$ is the difference in volumetric free energy between the solid and the liquid phase and is tabulated in Table 5.1.(14) If Equation 5.13 is reduced to only the first term, $(1 - x_{Ge})\Delta G_{S \rightarrow L}^{Au} + x_{Ge}\Delta G_{S \rightarrow L}^{Ge}$, the solution is considered a mechanical mixture, i.e. there is no chemical mixing.(22) The second term, $RT((1 - x_{Ge}) \log(1 - x_{Ge}) + x_{Ge} \log(x_{Ge}))$, is attributed to the configuration entropy. If Equation 5.13 is reduced to the first two terms, the solution is ideal. However, most systems deviate from the ideal solution model. This deviation is taken into account in the regular solution model through the addition of $G^{Ex,L}$, the excess energy of mixing, which is calculated as discussed in Chapter 4.

The liquid particle is assumed to be spherical in shape. The contribution of the surface is then $4\pi r^2 \cdot \sigma^L$, which is calculated using the surface energies determined in Chapter 4. The total free energy of the liquid particle then becomes:

$$G^L(T, x_{Ge}) = \frac{4}{3}\pi r^3 \cdot \Delta G_{Vol}^L + 4\pi r^2 \cdot \sigma^L. \quad (5.14)$$

Results of this calculation are shown in Figure 5.9 (thick, blue line) for a AuGe-liquid at $T = 1400 \text{ K}$. As a reference, the volumetric contribution is shown as a black, dashed line. Again, the surface contributes positively to the total free energy of the alloy particle.

5.3 Free energy curve of a Particle consisting of Ge-solid and AuGe-Liquid

Consider a particle with overall composition x_{Ge} that is composed of part Ge-solid and part AuGe-liquid with composition x_L . Mass conservation requires that x_{Ge} is larger than x_L . The volume fraction of solid in the particle can be calculated from the following:

$$f_\beta(T, x_{Ge}, x_L) = \frac{(\frac{x_{Ge}-x_L}{1-x_L})v_{Sol}^{Ge}(T)}{(\frac{1-x_{Ge}}{1-x_L})(x_L \cdot v_{Liq}^{Ge}(T) + (1 - x_L) \cdot v_{Liq}^{Au}(T)) + (\frac{x_{Ge}-x_L}{1-x_L})v_{Sol}^{Ge}(T)}. \quad (5.15)$$

$f_\beta(T, x_{Ge}, x_L)$ is calculated for $T = 300 \text{ K}$ and $x_L = 0.4$ at. % Ge and shown in Figure 5.10. While $v_{Au_{1-x}Ge_x}^{Liq}$ is calculated using a concentration weighted average(21), due to the differences in molar volumes, the volume fraction deviates from linearity.

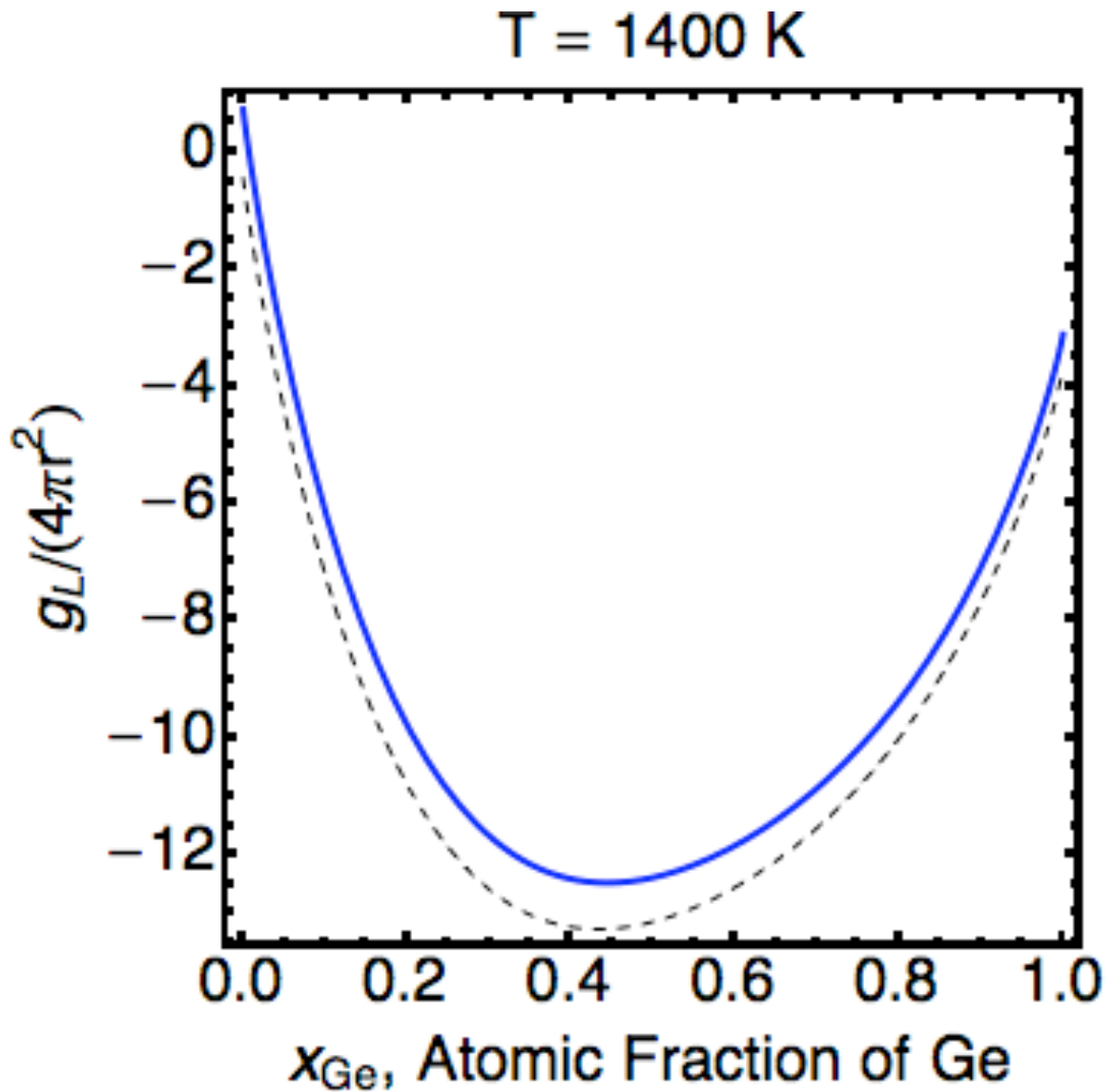


Figure 5.9. The free energy curve of a AuGe-liquid alloy is calculated as a function of composition. The black dotted line represents the volumetric contribution. The thick, blue line represents the total energy of the liquid alloy after the surface contribution has been taken into account. This leads to an increase in the overall free energy when normalized by the total surface area.

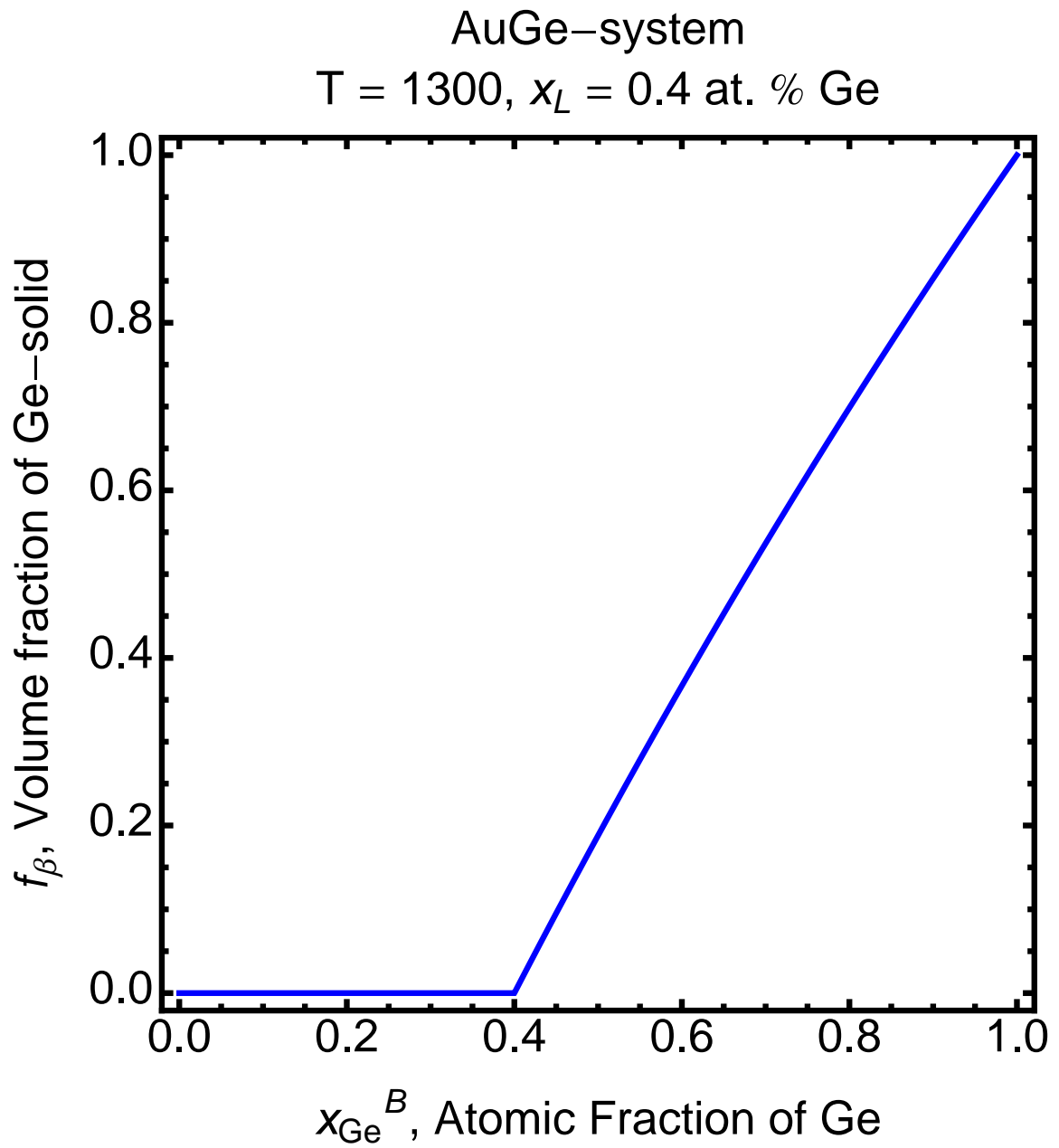


Figure 5.10. Volume fraction of Ge-solid in a particle consisting of Ge-solid and a AuGe-liquid of composition $x_L = 40$ at. % Ge as a function of alloy composition, x_{Ge} .

The surface contribution is calculated using the three applicable surface/interface energies: σ_{Ge}^S , σ^L and $\sigma^{Ge(sol)L}$, which are all dependent on temperature, and the latter two are dependent on the composition of the liquid, x_L . These energies dictate which structure minimizes the total energy. As an example, Figure 5.11 shows the contribution of the surface/interface energies at a temperature of $T = 1300 K$ and liquid composition of $x_L = 0.40$. Clearly, the bilobe structure minimizes the energy, and thus the overall energy of the particle becomes:

$$G^{Ge(sol)L}(T, x_{Ge}, x_L) = (1 - f_\beta(T, x_{Ge}, x_L)) \cdot \frac{4}{3}\pi r^3 \cdot \Delta G_{Vol}^L + A^{Ge(sol)} \cdot \sigma^{Ge(sol)} + A^L \cdot \sigma^L + A^{Ge(sol)L} \cdot \sigma^{Ge(sol)L} \quad (5.16)$$

Results of a representative calculation are shown in Figures 5.12 and 5.13 for a particle size of $r = 25 \times 10^{-9}m$ and $r = 5 \times 10^{-9}m$, respectively. First consider Figure 5.12. Plotted are the total free energy of the solid-solid particle (blue), $G^{Au(sol)Ge(sol)}$, the pure liquid particle (red), G^L , and various curves for particles consisting of Ge-solid and AuGe-liquids (purple), $G^{Ge(sol)L}(T, x_{Ge}, x_L)$. $G^{Ge(sol)L}(T, x_{Ge}, x_L)$ is calculated for compositions of liquids $x_L = 0.01, 0.05, 0.10, 0.15, 0.20, 0.25, 0.30, 0.35, 0.40, 0.45, 0.51, 0.55, 0.60, 0.65, 0.70, 0.75, 0.80, 0.85, 0.90, 0.95, 0.99$. We point out that the purple curves appear very linear, which is attributed to the rather large size of the nanoparticle under consideration, i.e. the volumetric component still outweighs the surface contribution. Since equilibrium is achieved when the overall energy of the system is minimized, all compositions, x_{Ge} , indicate a solid-solid particle to be stable. These findings are consistent with the bulk phase diagram of AuGe at a temperature of $300K$. However, once the particle size is decreased to, for example, $r = 5 \times 10^{-9}m$, this is no longer the case.

Consider now Figure 5.13, which plots the same information as Figure 5.12 (just at a much smaller particle size of $r = 5 \times 10^{-9}m$). First, we notice that the $G^{Au(sol)Ge(sol)}$ line shows no change, since it is normalized by $4\pi r^2$ in both cases. However, G^L , indicated by the red line, shows a marked decrease due to the particle size. To clarify this, and for ease of viewing, a magnified view of these results is shown in Figure 5.14. It is immediately clear that the stable phases predicted are now different than those of the larger particle. Subsequently, we must examine each composition, x_{Ge} individually, and determine which phase, solid-solid, liquid, or solid-liquid, minimizes the total energy of the particle. From the image, compositions below approximately $x_{Ge} \approx 0.35$ should exist as the solid-solid phase, as this phase assumes the lowest energy. However, at compositions greater than $x_{Ge} \approx 0.35$ a solid-liquid phase is predicted. This is unlike the bulk phase diagram, as the liquid phase is greater than the solid-solid phase over the entire composition phase, yet the energy can be minimized by splitting into a liquid-solid particle. These findings are directly attributed to the particle size and the resulting curvature of the solid-solid curve, as well as the decrease in energy of the liquid-line. Furthermore, the apparent discontinuity in the solid-liquid curves at $x_L = 0.01$ and $x_L = 0.05$ should be mentioned. At low Ge-concentrations, the surface energy of the AuGe-liquid is sufficiently high in comparison to the Ge-solid surface energy and the interface energy that the nanoparticle

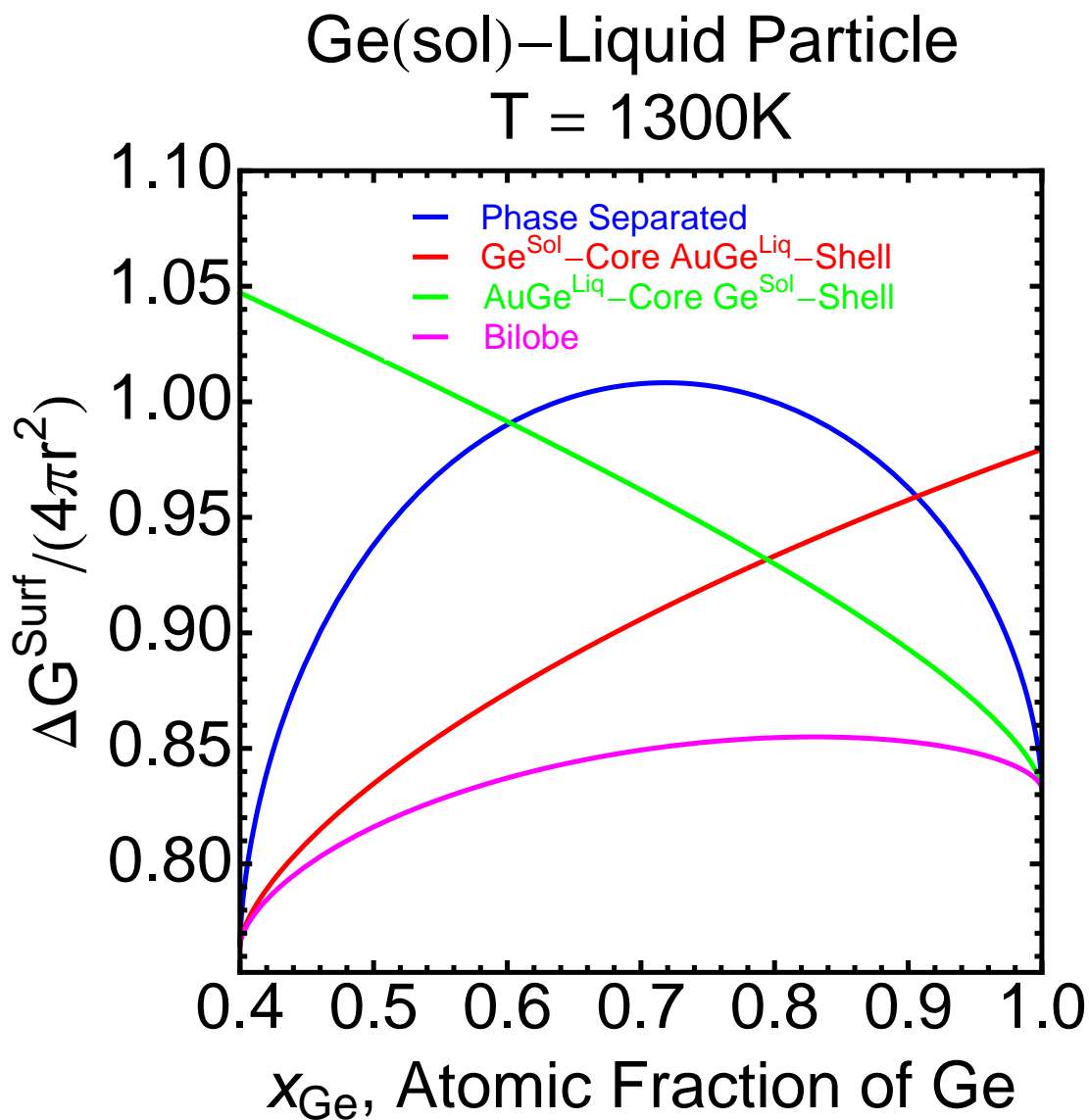


Figure 5.11. The four possible binary alloy nanoparticle morphologies are calculated as a function of Ge-concentration at a temperature of 1300K and $x_L = 0.40$. The contribution of the surfaces/interfaces to the total energy is minimized by the bilobe geometry.

Pure Solid, Pure Liquid and Solid–Liquid Particle

$T = 300 \text{ K}$, $r = 25 \times 10^{-9} \text{ m}$

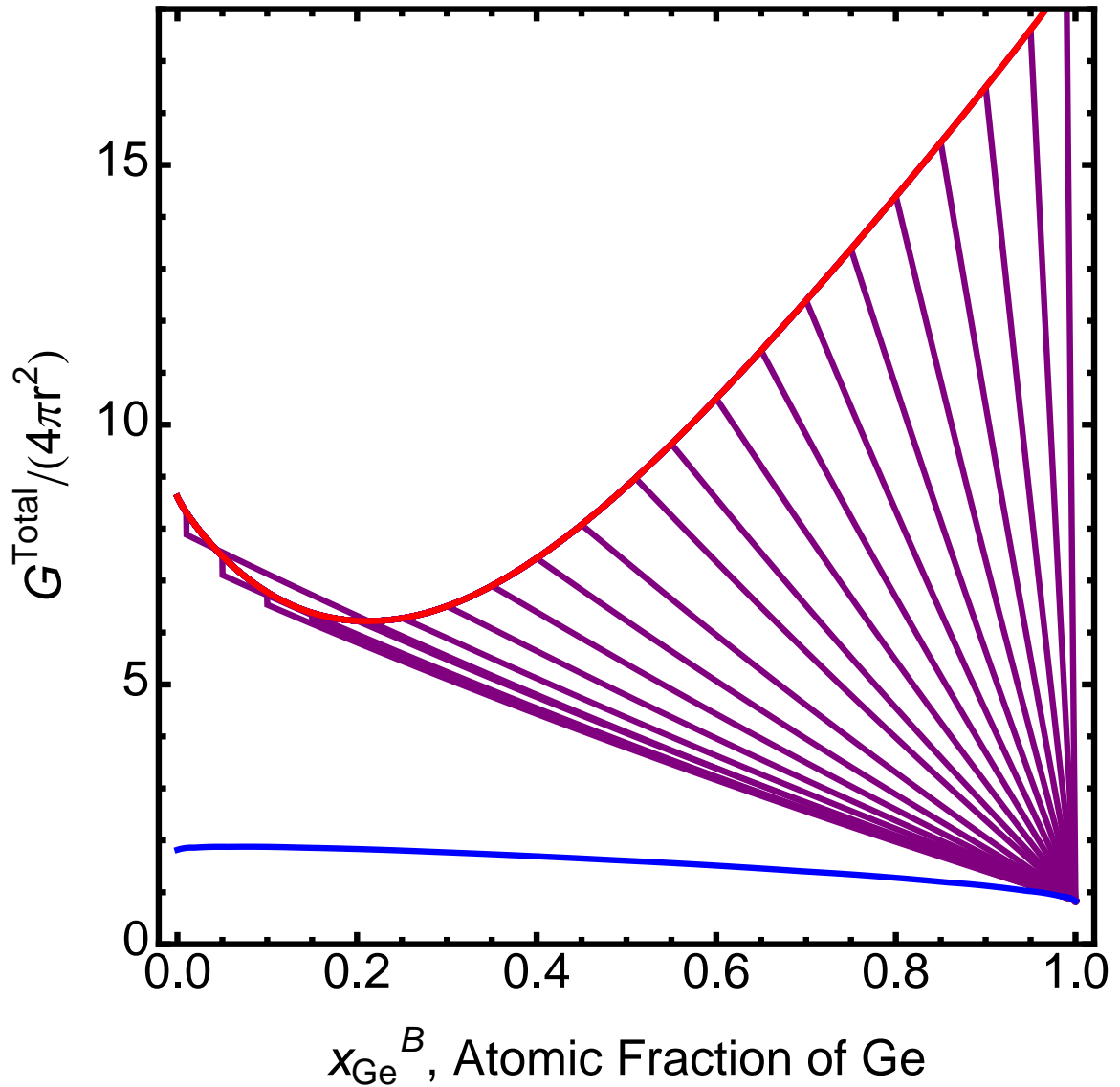


Figure 5.12. $G^{Au(sol)Ge(sol)}(x_{Ge})$ (blue), $G^L(T, x_{Ge})$ (red) and $G^{Ge(sol)L}(T, x_{Ge}, x_L)$ (purple) are calculated for a particle of size $r = 25 \times 10^{-9} \text{ m}$. Liquids of composition $x_L = 0.01, 0.05, 0.10, 0.15, 0.20, 0.25, 0.30, 0.35, 0.40, 0.45, 0.51, 0.55, 0.60, 0.65, 0.70, 0.75, 0.80, 0.85, 0.90, 0.95, 0.99$ are considered for $G^{Ge(sol)L}(T, x_{Ge}, x_L)$.

Pure Solid, Pure Liquid and Solid–Liquid Particle

$T = 300 \text{ K}$, $r = 5 \times 10^{-9} \text{ m}$

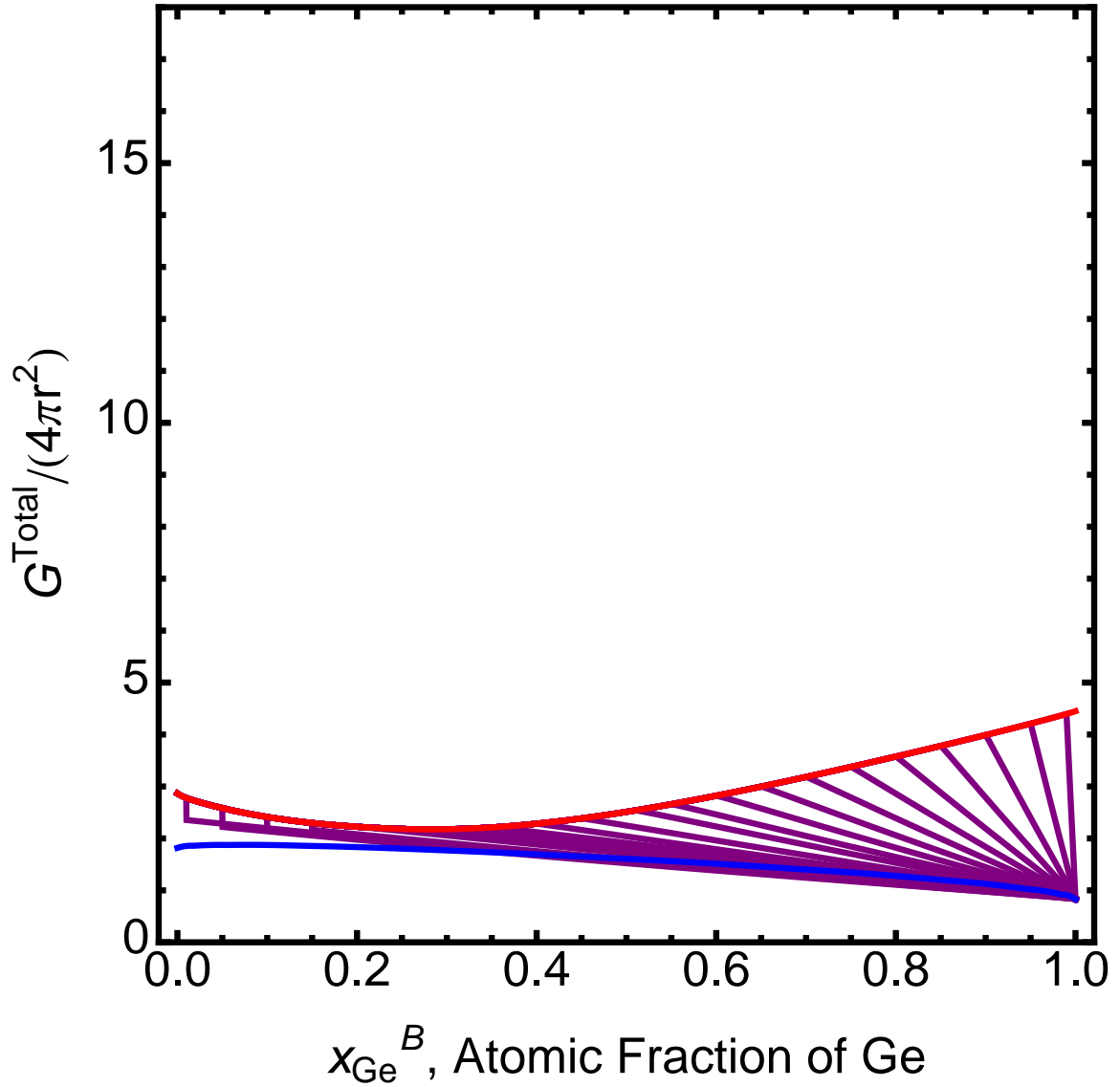


Figure 5.13. $G^{Au(sol)Ge(sol)}(x_{Ge})$ (blue), $G^L(T, x_{Ge})$ (red) and $G^{Ge(sol)L}(T, x_{Ge}, x_L)$ (purple) are calculated for a particle of size $r = 5 \times 10^{-9}m$. Liquids of composition $x_L = 0.01, 0.05, 0.10, 0.15, 0.20, 0.25, 0.30, 0.35, 0.40, 0.45, 0.51, 0.55, 0.60, 0.65, 0.70, 0.75, 0.80, 0.85, 0.90, 0.95, 0.99$ are considered for $G^{Ge(sol)L}(T, x_{Ge}, x_L)$.

assumes a liquid-core/solid-shell structure to minimize its energy. This change leads to a sudden drop in total energy as soon as the volume fraction of solid Ge exceeds $f_{Ge(sol)} = 0$. Furthermore, we should note that the solid-liquid lines also display a positive deviation from linearity. Therefore, it is not guaranteed that all compositions above $x_{Ge} \approx 0.35$ are minimized by a liquid-solid particle of the same liquid composition. Thus, every composition requires a separate investigation and the minimizing structure must be ascertained.

5.4 Free energy curve of a Particle consisting of Au-solid and AuGe-Liquid

Finally, we consider a particle with overall composition x_{Ge} that is composed of part Au-solid and part AuGe-liquid with composition x_L . The volume fraction of liquid, f_β , can be calculated by:

$$f_\beta(T, x_{Ge}, x_L) = \frac{\left(\frac{x_{Ge}}{x_L}\right)v_{Sol}^{Ge}(T)}{\left(\frac{x_L - x_{Ge}}{x_L}\right)(x_L \cdot v_{Liq}^{Ge}(T) + (1 - x_L) \cdot v_{Liq}^{Au}(T)) + \left(\frac{x_{Ge}}{x_L}\right)v_{Sol}^{Ge}(T)}. \quad (5.17)$$

Unlike before, mass conservation requires $x_{Ge} \leq x_L$ to allow for a solid-liquid particle. Figure 5.15 shows the volume fraction of AuGe-liquid, $f_\beta(T, x_{Ge}, x_L)$, for $T = 300 \text{ K}$ and $x_L = 0.4 \text{ at. } \% \text{ Ge}$. Again, due to the differences in molar volumes, the volume fraction deviates from linearity.

Now, the surface contribution must be calculated using three new surface/interface energies: σ_{Au}^S , σ^L and $\sigma^{Au(sol)L}$, which are all dependent on temperature, and the latter two are dependent on the composition of the liquid, x_L . These energies dictate which structure minimizes the total energy. σ_{Au}^S and σ^L are known or have been calculated as discussed in the preceding chapters. While $\sigma^{Au(sol)L}$ is not known, $\sigma^{Au(sol)Au(liq)}$ has been estimated to be 0.187 J/m^2 .(29) Therefore, we will assume that the composition dependence of $\sigma^{Au(sol)L}$ is equal to that of $\sigma^{Ge(sol)L}$ (measured by Naidich and Perevertailo(43)), but shifted such that $\sigma^{Au(sol)Au(liq)} = 0.187 \text{ J/m}^2$ (added term of 0.054 J/m^2). The total energy of the particle then becomes:

$$G^{Ge(sol)L}(T, x_{Ge}, x_L) = f_\beta(T, x_{Ge}, x_L) \cdot \frac{4}{3}\pi r^3 \cdot \Delta G_{Vol}^L + A^{Au(sol)} \cdot \sigma^{Au(sol)} + A^L \cdot \sigma^L + A^{Au(sol)L} \cdot \sigma^{Au(sol)L} \quad (5.18)$$

The energies of the four structures are calculated at a temperature of 1300 K and liquid composition of $x_L = 0.40$ and shown in Figure 5.16. Clearly, the Au(sol)-core/AuGe(liq)-shell structure is the preferred morphology in this case ($T_M^{Au} = 1336 \text{ K}$).

As was the case in the Ge(sol)-liquid particle discussed above, $G^{Au(sol)Ge(sol)}$, G^L , and all curves for particles consisting of Au-solid and AuGe-liquids (purple),

Pure Solid, Pure Liquid and Solid–Liquid Particle

$T = 300 \text{ K}, r = 5 \cdot 10^{-9} \text{ m}$

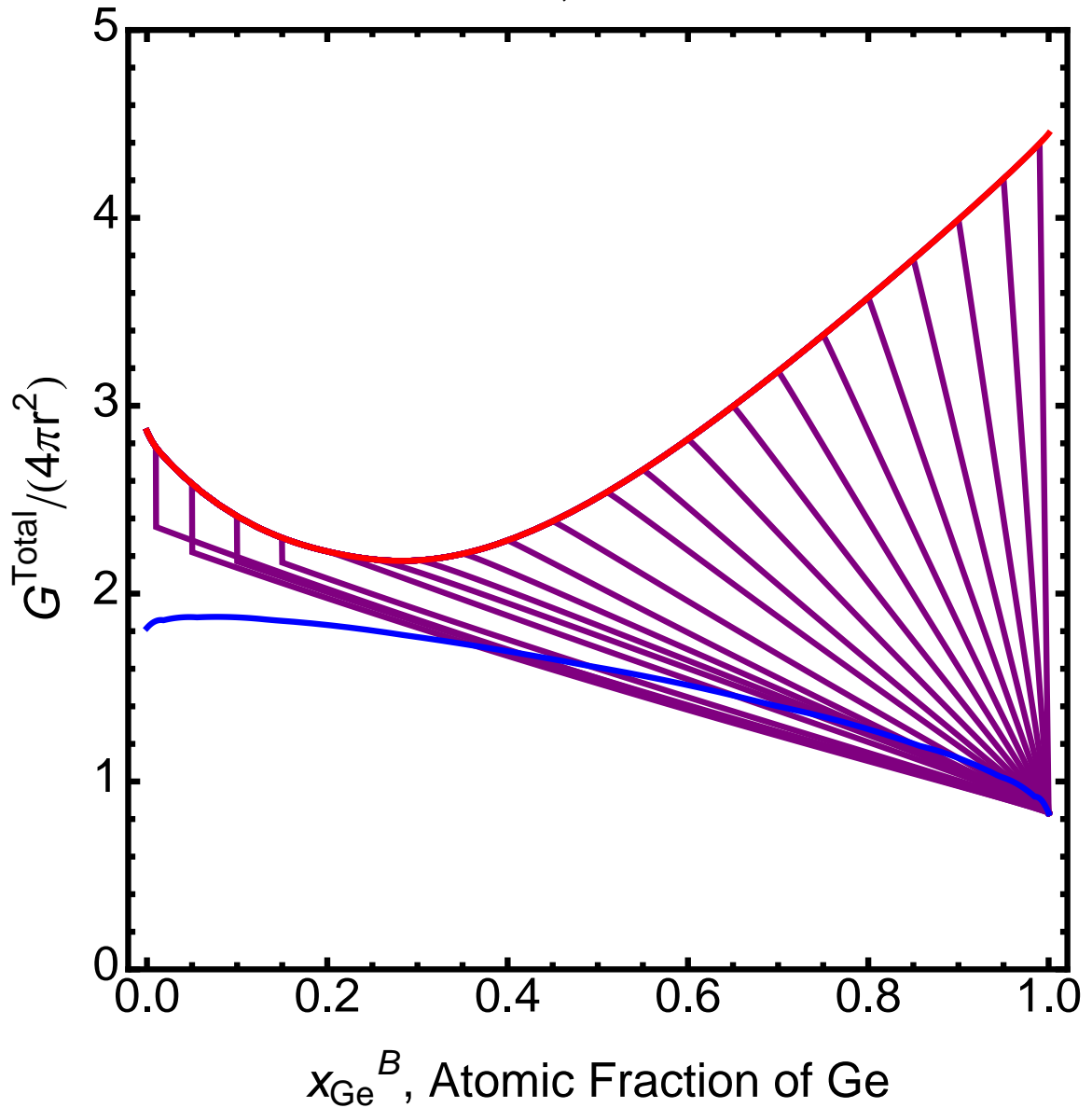


Figure 5.14. Magnified view of Figure 5.13. Clearly, the solid-liquid phase minimizes the overall energy at compositions above ≈ 0.35 , while at larger particle size the solid-solid phase is stable.

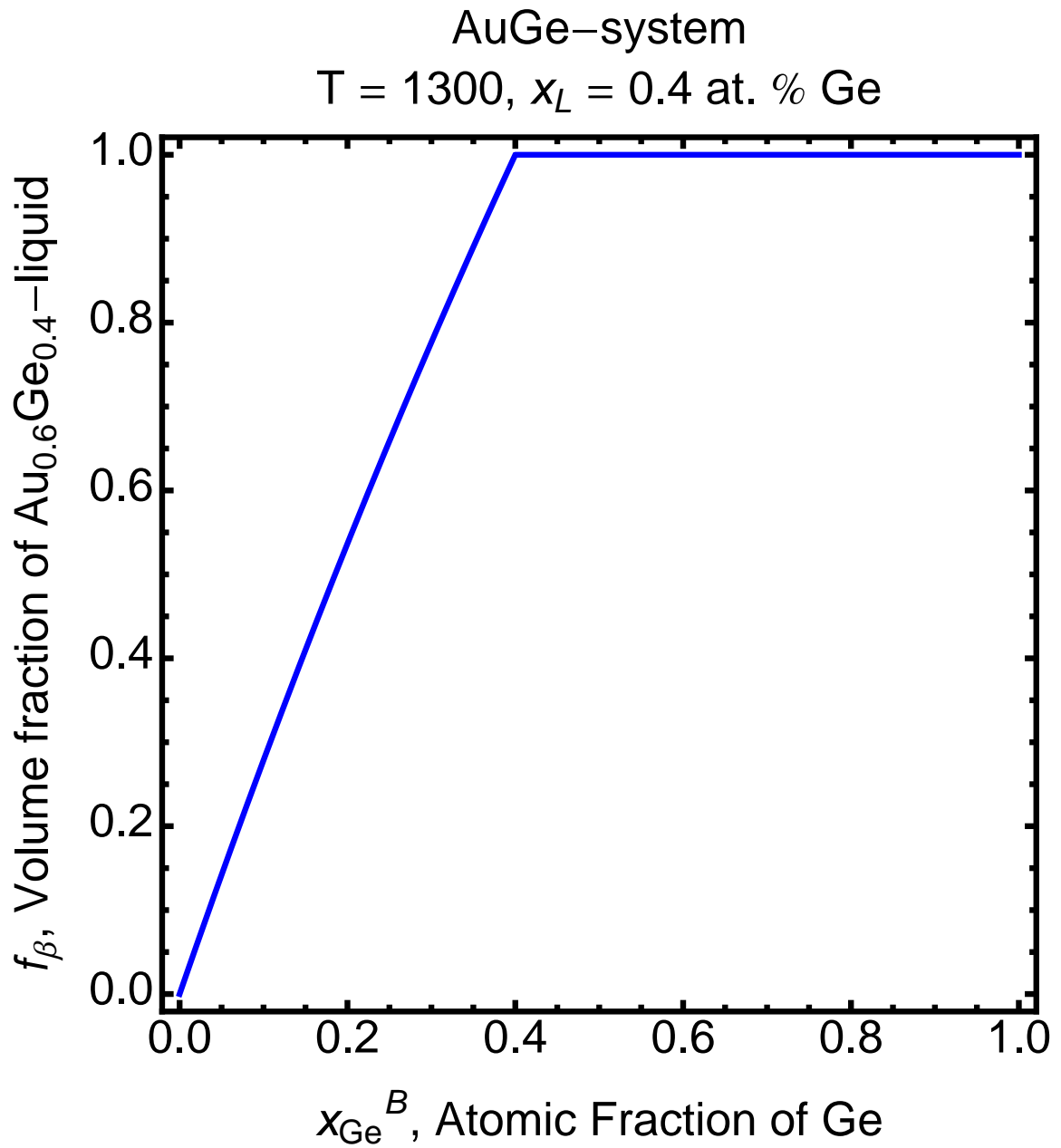


Figure 5.15. Volume fraction of $Au_{0.6}Ge_{0.4}$ -liquid in a particle consisting of Au-solid and a AuGe-liquid of composition $x_L = 0.4$ at. % Ge as a function of alloy composition, x_{Ge} .

Au(sol)–Liquid Particle T = 1300K

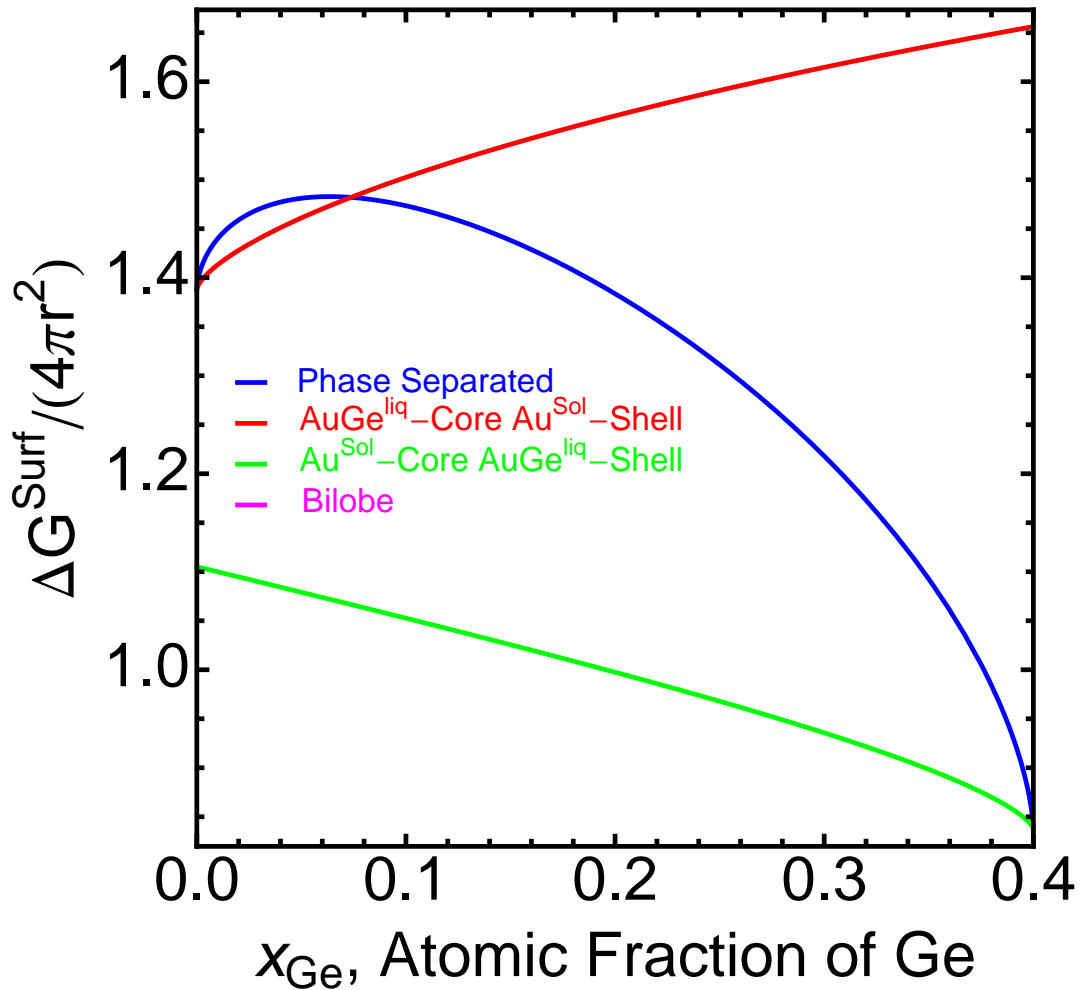


Figure 5.16. The four possible binary alloy nanoparticle morphologies are calculated as a function of Ge-concentration at a temperature of 1300K and $x_L = 0.40$. The Au(sol)-core/AuGe(liq)-shell structure minimizes the contribution of the surfaces/interfaces to the total energy. At these temperatures and compositions, the bilobe structure cannot be realized.

$G^{Au(sol)L}(T, x_{Ge}, x_L)$, must be considered at each temperature. Results of this calculation, and the calculations discussed above, are shown in Figure 5.17 for a particle of size, $r = 5 \times 10^{-9}$ m at $T = 300$ K. The assumed interface energy, $\sigma^{Au(sol)L}$, in conjunction with the values of σ_{Au}^S and σ^L determine the solid-core/liquid-shell structure to minimize the overall energy of the system. Consequently, a sharp decrease in energy is observed as the composition moves just slightly away from pure Au. Therefore, all calculations will also be performed at values of $\sigma^{Au(sol)L}$, which guarantee a stable bilobe structure. This can be achieved by shifting the values of $\sigma^{Ge(sol)L}$ up by 2 J/m²: $\sigma^{Au(sol)L} = \sigma^{Ge(sol)L} + 2$. These results are shown in Figure 5.18. Interestingly, in the first case (see Figure 5.17), all compositions predict either a Au(sol)-liquid or Ge(sol)-liquid structure even at temperatures as low as 300 K. Alternatively, when $\sigma^{Au(sol)L} = \sigma^{Ge(sol)L} + 2$, all Au(sol)-liquid curves lie at higher energies than the Au(sol)-Ge(sol) curve, which leads to a composition range that is stable in the solid-solid phase ($x_{Ge} \leq \approx 0.30$), while compositions with greater Ge content split into Ge(sol) and AuGe(liq).

5.5 Nanoscale Phase Diagram of Free-standing AuGe particles

In the following section, nanoscale phase diagrams of the AuGe system will be determined as discussed above. The results will be compared to the “bulk” phase diagram (calculated using the tangent rule and assuming no solid-solubility and no surface contribution), the “standard nanoscale” phase diagram (calculated using the tangent rule construction and assuming no solid-solubility; however, taking into account the surface contributions of both the solid and liquid phases), and qualitatively to the phase diagrams calculated by Weissmueller *et al.*

Figure 5.19 shows the phase diagrams of a theoretical system for particle sizes $r = 25 \times 10^{-9}$, 10×10^{-9} and 5×10^{-9} m in the top, center and bottom panels, respectively. These phase diagrams are calculated using the theoretical approach outlined by Weissmueller *et al.*(68; 8; 69) Two important and prominent features should be noted: the spreading of the eutectic point indicating a region of discontinuous melting and the variance of the eutectic temperature as a function of composition. These two features become increasingly pronounced as the particle size is decreased.

First, a relatively large AuGe particle of size $r = 25 \times 10^{-9}$ m is considered. As discussed above, $\sigma^{Au(sol)L}$ will first be assumed to be equal to $\sigma^{Ge(sol)L} + 0.054$ (see above) and then $\sigma^{Ge(sol)L} + 2$. Results of these calculations are shown in the top left and top right plots of Figure 5.20, respectively.

In each figure, the black, dotted line represents the “bulk” phase diagram, while the black, solid line represents the “standard nanoscale” phase diagram. The colored

Pure Solid, Pure Liquid and Solid–Liquid Particle

$T = 300 \text{ K}, r = 5 \cdot 10^{-9} \text{ m}$

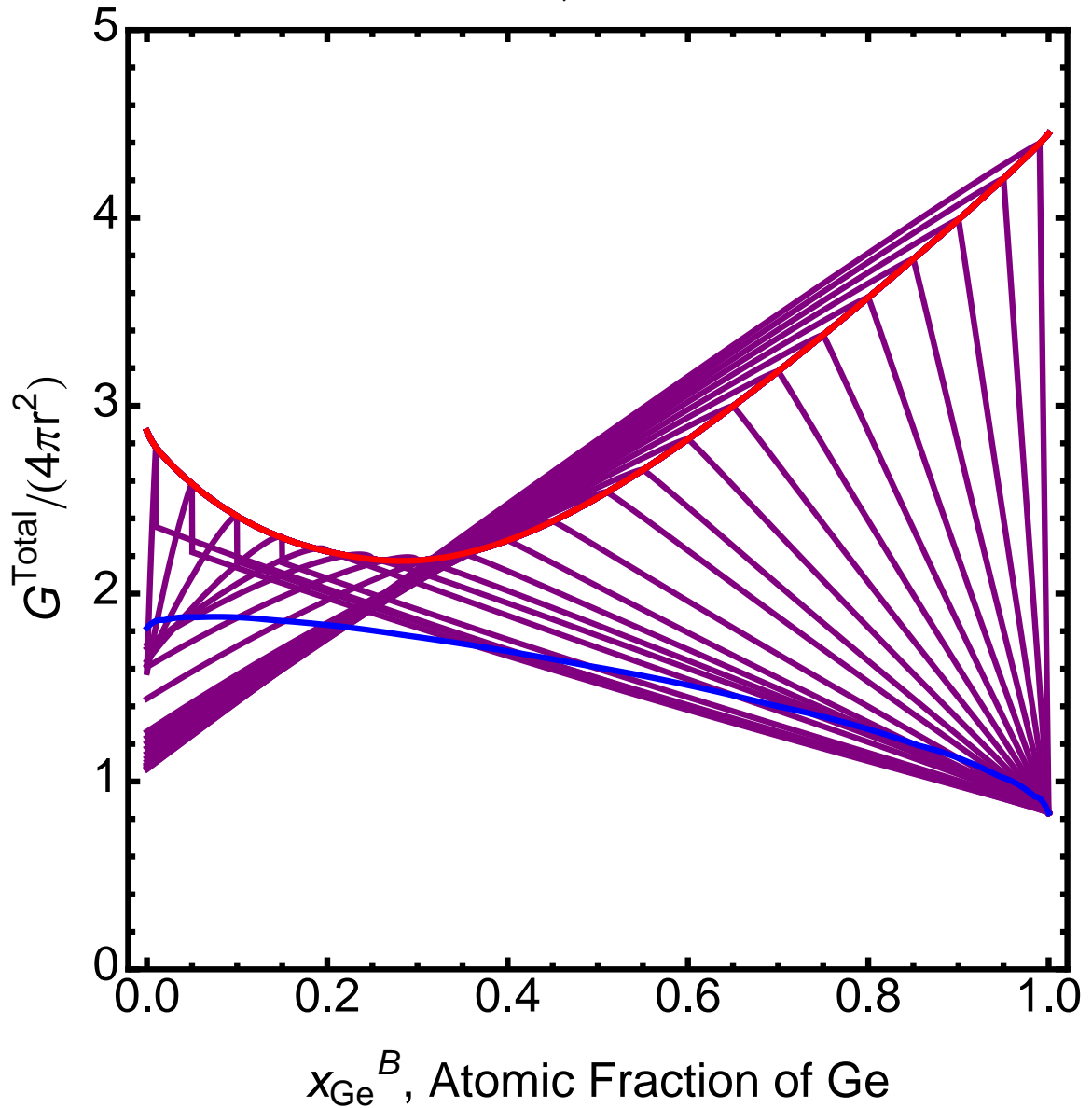


Figure 5.17. $G^{Au(sol)Ge(sol)}(x_{Ge})$ (blue), $G^L(T, x_{Ge})$ (red), $G^{Ge(sol)L}(T, x_{Ge}, x_L)$ and $G^{Au(sol)L}(T, x_{Ge}, x_L)$ (both shown in purple) are calculated for a particle of size $r = 5 \times 10^{-9} \text{ m}$ as a function of alloy composition, x_{Ge} .

Pure Solid, Pure Liquid and Solid–Liquid Particle

$T = 300 \text{ K}, r = 5 \cdot 10^{-9} \text{ m}$

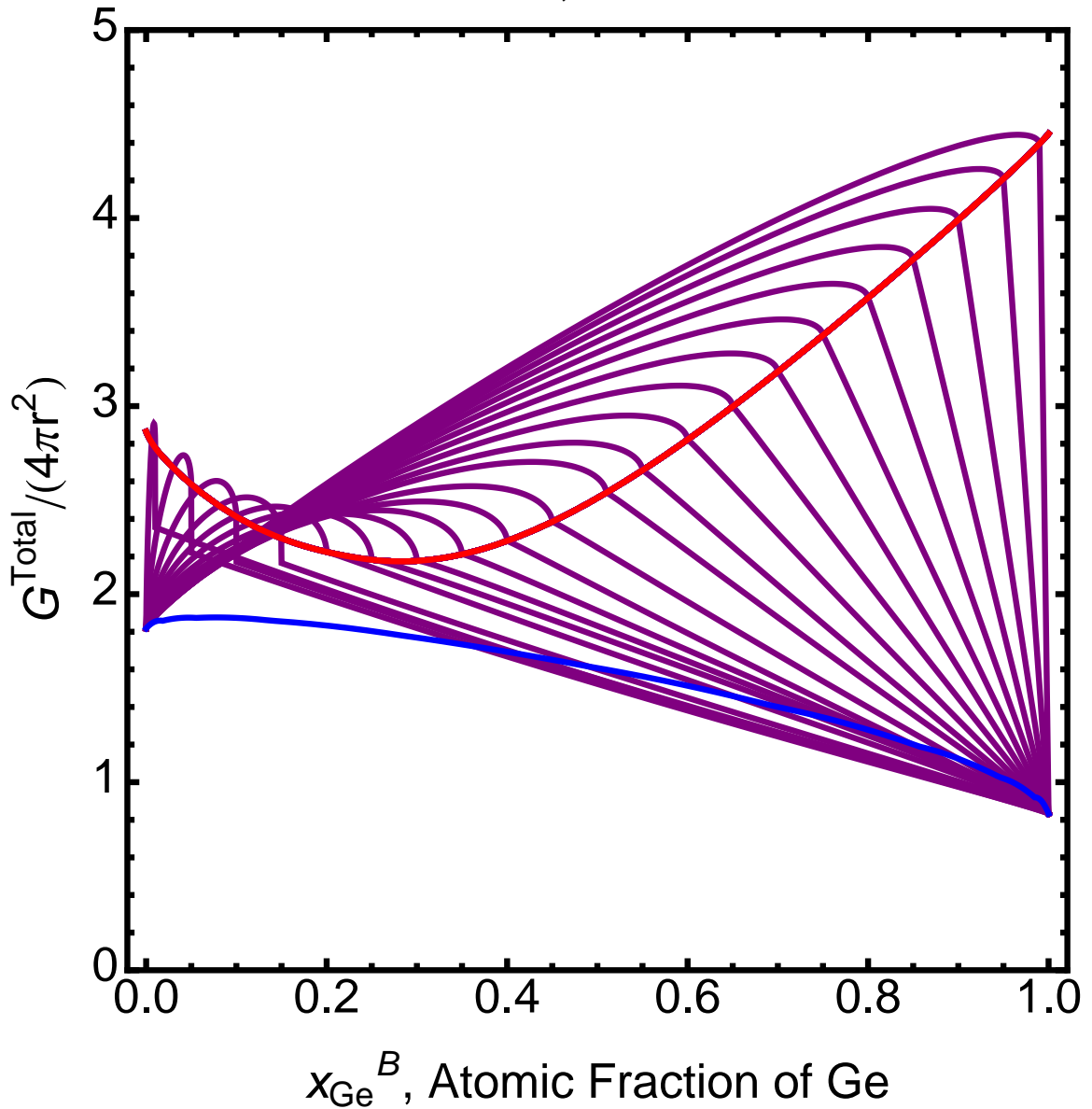


Figure 5.18. $G^{Au(sol)Ge(sol)}(x_{Ge})$ (blue), $G^L(T, x_{Ge})$ (red), $G^{Ge(sol)L}(T, x_{Ge}, x_L)$ and $G^{Au(sol)L}(T, x_{Ge}, x_L)$ (both shown in purple) are calculated for a particle of size $r = 5 \times 10^{-9} \text{ m}$ as a function of alloy composition, x_{Ge} . $\sigma^{Au(sol)L} = \sigma^{Ge(sol)L} + 2$

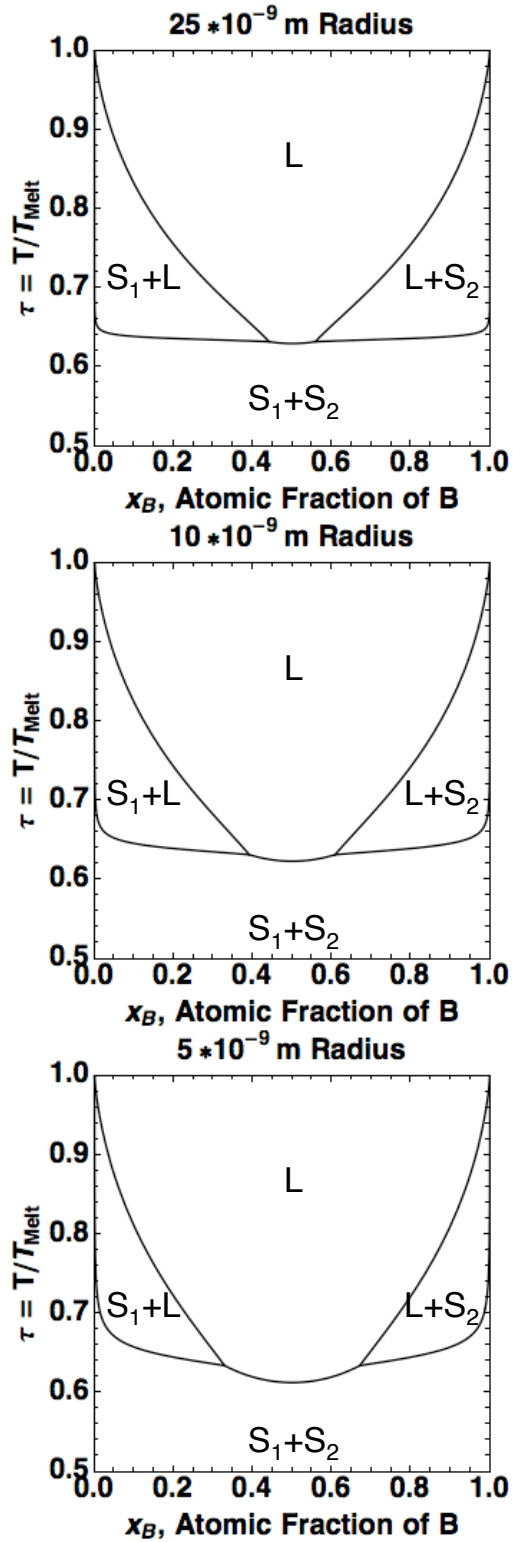


Figure 5.19. Theoretical phase diagrams of particles of sizes $r = 25 \times 10^{-9}$, 10×10^{-9} and 5×10^{-9} m are shown in the top, center and bottom plots, respectively. These phase diagrams are calculated using the theoretical approach outlined by Weissmueller *et al.*(68; 8; 69)

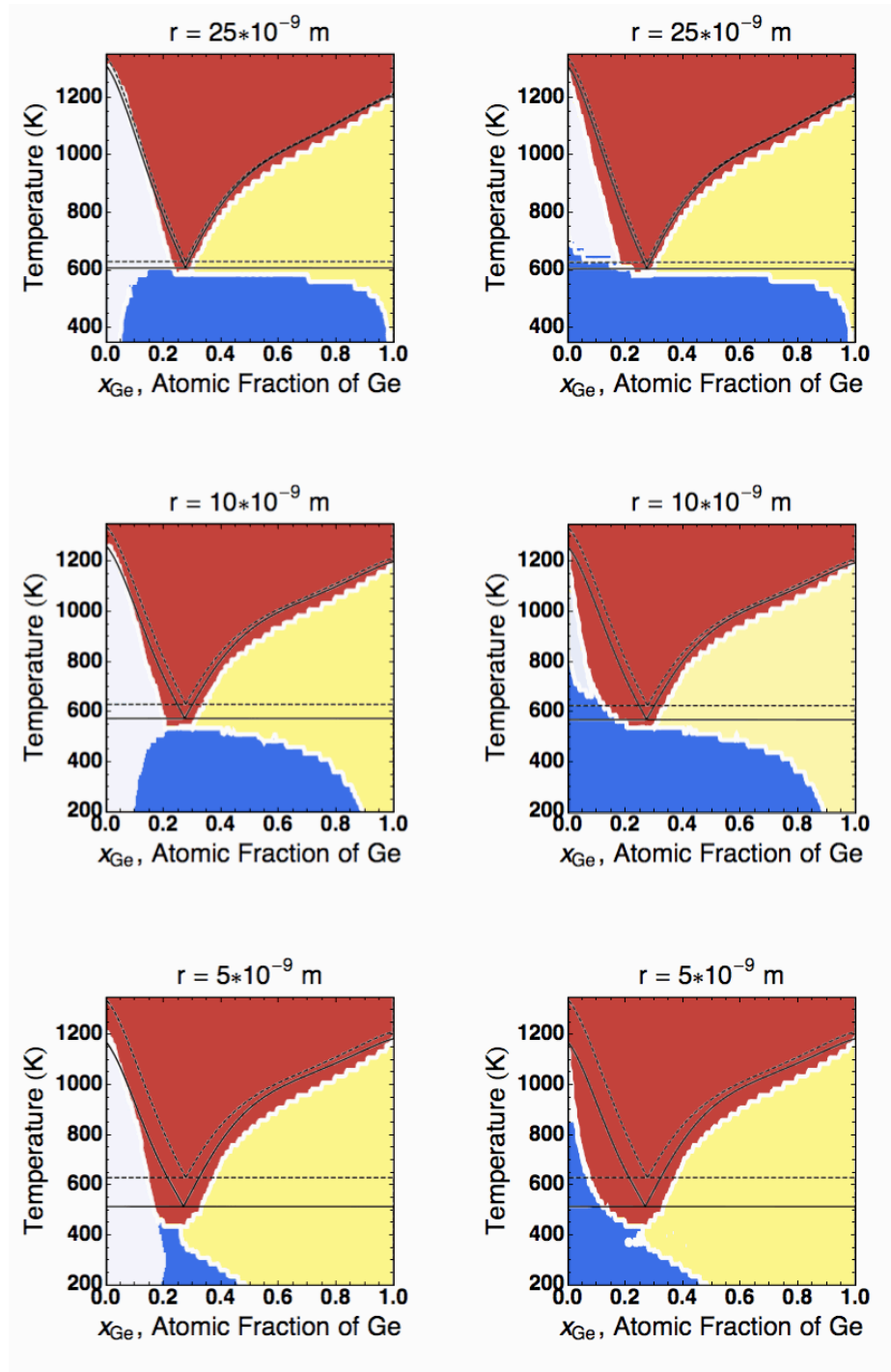


Figure 5.20. The size dependent phase diagrams of the AuGe system are calculated. Three particle sizes are considered: $r = 25 \times 10^{-9}$, 10×10^{-9} and 5×10^{-9} m, which are shown in the top, center and bottom panels, respectively. The left column considers assumed values of $\sigma^{Au(sol)L} = \sigma^{Ge(sol)L} + 0.054$, while the right column considers $\sigma^{Au(sol)L} = \sigma^{Ge(sol)L} + 2$. The black, dotted and black, solid lines represent the “bulk” and “standard nanoscale” phase diagrams, respectively. Phases under consideration are: Au-solid/Ge-solid (dark blue), homogenous liquid (red), Au-solid/liquid (light blue) and Ge-solid/liquid (yellow).

regions are indicative of the results of the calculations performed in this work. Dark blue represents the Au-solid/Ge-solid phase, while red represents the homogenous liquid phase. The light blue and yellow regions indicate the Au-solid/liquid and Ge-solid/liquid phases, respectively.

Clearly, in both cases ($\sigma^{Ge(sol)L} + 0.054$ and $\sigma^{Ge(sol)L} + 2$), there are marked differences between the phase diagrams calculated herein and the “bulk” and “standard nanoscale” phase diagrams. However, the overall expected trends are in fact observed. As expected, the melting temperatures of the elemental solids decrease, therefore causing a decrease in the liquidus lines.

In the case of $\sigma^{Ge(sol)L} + 0.054$, both liquidus lines are very similar to those calculated by the “standard nanoscale” phase diagram. The most prominent difference however is found in the regions of very low and very high Ge concentration. In both regions, the respective solid/liquid phases (Au-solid/liquid and Ge-solid/liquid) are energetically favorable when all surface and interface energies are taken into account. This behavior is not predicted in the “standard nanoscale” phase diagrams. Furthermore, the eutectic point broadens to a range of compositions, indicating a region (24-29 at. % Ge) of discontinuous melting, which is consistent with the predictions made by Weissmueller *et al.* (see Figure 5.19)

Next, consider the case of $\sigma^{Ge(sol)L} + 2$ shown in the top, right corner of Figure 5.20. Again, the eutectic point has spread to a eutectic region ranging from $\approx 17 - 29$ at. % Ge, indicating that a particle in this composition range is predicted to melt discontinuously. Now, consider the Ge-rich portion of the phase diagram. As the composition approaches $x_{Ge} = 1$, the eutectic line, which is invariant in the “bulk” and “standard nanoscale” phase diagrams, curves downward toward lower temperatures (just as in the case of $\sigma^{Ge(sol)L} + 0.054$). These findings signify that a Ge-rich nanoscale system can lower its’ total energy by existing in a Ge-solid/liquid phase, rather than a Ge-solid/Au-solid phase, even at temperatures significantly below the “bulk” and “standard nanoscale” eutectic temperature.

Now, consider the Au-rich region of the phase diagram. As predicted by Weissmueller, the eutectic line is no longer invariant with composition, but instead curves to higher temperatures as the concentration of Ge approaches 0, indicating that at low Ge concentration, the solid-solid particle has the lowest total energy. This is attributed to the higher degree of curvature predicted by the bilobe morphology for the solid-liquid particle than the solid-solid particle. However, once the Ge concentration is increased sufficiently, the total energy of the solid-liquid particle is minimal.

Next, consider a system of particle size $r = 10 \times 10^{-9}$ m. Again, the cases of $\sigma^{Ge(sol)L} + 0.054$ and then $\sigma^{Ge(sol)L} + 2$ are considered and shown in the left and right center panels of Figure 5.20, respectively. While the liquidus lines of the Ge-rich portion of the phase diagram are similar to those predicted by the “standard nanoscale” phase diagrams, the eutectic lines deviate significantly. In both cases (+0.054 and +2), the spreading of the eutectic point is observed, but to a greater extent than was discussed above. This is directly attributed to the decrease in particle

size. Also, particles with Ge concentration above 87 at. % are predicted to display Ge-solid/liquid behavior at temperatures below even 200 K .

Again, as the composition approaches 0 at. % Ge, the eutectic line differs significantly from that predicted in the “standard nanoscale” phase diagram. As described above, the eutectic line loses its invariance. It decreases drastically for the case of $\sigma^{Ge(sol)L} + 0.054$, while an increase is observed for the case of $\sigma^{Ge(sol)L} + 2$. Again, this second result is consistent with the predictions of Weissmueller.(68; 8; 69) Furthermore, the Au-rich liquidus line shows a significant depression from that of the “bulk” and “standard nanoscale” phase diagrams, which is also consistent with Weissmuellers’ predictions.

When the particle size is decreased further, the above described characteristics become more pronounced. Results are shown in the bottom left and right panels of Figure 5.20 for a particle of size $r = 5 \times 10^{-9}$ m. In the left plot(+0.054), the solid/solid region has almost disappeared at the temperatures under investigation. The eutectic point has spread to a region between 18 – 26 at. % Ge. In the right panel of Figure 5.20, the results of the calculation for $\sigma^{Ge(sol)L} + 2$ is shown. Again, the eutectic point has broadened to an eutectic region. However, the region of Au-solid/liquid phase has now shrunk significantly in size.

5.6 Nanoscale Phase Diagram of Free-standing SnGe particles

Following the previously established model calculations, the SnGe system is investigated using a similar approach. The interface energies of SnGe-liquids and Ge-solid will be used as measured by Naidich and Perevertailo.(42) As before, due to the lack of information regarding the wetting characteristics of SnGe-liquids on Sn-solid, the trend of the measured values of SnGe-liquids on Ge-solid will be assumed. However, the values will be shifted such that the value of $\sigma^{Sn(sol)Sn(liq)}$ is $0.077 J/m^2$.(66)

Again, particle sizes of $r = 25 \times 10^{-9}$, 10×10^{-9} and 5×10^{-9} m are considered and the size dependent phase diagrams are calculated as described in the preceding sections. Results are shown in Figure 5.21. As described previously, the “bulk” and “standard nanoscale” phase diagrams are shown as well (black, dotted and black, solid lines, respectively). The dark blue region represents the Sn-solid/Ge-solid phase, while the red represents the homogeneous SnGe-liquid phase. The Ge-solid/liquid and Sn-solid/liquid phases are represented by yellow and light blue, respectively.

At a relatively large particle size ($r = 25 \times 10^{-9}$ m), the liquidus line of the “bulk” and “standard nanoscale” phase diagrams do not differ significantly. However, the eutectic temperature has decreased by approximately 25 K . Furthermore, the Ge-rich liquidus line calculated herein is in close agreement to those of the “bulk” and

“standard nanoscale” phase diagrams, with only a slight depression at compositions greater than $x_{Ge} = 0.5$. The major differences between the results calculated herein and the “standard nanoscale” phase diagram are similar to those described in the AuGe system above. Most notably, the eutectic line loses its’ invariance and shifts to lower temperatures, which is especially evident at high Ge concentrations, where the Ge-solid/liquid phase is predicted to be stable at temperatures far below the bulk eutectic temperature. Also, while barely visible, at very low Ge concentrations the Sn-solid/liquid phase is predicted to be stable at temperatures below the eutectic temperature predicted by the “standard nanoscale” phase diagram.

This behavior becomes more pronounced as the particle size is reduced to $r = 10 \times 10^{-9}$ m (see the center panel of Figure 5.21). At this particle size, the liquidus line also shows significant depression from those predicted by the “bulk” and “standard nanoscale” phase diagrams. Furthermore, the eutectic line has lost its’ invariance over the entire composition range. The region of Sn-solid/Ge-solid stability has been reduced in composition and temperature range significantly. Also, the region of Sn-solid/liquid phase stability is more pronounced. Once the particle size is decreased to $r = 5 \times 10^{-9}$, the region of Sn-solid/Ge-solid phase stability is barely present in the investigated temperature range ($200 \leq T \leq 1250$). The maximum concentration of a stable Sn-solid/liquid particle is found at approximately 7 at. % Ge and a temperature of $T \approx 290$ K. As before, the Ge-rich liquidus line is significantly depressed from those of the “bulk” and “standard nanoscale” phase diagrams.

5.7 Nanoscale Phase Diagram of AuGe particle embedded in SiO₂

Finally, we consider a AuGe particle of size $r = 5 \times 10^{-9}$ m embedded in SiO₂. In such a system, rather than using surface energies, the interface energies of the solids and liquids to SiO₂ must be used. As not all of the relevant interface energies are known, necessary assumptions must be made.

The interface energy $\gamma_{Ge(s)/SiO_2}$ and $\gamma_{Ge(l)/SiO_2}$ have been estimated to lie between 0.7 and 0.9 J/m².(58) Therefore, we set the interface energy of Ge liquid (assumed at its’ melting point) and SiO₂ equal to 0.7 J/m². It has been estimated that the surface energy of a solid is approximately proportional to 1.25 times the surface energy of the liquid. Accordingly, we will assume that a similar relationship exists for the interface energy: $\gamma_{Ge(s)/SiO_2} = 1.25\gamma_{Ge(l)/SiO_2}$.(3; 41; 32) Also, the temperature dependence of the respective liquid surface energy will be adopted. Hence,

$$\gamma_{Ge(l)/SiO_2} = 0.7 - 2.6 \times (T - 1211.5) \quad (5.19)$$

$$\gamma_{Ge(s)/SiO_2} = 0.875 - 3.25 \times (T - 1211.5). \quad (5.20)$$

Similarly for Au, we consider the available wetting data. Using the values of the

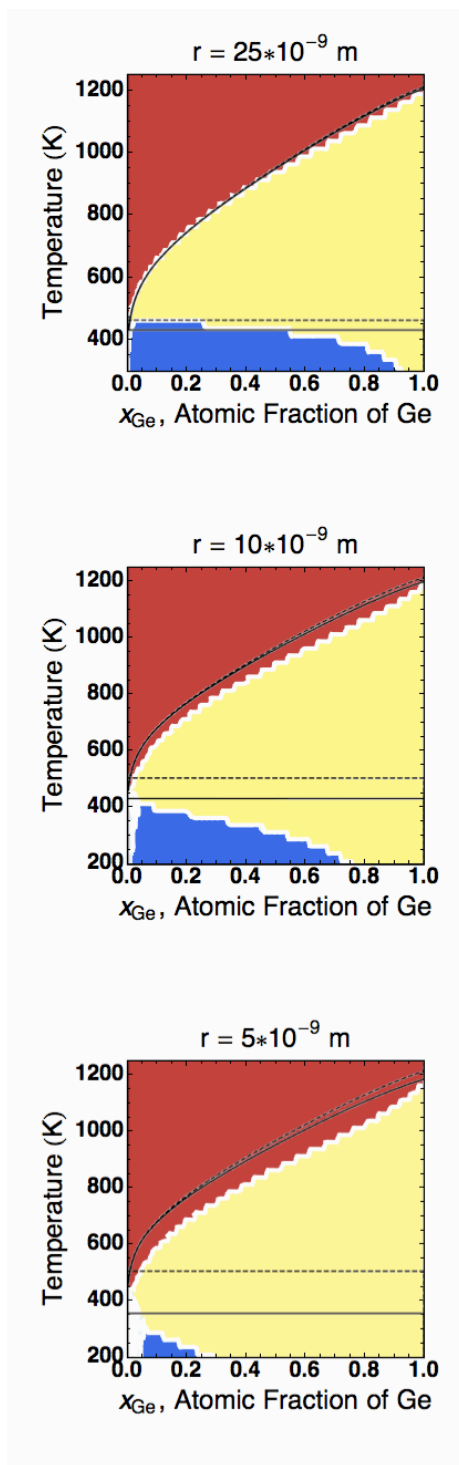


Figure 5.21. Three SnGe particle sizes are considered, $r = 25 \times 10^{-9}$, 10×10^{-9} and 5×10^{-9} m, and the size dependent phase diagrams are calculated. Resulting phase diagrams are shown in the top, center and bottom panels, respectively. The black, dotted lines represent the “bulk” phase diagram, while the black, solid lines represent the size dependent “standard nanoscale” phase diagrams. The dark blue, red and yellow regions represent the Sn-solid/Ge-solid phase, homogenous liquid, and Ge-solid/liquid phases, respectively.

interface energies of Au-liquid/SiO₂ measured by Kwon *et al.*(34), a linear fit to the temperature dependent interface energies can be calculated:

$$\gamma_{Au(l)/SiO_2} = 1.714 - 4 \times 10^{-4}T. \quad (5.21)$$

As before, the solid interface energy is assumed to be proportional to the liquid:

$$\gamma_{Au(s)/SiO_2} = 2.143 - 5 \times 10^{-4}T. \quad (5.22)$$

The interface energies of the composition dependent AuGe liquids are calculated using Butler’s equation as discussed in Chapter 4, but using the new endpoint values. Results of this calculation are shown in Figure 5.22. Under these assumptions, the composition dependent interface energies follow the same trends as those of the surface energies described in Chapter 4.

Using these values, the above described procedure may be employed to calculate the size dependent phase diagram of the AuGe nanoparticle embedded in SiO₂. Results of this calculation are shown in Figure 5.23. Again, the size dependent phase diagram calculated herein clearly deviates from the “bulk” phase diagram. The melting points of the elemental solids are lowered, and the liquidus and eutectic lines are clearly depressed from those predicted macroscopically. Additionally, the eutectic point has broadened to a eutectic region similar to that described above. However, it should also be noted that the phase diagram for the embedded nanoparticle differs from that of the free-standing nanoparticle described above. Clearly, when interface energies are used in place of the surface energies, the respective energies of the phases change, thus changing the regions in which the phases are stable. In general, the interface energies are larger in magnitude than the surface energies, leading to a even larger contribution of the surfaces to the total energy. Moreover, the assumed interface energies between the solids (Au(s) or Ge(s)) and the AuGe liquids remain unchanged. Thus, the values of γ_1 and γ_2 increase in magnitude in comparison to the free-standing nanoparticles, leading to a change in shape of the $G^{Solid-Liquid}$ curves, and further depression of the liquidus lines.

Finally, using the Ge-rich liquidus line evaluated for the embedded AuGe particle, γ_{Ge^{sol}/SiO_2} can once again be calculated as a function of temperature as discussed in Chapter 3. Results of this calculation (considering the possible size effects) are shown in Figure 5.24. Again, the black line represents the SnGe system, while the gray line represents the AuGe nanoscale system. Clearly, the shift in the liquidus line results in an overall decrease of the γ_{Ge^{sol}/SiO_2} -values. While the calculated curves no longer intersect, the AuGe results clearly have shifted to lower interface energies. Considering the values at $T = 600$ °C, the overlap of the error bars indicates an interface energy in the range of $\gamma_{Ge^{sol}/SiO_2} = 0.75 - 0.85$ J/m², which is in good agreement with prior predictions of $0.7 - 0.9$ J/m².

Au_{1-x}Ge_x system
T = 973, 1173, 1373,
1573, 1773, 1973

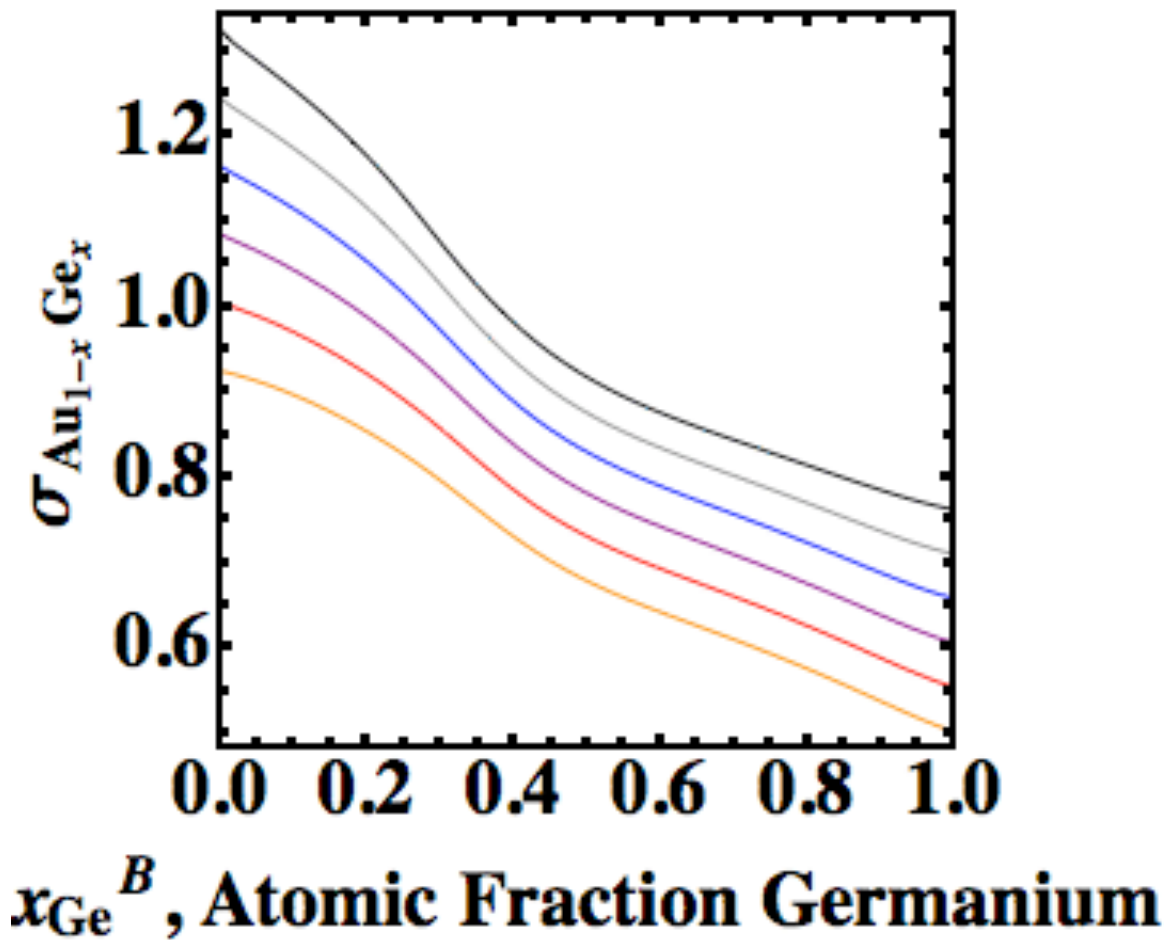


Figure 5.22. The composition dependent interface energies of Au_{1-x}Ge_x-liquids are calculated as a function of Ge concentration for various temperatures using Butler's equation.

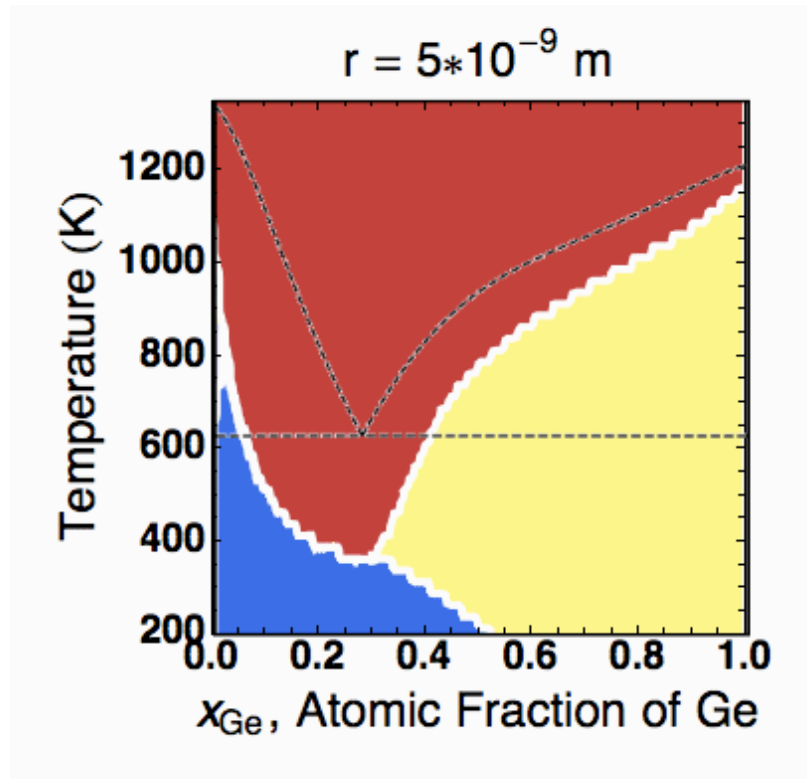


Figure 5.23. A AuGe particle of size $r = 5 \times 10^{-9} \text{ m}$ is considered to be embedded in a SiO_2 matrix and the size dependent phase diagram is considered. The blue region represents the solid-solid phase, while red represents the homogeneous liquid phase. Light blue and yellow represent the Au-solid/liquid and Ge-solid/liquid phases, respectively. The dotted line represents the “bulk” phase diagram as a point of comparison.

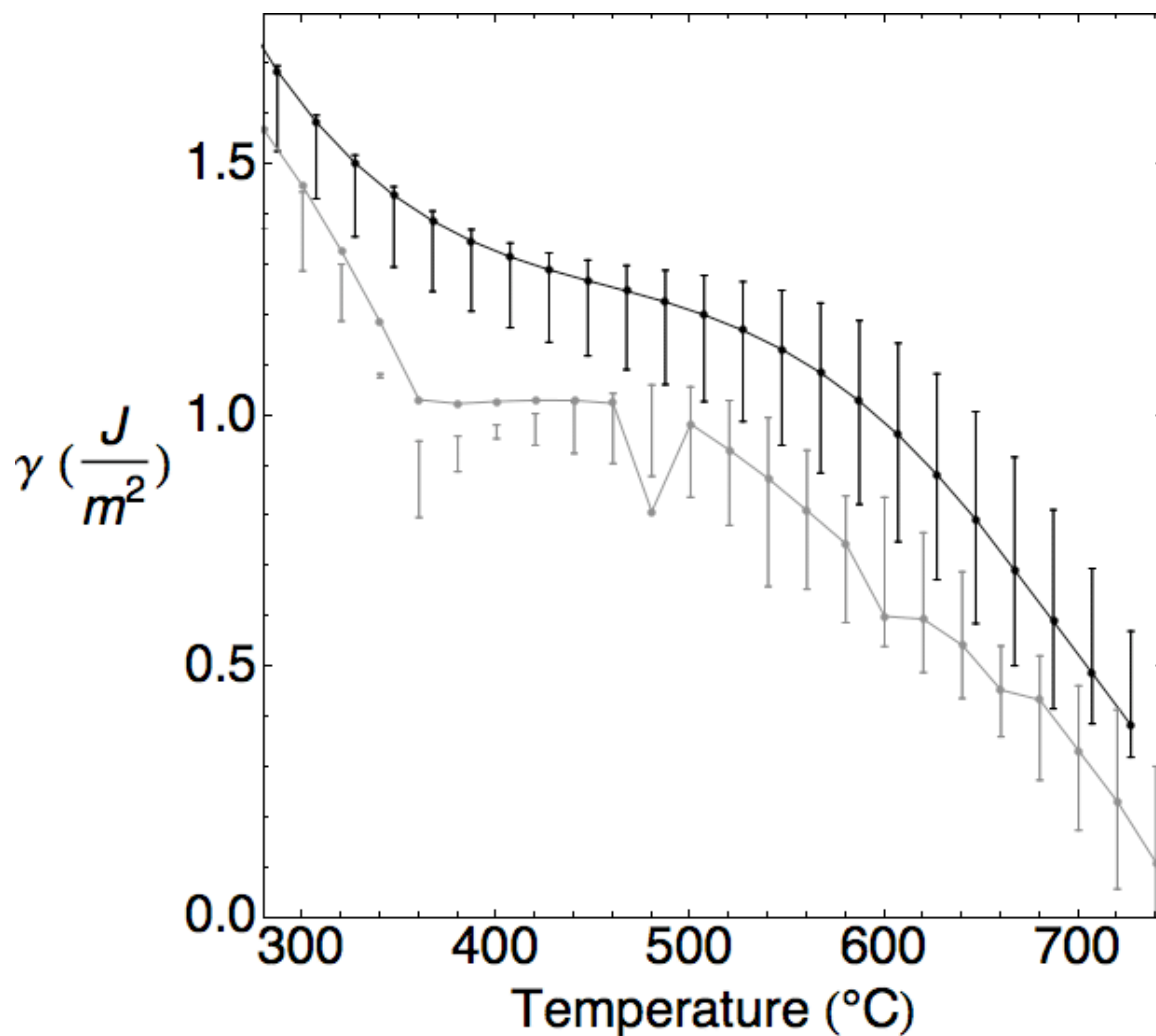


Figure 5.24. γ_{Ge^{sol}/SiO_2} is plotted as a function of temperature after taking into account the possibility of size effects in the AuGe system. The black line represents the results calculated from the SnGe system, while the gray line is calculated from the AuGe system at $r = 5 \times 10^{-9}$ m.

5.8 Discussion

Finally, we will consider the phase diagram depicted in Figure 5.23 more closely. Clearly, the phase diagram is strongly dependent on particle size and the regions of two-phase equilibrium have shifted significantly. Consider now the Ge-solid/liquid region represented by the yellow region of the phase diagram in Figure 5.23. In this region, we plot the compositions of the liquid phases that minimizes the total free energy of the Ge-solid/AuGe-liquid particle, shown in Figure 5.25. In the investigated temperature range, the embedded binary alloy nanoparticles are predicted to consist of Ge-solid and a AuGe-liquid. However, the composition of the AuGe liquid deviates from the behavior expected from standard bulk phase diagrams. We notice that at temperatures below approximately 450 K, the particles are expected to be composed of Ge-solid and a very Au-rich liquid phase. This is indicated by the dark blue region. These liquids are composed of less than 10 at. % Ge.

However, at temperatures above approximately 450 K, the composition of the liquids vary between approximately 30 and 100 at. % Ge. To investigate this, contours of equal liquid composition are plotted for liquids of compositions equal to 45, 65 and 85 at. % Ge. These contours are shown in Figure 5.25 as blue, green and red lines. Unlike the bulk phase diagram, these lines are not invariant to temperature, once again indicating that the lever rule is no longer applicable in nanoscale systems. Again, these results are consistent with the findings of Weissmueller *et al.* (68; 8; 69)

These results indicate that there is some kind of transition at a temperature of approximately 450 K. To further investigate this, we determine which morphology is stable at all temperatures and compositions of the two-phase region. This is shown in Figure 5.26, where blue represents the liquid-core/solid-shell structure, red the bilobe structure and yell the solid-core/liquid-shell structure. Clearly at temperatures below approximately 450 K, the most stable morphology is the Ge(sol)-core/AuGe(liq)-shell structure. As the temperature increases, the interface energies dictate that the bilobe structure minimizes the total free energy. At high temperatures around 1100 K, there also exists a small region in which the AuGe(liq)-core/Ge(sol) shell structure is stable. These regions are expected to shift as a function of particle size.

These results indicate that one may use particle size, composition and temperature to switch between various particle morphologies. For example, Figure 5.26 indicates that if a 5 nm AuGe particle embedded in a SiO₂ matrix is fabricated, temperature may be used to switch the particle between a bilobe and a core-shell nanocrystal nanocrystal. At this particle size, the transition temperature lies around approximately 450 K. Furthermore, increasing or decreasing the particle size will shift the transition temperature.

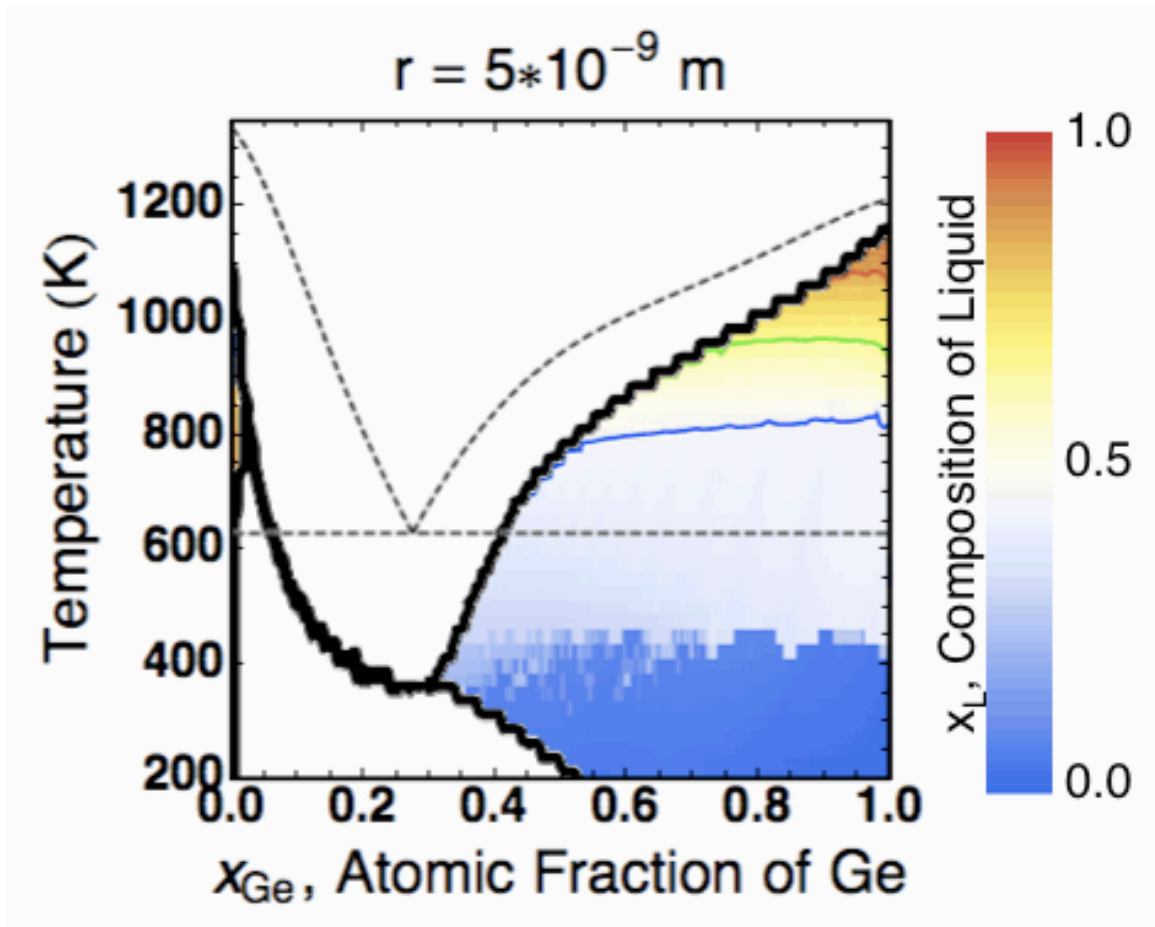


Figure 5.25. In the two-phase regions of the phase diagram, the composition of the respective liquid phases is plotted. The legend shows that liquids composed of 0 at. % Ge is represented by blue, while a liquid of 100 at. % Ge is represented by red.

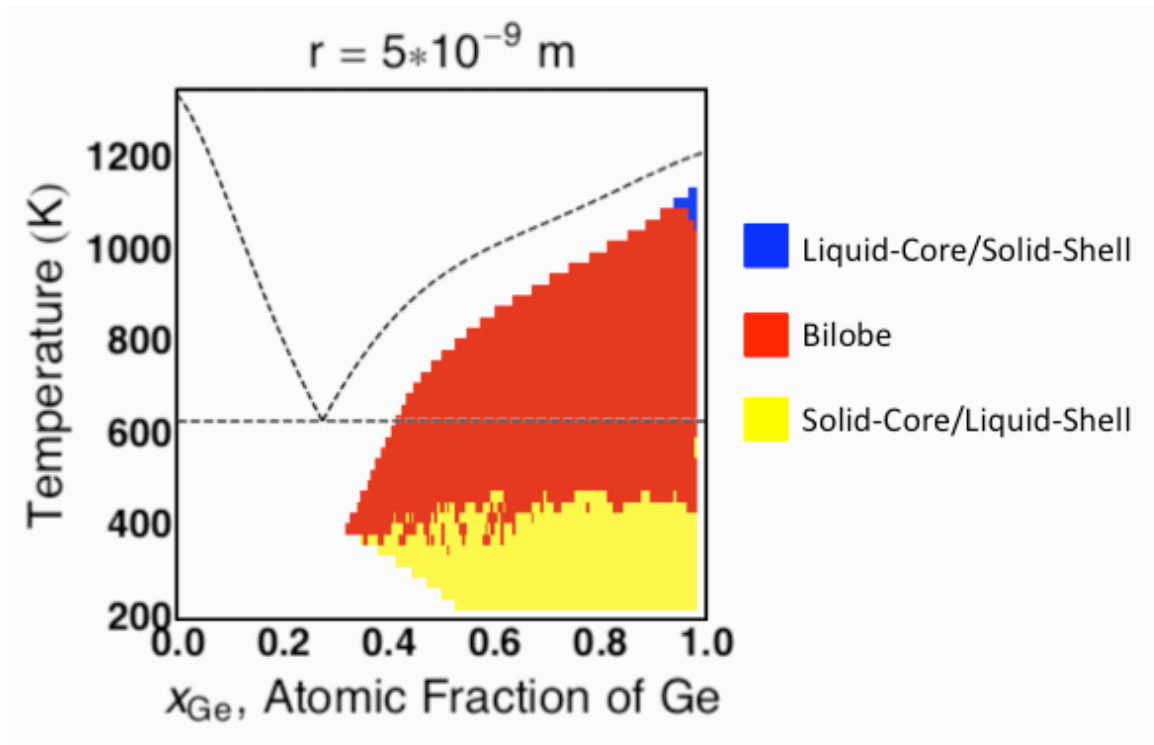


Figure 5.26. The Ge(sol)/AuGe(liq) region of the phase diagram is considered. Here, we determine which morphology is the structure that minimizes the total free energy of the particle. Blue and yellow represent the AuGe(liq)-core/Ge(sol)-shell and Ge(sol)-core/AuGe(liq)-shell structures, respectively. Red represents the bilobe structure. There is no region which is stabilized by the phase separated morphology.

Table 5.1. $\Delta G(\text{solid} \rightarrow \text{liquid})$ (J/m^3)

Au (FCC \rightarrow liquid)	$T \leq 1735.8 \text{ K}$	12552 -9.38587 T
Ge (diamond \rightarrow liquid)	$T \leq 900 \text{ K}$	$37141.5 + T(-30.687 + 8. \times 10^{-10}T + 8.5663 \times 10^{-21}T^6)$
	$900 \text{ K} < T \leq 1211.4 \text{ K}$	$37141.5 + T(-30.687 + 8. \times 10^{-10}T + 8.5663 \times 10^{-21}T^6)$
	$1211.4 \text{ K} < T \leq 3200 \text{ K}$	$36791.7 + 8.598 \times 10^{28}T^{-9} - 30.3838T$
Sn (BCT \rightarrow liquid)	$T \leq 250 \text{ K}$	$7103.09 + T(-14.0878 - 8. \times 10^{-8}T + 1.47031 \times 10^{-18}T^6)$
	$250 \text{ K} < T \leq 505.078 \text{ K}$	$7103.09 + T(-14.0878 - 8. \times 10^{-8}T + 1.47031 \times 10^{-18}T^6)$
	$505.078 \text{ K} < T \leq 800 \text{ K}$	$6971.59 + 1.2307 \times 10^{25}T^{-9} - 13.8144T - 8. \times 10^{-10}T^2$
	$800 \text{ K} < T \leq 3000 \text{ K}$	$6971.59 + 1.2307 \times 10^{25}T^{-9} - 13.8144T$

Chapter 6

Conclusions

The SnGe and AuGe systems were investigated at the nanoscale. Both systems displayed limited solid solubility and a eutectic type phase diagram. The first observation made by transmission electron microscopy was that both systems display a lobe-lobe or bilobe morphology when embedded and annealed in SiO₂.(60; 24) Evidenced by a previously calculated equilibrium structure map(72), interface energies in both systems fell in the region of bilobe stability, as this structure minimized the overall system energy. However, the region of bilobe stability contained an infinite number of possible γ -doublets, $\{\gamma_1, \gamma_2\}$, where $\gamma_1 = \gamma_{\alpha/M}/\gamma_{\alpha/\beta}$ and $\gamma_2 = \gamma_{\beta/M}/\gamma_{\alpha/\beta}$ (72) and further investigation was required to pinpoint the acting interface energies.

Therefore, two dimensionless length scales, η_1 and η_2 , were identified to further characterize the bilobes. These length scales described the bilobe particles independent of particle size; however, the volume fraction of the secondary phase, f_β , had to be known. Fortunately, the SnGe and AuGe phase diagrams and lever rule could be used to determine the volume fraction of liquid phase present as a function of temperature during cooling after the annealing step. Contour plots of η_1 and η_2 over the entire range of bi-lobe stability were then calculated for each value of f_β . Resulting contour plots were overlaid and the intersection of the contours indicated the values of γ_1 and γ_2 predicted at the respective temperature.

Available experimental wetting data of SnGe- and AuGe-liquids on Ge-solid could then be used to calculate $\gamma_{Ge(s)/SiO_2}$ as a function of temperature for each system. The intersection of the two predictions should indicate the temperature of bilobe setting. Although the predictions intersected twice in addition to a large region of error bar overlap, the bilobe setting temperature was estimated to lie at $T = 600$ °C. At this temperature, $\gamma_{Ge(s)/SiO_2}$ was found to be between 0.82-0.99 $\frac{J}{m^2}$. The respective values of $\gamma_{Ge_{0.22}Sn_{0.78}(l)/SiO_2}$ and $\gamma_{Au_{0.53}Ge_{0.47}(l)/SiO_2}$ were determined to be 1.20 and 0.94 $\frac{J}{m^2}$.

Although the effects of size with regard to melting temperature of elemental solids is generally well understood and accepted, the respective influence on binary alloy

phase diagrams is still largely unexplored. Previous investigations of phase diagrams were focused on the effects of surface energy contributions of the solid and liquid phases, causing a shift in the endpoints of the free energy curves. Application of the classical tangent rule resulted in the observation of an additional shift of the liquidus and eutectic lines. However, in the case of a nanoscale binary alloy, the free energy of, for example, a solid-liquid particle is not equal to the values predicted by the tangent rule, which is due to the existence of an internal interface, which also contributes to the total energy of the particle. Therefore, all possible phases must be considered at each composition and temperature, and the phase which truly minimizes the total energy of the system must be determined.

Butler's equation was initially used to calculate the composition dependent surface energies of the binary liquids in an attempt to determine the nanoscale phase diagrams. Subsequently, an approach first outlined by Weissmueller *et al.* was applied to determine the free energies of all phases as a function of size. Unsurprisingly, the nanoscale phase diagrams predicted herein differed significantly from those calculated using the classical approach. While the standard melting point depression of the elemental solids was observed, the liquidus lines showed further depression. Also, the eutectic line lost its invariance and became curved upward or downward depending on the values of the interface/surface energies. These results are in close agreement with predictions by Weissmueller *et al.* involving an imaginary binary alloy system.

Furthermore, the same procedure was applied to a AuGe particle of size $r = 5 \times 10^{-9}$ m consistent with the particles observed experimentally. However, now rather than using the surface energies, the interface energies to SiO_2 were used. This allowed us to recalculate the composition dependent interface energies using Butler's equation and subsequently calculate the phase diagram of an embedded AuGe nanoparticle. While the general characteristics of this phase diagram were similar to that of the free-standing particles, the location of the liquidus line differs, which allowed the recalculation of the temperature dependent values of $\gamma_{Ge(s)/SiO_2}$. When considering the effects of limited size, the determined values became: $0.75 - 0.85 \text{ J/m}^2$, which is in good agreement with previous estimates of $0.7 - 0.9 \text{ J/m}^2$.

Bibliography

- [1] A. P. Alivisatos, “Perspectives on the physical chemistry of semiconductor nanocrystals,” *J. Phys. Chem.*, vol. 100, p. 13226, 1996.
- [2] ———, “Semiconductor clusters, nanocrystals, and quantum dots,” *Science*, vol. 271, p. 933, 1996.
- [3] B. C. Allen and W. D. Kingery, “Surface tension and contact angles in some liquid metal-solid ceramic systems at elevated temperatures,” *Trans. Metall. Soc. AIME*, vol. 215, p. 30, 1959.
- [4] C. Antion and D. Chatain, “Liquid surface and liquid/liquid interface energies of binary subregular alloys and wetting transitions,” *Surface Science*, vol. 601, pp. 2232–2244, 2007.
- [5] D. R. Askeland, P. P. Fulay, and W. J. Wright, *The Science and Engineering of Materials*, 6th ed., H. Gowans, Ed. Global Engineering, Christopher M. Schorrt, 2010.
- [6] Y. L. Belousov, V. A. Firsov, and A. I. Shutov, “Temperature dependence of the modulus of elasticity of industrial glasses,” *Steklo i Keramika*, vol. 2, pp. 12–13, 1992.
- [7] P. Buffat and J.-P. Borel, “Size effect on the melting temperature of gold particles,” *Physical Review A*, vol. 13, no. 6, pp. 2287–2298, 1976.
- [8] P. Bunzel, “Phasengleichgewicht in nanoskaligen binären legierungspartikeln,” Ph.D. dissertation, Universitaet des Saarlandes, Forschungszentrum Karlsruhe, GmbH, 2004.
- [9] J. A. V. Butler, “The thermodynamics of the surfaces of solutions,” *Proc. R. Soc. Lond. A*, vol. 135, pp. 348–375, 1932.
- [10] T. Castro, R. Reifengerger, E. Choi, and R. P. Andres, “Size-dependent melting temperature of individual nanometer-sized metallic clusters,” *Physical Review B*, vol. 42, no. 13, 1990.

- [11] Y.-L. Chueh, C. N. Boswell, C.-W. Yuan, S. J. Shin, K. Takei, J. C. Ho, H. Ko, Z. Fan, E. E. Haller, D. C. Chrzan, and A. Javey, “Nanoscale structural engineering via phase segregation: Auge system,” *Nano Lett.*, vol. 10, no. 2, pp. 393–397, 2010.
- [12] P. R. Couchman and W. A. Jesser, “Thermodynamic theory of size dependence of melting temperature in metals,” *Nature*, vol. 269, pp. 481–483, 1977.
- [13] P. R. Couchman, “On the size-dependence of melting temperature,” Ph.D. dissertation, University of Virginia, 1976.
- [14] A. T. Dinsdale, “Sgte data for pure elements,” *CALPHAD*, vol. 15, no. 4, pp. 317–425, 1991.
- [15] Y. Eichhammer, J. Roeck, N. Moelans, F. Lacopi, B. Blanpain, and M. Heyns, “Calculation of the au-ge phase diagram for nanoparticles,” *Archives of Metallurgy and Materials*, vol. 53, no. 4, pp. 1133–1339, 2008.
- [16] Y. Eichhammer, M. Heyns, and N. Moelans, “Calculation of phase equilibria for an alloy nanoparticle in contact with a solid nanowire,” *CALPHAD: Computer Coupling of Phase Diagrams and Thermochemistry*, vol. 35, pp. 173–182, 2011.
- [17] Y. Feutelais, B. Legendre, and S. G. Fries, “Thermodynamic evaluation of the system germanium-tin,” *Calphad*, vol. 20, no. 1, pp. 109–123, 1996.
- [18] T. Gancarz, Z. Moser, W. Gasoir, J. Pstrus, and H. Henein, “A comparison of surface tension, viscosity, and density of sn and sn-ag alloys using different measurement techniques,” *Int J Thermophys*, vol. 32, pp. 1210–1233, 2011.
- [19] W. Gasior, “Modeling of the thermodynamic properties from the surface tension,” *Archives of Metallurgy and Materials*, vol. 51, no. 3, pp. 317–326, 2006.
- [20] W. Gasior, P. Fima, and Z. Moser, “Modeling of the thermodynamic properties of liquid fe-ni and fe-co alloys from the surface tension data,” *Archives of Metallurgy and Materials*, vol. 56, no. 1, pp. 13–23, 2011.
- [21] W. Gasior, Z. Moser, and J. Pstrus, “Surface tension, density and molar volume of liquid of sb-sn alloys: Experiment versus modeling,” *Journal of Phase Equilibria*, vol. 24, no. 6, pp. 504–510, 2003.
- [22] D. R. Gaskell, *Introduction to the Thermodynamics of Materials*, 4th ed. Taylor and Francis, 2003.
- [23] A. N. Goldstein, C. M. Echer, and A. P. Alivisatos, “Melting in semiconductor nanocrystals,” *Science*, vol. 256, p. 1425, 1992.
- [24] J. Guzman, C. N. Boswell-Koller, J. W. Beeman, K. C. Bustillo, T. Conry, O. D. Dubón, W. L. Hansen, A. X. Levander, C. Y. Liao, R. R. Lieten, C. A. Sawyer, M. P. Sherburne, S. J. Shin, P. R. Stone, M. Watanabe, K. M. Yu,

- J. W. A. III, D. C. Chrzan, and E. E. Haller, "Reversible phase changes in ge-au nanoparticles," *Applied Physics Letters*, vol. 98, no. 1, pp. 1–3, 2011.
- [25] V. C. Holmberg, M. G. Panthani, and B. A. Korgel, "Phase transitions, melting dynamics, and solid-state diffusion in a nano test tube," *Science*, vol. 326, pp. 405–407, 2009.
- [26] D. Houlier and P. Perrot, "Au-si and au-ge phase diagrams for nanosystems," *Materials Science Forum*, vol. 653, pp. 77–85, 2010.
- [27] T. Iida and R. Guthrie, *The Physical Properties of Liquid Metals*. Clarendon Press, Oxford, 1988.
- [28] W. A. Jesser, G. J. Shiflet, G. L. Allen, and J. L. Crawford, "Equilibrium phase diagrams of isolated nano-phases," *Mat. Res. Innovat*, vol. 2, pp. 211–216, 1999.
- [29] Z. Jian, K. Kuribayashi, and W. Jie, "Solid–liquid interface energy of metals at melting point and undercooled state," *Materials Transactions*, vol. 43, no. 4, pp. 721–726, 2002.
- [30] Q. Jiang, S. Zhang, and M. Zhao, "Size-dependent melting point of noble metals," *Materials Chemistry and Physics*, vol. 82, pp. 225–227, 2003.
- [31] N. Kaiser, A. Croell, F. R. Szofran, S. D. Cobb, , and K. Benz, "Wetting angle and surface tension of germanium melts on different substrate materials," *J. Cryst. Growth*, vol. 231, p. 448, 2001.
- [32] V. K. Kumikov, "The measurement of the surface tension of some pure metals in the solid state," *Materials Science and Engineering*, vol. 60, 1983.
- [33] V. K. Kumikov and K. B. Khokonov, "On the measurement of surface free energy and surface tension of solid metals," *Journal of Applied Physics*, vol. 54, pp. 1346–1350, 1983.
- [34] J.-Y. Kwon, T.-S. Yoon, and K.-B. Kim, "Comparison of the agglomeration behavior of au and cu films sputter deposited on silicon dioxide," *Journal of Applied Physics*, vol. 93, no. 6, pp. 3270–3278, 2003.
- [35] J. Lee, W. Shimoda, and T. Tanaka, "Temperature dependence of surface tension of liquid sn-ag, in-ag and in-cu alloys," *Measurement Science and Technology*, vol. 16, pp. 438–442, 2005.
- [36] J. Lee, J. Lee, T. Tanaka, H. Mori, and K. Penttilae, "Phase diagrams of nanometer-sized particles in binary systems," *JOM Research Summary Nanomaterials*, 2005.
- [37] J. Li, Z. Yuan, Z. Qiao, J. Fan, Y. Xu, and J. Ke, "Measurement and calculation of surface tension of molten sn-bi alloy," *Journal of Colloid and Interface Science*, vol. 297, pp. 261–265, 2006.

- [38] Y. Lijun, X. Yunan, X. Xianran, and Q. Zhiyu, "Prediction of surface tensions of pure liquid metals and alloys," *Journal of Rare Earths*, vol. 17, no. 3, pp. 182–188, 1999.
- [39] D. A. McGraw, "A method for determining young's modulus of glass at elevated temperatures," *J. Am. Chem. Soc.*, vol. 35, no. 1, pp. 22–27, 1952.
- [40] A. Meldrum, R. F. Haglund, L. A. Boatner, and C. W. White, "Nanocomposite materials formed by ion implantation," *Adv. Mat.*, vol. 13, no. 19, p. 1431, 2001.
- [41] L. E. Murr, *Interfacial Phenomena in Metals and Alloys*. Addison-Wesley Pub. Co., Advanced Book Program, 1975.
- [42] Y. V. Naidich and V. M. Perevertailo, "Surface and contact properties in the system composed of germanium and a tin-germanium melt," *Poroshkovaya Metallurgiya*, vol. 2, no. 98, pp. 74–80, 1971.
- [43] —, "Contact properties of the phases participating in the crystallization of gold-silicon and gold-germanium melts," *Poroshkovaya Metallurgiya*, vol. 7, no. 151, pp. 63–69, 1975.
- [44] P. Normand, E. Kapetanakis, P. Dimitrakis, D. Skarlatos, K. Beltsios, D. Tsoukalas, C. Bonafos, G. B. Assayag, N. Cherkashin, A. Claverie, J. A. V. D. Berg, V. Soncini, A. Agarwal, M. Ameen, M. Perego, and M. Fanciulli, "Nanocrystals manufacturing by ultra-low-energy ion-beam-synthesis for non-volatile memory applications," *Nucl. Instrum. Meth. B*, vol. 216, p. 228, 2004.
- [45] D. F. Ollis, "Phase equilibrium in binary alloy crystallites," *Journal of Catalysis*, vol. 23, pp. 131–140, 1971.
- [46] E. A. Olsen, M. Y. Elfremov, M. Zhang, Z. Zhang, and L. H. Allen, "Size-dependent melting of bi nanoparticles," *Journal of Applied Physics*, vol. 97, p. 03404, 2005.
- [47] S. J. Palmer, "The effect of temperature on surface tension," *Physics Education*, vol. 11, pp. 119–121, 1976.
- [48] J. Park and J. Lee, "Phase diagram reassessment of ag-au system including size effect," *CALPHAD: Computer Coupling of Phase Diagrams and Thermochemistry*, vol. 32, pp. 135–141, 2008.
- [49] P. Z. Pawlow, "Über die abhängigkeit des schmelzpunktes von der oberflächenenergie eines festen körpers," *Z. Physik. Chem.*, vol. 65, pp. 545–548, 1909.
- [50] R. Picha, J. Vrestal, and A. Kroupa, "Prediction of alloy surface tension using a thermodynamic database," *Computer Coupling of Phase Diagrams and Thermochemistry*, vol. 28, pp. 141–146, 2004.

- [51] W. H. Qi and M. P. Wang, “Size and shape dependent melting of metallic nanoparticles,” *Materials Chemistry and Physics*, vol. 88, pp. 280–284, 2004.
- [52] —, “Size and shape dependent melting temperature of metallic nanoparticles,” *Materials Chemistry and Physics*, vol. 88, pp. 280–284, 2004.
- [53] O. Redlich and A. T. Kister, “Algebraic representation of thermodynamic properties and the classification of solutions,” *Industrial and Engineering Chemistry*, vol. 40, no. 2, pp. 346–348, 1948.
- [54] E. Roduner, “Size matters: why nanomaterials are different,” *Chem. Soc. Rev.*, vol. 35, pp. 583–592, 2006.
- [55] H. Sadan and W. D. Kaplan, “Au–sapphire (0001) solid–solid interfacial energy,” *Journal of Materials Science*, vol. 41, no. 16, 2006.
- [56] C. T. Schamp and W. A. Jesser, “Two-phase equilibrium in individual nanoparticles of bi-sn,” *Metallurgical and Materials Transactions A*, vol. 37A, pp. 1825–1829, 2006.
- [57] I. D. Sharp, Q. Xu, C. Y. Liao, D. O. Yi, J. W. Beeman, Z. Liliental-Weber, K. M. Yu, D. N. Zakharov, J. W. A. III, D. C. Chrzan, and E. E. Haller, “Stable, freestanding ge nanocrystals,” *J. Appl. Phys.*, vol. 97, p. 124316, 2005.
- [58] I. D. Sharp, D. O. Yi, Q. Xu, C. Y. Liao, J. W. Beeman, Z. Liliental-Weber, K. M. Yu, D. N. Zakharov, J. W. A. III, D. C. Chrzan, and E. E. Haller, “Mechanism of stress relaxation in ge nanocrystals embedded in SiO_2 ,” *Applied Physics Letters*, vol. 86, no. 063107, 2005.
- [59] P. Shen, H. Fujii, and K. Nogi, “Wetting, adhesion and adsorption in al-si/(01112) -alumina system at 1723k,” *Materials Transactions*, vol. 45, no. 9, pp. 2857–2863, 2004.
- [60] S. J. Shin, J. Guzman, C. W. Yuan, C. Y. Liao, C. N. Boswell-Koller, P. R. Stone, O. D. Dubon, A. M. Minor, M. Watanabe, J. W. Beeman, K. M. Yu, J. W. Ager, D. C. Chrzan, and E. E. Haller, “Embedded binary eutectic alloy nanostructures- a new class of phase change materials,” *Nano Lett.*, 2010.
- [61] R. Shuttleworth, “The surface tension of solids,” *Proc. Phys. Soc. A*, vol. 63, pp. 444–457, 1950.
- [62] T. Soma, H. Matsuo, and S. Kagaya, “Phase diagrams of the si-sn and ge-sn systems,” *Phys. Stat. Sol. B*, vol. 105, pp. 311–314, 1981.
- [63] E. Sutter and P. Sutter, “Phase diagram of nanoscale alloy particles used for vapor-liquid-solid growth of semiconductor nanowires,” *Nano Lett.*, vol. 8, no. 2, pp. 411–414, 2008.

- [64] T. Tanaka, "Prediction of phase diagrams in nano-sized binary alloys," *Materials Science Forum*, vol. 653, pp. 55–75, 2010.
- [65] T. Tanaka, K. Hack, and S. Hara, "Calculation of surface tension of liquid bi-sn alloy using thermochemical application library chemapp," *Calphad*, vol. 24, no. 4, pp. 465–474, 2000.
- [66] B. Vinet, L. Magnusson, H. Fredriksson, and P. J. Desre, "Correlations between surface and interface energies with respect to crystal nucleation," *Journal of Colloid and Interface Science*, vol. 255, pp. 363–374, 2002.
- [67] M. Wautelet, J. P. Dauchot, and M. Hecq, "Phase diagrams of small particles of binary systems: a theoretical approach," *Nanotechnology*, vol. 11, pp. 6–9, 2000.
- [68] J. Weissmueller, P. Bunzel, and G. Wilde, "Two-phase equilibrium in small alloy particles," *Scripta Materialia*, vol. 51, pp. 813–818, 2004.
- [69] G. Wilde, P. Bunzel, H. Roesner, and J. Weissmueller, "Phase equilibria and phase diagrams of nanoscaled systems," *Journal of Alloys and Compounds*, vol. 434–435, pp. 286–289, 2007.
- [70] Q. Xu, I. D. Sharp, C. W. Yuan, D. O. Yi, C. Y. Liao, A. M. Glaeser, A. M. Minor, J. W. Beeman, M. C. Ridgway, P. Kluth, J. W. A. III, D. C. Chrzan, and E. E. Haller, "Large melting-point hysteresis of ge nanocrystals embedded in SiO_2 ," *Phys. Rev. Lett.*, vol. 97, no. 15, p. 155701, 2006.
- [71] S. W. Yoon, W. K. Choi, and H. M. Lee, "Calculation of surface tension and wetting properties of sn-based solder alloys," *Scripta Materialia*, vol. 40, no. 3, pp. 297–302, 1999.
- [72] C. W. Yuan, S. J. Shin, C. Y. Liao, J. Guzman, P. R. Stone, M. Watanabe, J. W. Ager, E. E. Haller, and D. C. Chrzan, "Structure map for embedded binary alloy nanocrystals," *Appl. Phys. Lett.*, vol. 93, no. 19, 2008.
- [73] M. Yudin and B. D. Hughes, "Surface energy of solids," *Physical Review B*, vol. 49, no. 8, pp. 5638–5642, 1994.